



Properties and deformation characteristics of mechanically worked sintered billets.

ALKATIB, Hassan S.

Available from the Sheffield Hallam University Research Archive (SHURA) at:

<http://shura.shu.ac.uk/19246/>

A Sheffield Hallam University thesis

This thesis is protected by copyright which belongs to the author.

The content must not be changed in any way or sold commercially in any format or medium without the formal permission of the author.

When referring to this work, full bibliographic details including the author, title, awarding institution and date of the thesis must be given.

Please visit <http://shura.shu.ac.uk/19246/> and <http://shura.shu.ac.uk/information.html> for further details about copyright and re-use permissions.

POND STREET
SHEFFIELD S1 1WB

844336/83

7912113010



Sheffield City Polytechnic Library

REFERENCE ONLY

ProQuest Number: 10694126

All rights reserved

INFORMATION TO ALL USERS

The quality of this reproduction is dependent upon the quality of the copy submitted.

In the unlikely event that the author did not send a complete manuscript and there are missing pages, these will be noted. Also, if material had to be removed, a note will indicate the deletion.



ProQuest 10694126

Published by ProQuest LLC (2017). Copyright of the Dissertation is held by the Author.

All rights reserved.

This work is protected against unauthorized copying under Title 17, United States Code
Microform Edition © ProQuest LLC.

ProQuest LLC.
789 East Eisenhower Parkway
P.O. Box 1346
Ann Arbor, MI 48106 – 1346

PROPERTIES AND DEFORMATION CHARACTERISTICS
OF MECHANICALLY WORKED SINTERED BILLETS

by

Hassan S Alkatib
BSc., M.Phil.

This thesis is submitted for the Degree of
DOCTOR OF PHILOSOPHY
under the auspices of
SHEFFIELD CITY POLYTECHNIC
with registration with the
COUNCIL FOR NATIONAL ACADEMIC AWARDS

Department of Mechanical and Production Engineering
Sheffield City Polytechnic
Pond Street
Sheffield S1 1WB
England

June 1982

Collaborating Establishment

National Engineering Laboratories
East Kilbride
Glasgow



7912113 01

ACKNOWLEDGEMENTS

The author wishes to express his sincere appreciation to Dr M S J Hashmi, Director of Studies of this project, for his guidance and encouragement, and to Mr G Butterworth for his thorough assessment of the manuscript and for his most constructive comments.

The author would also like to express his gratitude to Mr O Bardsley, Head of the Department of Mechanical and Production Engineering, for his kind support and to the authorities of Sheffield City Polytechnic for their approval to carry out this work.

Thanks are also extended to everyone who supported and contributed to this work at every stage and level.

Finally, a word of thanks to my wife for her patience and preference of my work to her pleasure.

ABSTRACT

Properties and Deformation Characteristics of Mechanically Worked Sintered Billets

H S Alkatib

Sheffield City Polytechnic

This project originated from the desire to provide the sintered preform designers in forging industries with useful information on the effects of certain process variables on the forged product and to formulate these effects into comprehensive relationships of the basic rheological characteristics of the material. A further aim was to establish a technique to theoretically demonstrate the applicability of these relationships, by analysing simple forging of sintered billets.

A literature survey covering three main areas in general is presented highlighting the effects of various process variables on the mechanical properties, the deformation characteristics of various sintered materials, and the attempts to establish a yield criterion for porous materials on the basis of experimental results and theoretical analysis.

The experimental programme involved the design, construction and machining, where appropriate, of a double cone powder mixer, a sintering unit, and three die compaction sets, compacts of atomised iron powder, mixed with 0.25% flake graphite were made of various heights, diameters and

densities and sintered at various sintering conditions. Further work included preparation of testpieces for compression, tension, impact, hardness, chemical analysis and metallographic tests and making of forging dies for upsetting, upset-extrusion, capped ends upsetting, triangular cavity and multi-cavity closed die forging.

The programme of work involved the study of,

1. The effects of sintering time and temperature on the mechanical properties of sintered iron, on the deformation characteristics and on the properties of the upset specimens.
2. The effects of aspect ratio on the deformation characteristics of sintered billets.
3. The behaviour of the material through testing specimens of various cross-sections (circular, square rectangular, triangular and semi-circular) and by changing die geometry in order to simulate effects in actual closed die forging.
4. Closed die forging simulating the production of two and four gear teeth of various widths.
5. The existing yield criteria in an attempt to improve their applicability in respect of sintered iron.
6. A finite-difference numerical technique in order to simulate the upsetting process of a variable density material. Comparison of the predicted results with those observed experimentally showed good agreement.

CONTENTS

	<u>Page No.</u>
ACKNOWLEDGEMENTS	I
ABSTRACT	II
CONTENTS	IV
LIST OF SYMBOLS	VII
CHAPTER 1 - INTRODUCTION	
1.1 Background	1
1.2 Literature survey	4
1.2.1 Mechanical properties of sinter forged materials	5
1.2.2 Deformation characteristics of sinter forged materials	12
1.2.3 Plasticity theory for porous materials	20
1.3 Objectives and means	24
CHAPTER 2 - EXPERIMENTAL EQUIPMENT AND TEST-PIECE PREPARATION	
2.1 Materials	26
2.1.1 Powders	26
2.1.2 Lubricants	27
2.2 Tools	27
2.2.1 Powder mixing	27
2.2.2 Compaction	28
2.2.3 Sintering	29
2.2.4 Compressing machines and tools	30
2.3 Measurements	32
2.4 Test-piece preparation	
2.4.1 Compaction	34
2.4.2 Sintering	36
2.4.3 Machining	36
2.4.4 Metallographic examination	36
Tables	38
Figures	39

CHAPTER 3 - SINTERING CONDITIONS AND ASPECT RATIO

3.1	Introduction	47
3.2	Test Procedure and Results	49
3.2.1	Sintering conditions	49
3.2.2	Aspect ratio	51
3.3	Discussion	52
3.3.1	Effect of sintering conditions	52
3.3.2	Effect of aspect ratio	57
	Table of Results	62
	Figures	68

CHAPTER 4 - FLOW AND FRACTURE OF MATERIAL OF VARYING GEOMETRY

4.1	Introduction	91
4.2	Present work	92
4.2.1	Upsetting of various cross sections	93
4.2.2	Upset extrusion	94
4.2.3	Upsetting with capped ends	96
4.2.4	Triangular-cavity closed die forging	97
4.2.5	Closed die forging of cylindrical preforms into cavities of various widths	99
	Table of Results	102
	Figures	109

CHAPTER 5 - PLASTICITY THEORY AND A NUMERICAL TECHNIQUE FOR ANALYSING UPSETTING OF CYLINDRICAL BILLETS OF POROUS MATERIAL

5.1	Plasticity Theory for Sintered Materials	126
5.1.1	Verification of Oyan's Criterion	131
5.1.2	Determination of f and \bar{f}	
5.2	Stress-Strain-Density Diagram	137
5.3	Yield Stress Space Diagram	138

5.4	Analysis of Simple Upsetting of Cylindrical Billets of Porous Material using a Finite Difference Numerical Technique.	140
5.4.1	Analysis	142
5.4.2	Experimental work	147
5.4.3	Discussions	148
Figures		153
CHAPTER 6 - CONCLUSIONS and RECOMMENDATIONS		
6.1	Conclusions	177
6.2	Recommendations	180
REFERENCES		182

LIST OF SYMBOLS

a	Constant
A	Cross-sectional area
AR, AR_f, AR_0	Current, final and initial aspect ratios respectively
b	constant
$d\epsilon_1, d\epsilon_2, d\epsilon_3,$ $d\epsilon_i$	Plastic strain increment in the directions 1, 2, 3 and i respectively
$d\bar{\epsilon}_{eq}$	Equivalent strain increment
$d\lambda$	Proportionality constant
dW	Plastic work increment
D	Material strain-rate constant
D_f	Final diameter
E	Tooth depth/width ratio
f	The hydrostatic stress porosity parameter
\bar{f}	Applied stress/effective stress parameter
F	Function
g	Plastic potential
H_f, H_0	Final and initial heights respectively
i	Any direction, the mass number of the proceeding link
j	Instant of time
J_2	Second invariant of stress
\bar{J}_2	Second invariant of deviatoric stress
m	Mass per unit length, Mean value
n	Constant
P	Flow stress, Material strain rate constant
P_s	Flow stress of sintered material

Δs	Link length in the lumped parameter model
δt	Time increment
T	Constant
u	Displacement
v	Displacement, Constant
W	Width of forged tooth
x, y	Co-ordinate axes
$\epsilon_a, \epsilon_l, \epsilon_v$	Axial, lateral and volumetric strains, respectively
ρ, ρ_f, ρ_o	Density, current, final and initial, respectively
$\sigma_1, \sigma_2, \sigma_3,$ σ_i	Principal stress in the directions 1, 2, 3 and i respectively
$\bar{\sigma}_{eq}$	Effective stress
σ_m	Hydrostatic stress
σ_o	Yield stress of matrix material
μ	Coefficient of friction
ν	Poisson's ratio $= d\epsilon_l/d\epsilon_a$

Superscripts

$(\dot{})$	Single differentiation with respect to time
$(\ddot{})$	Double differentiation with respect to time

CHAPTER 1

INTRODUCTION

1.1 Background

Sintered components are basically made from powder material which has been subjected to a high temperature either in the loose or compacted form. In the loose form the component takes the shape of its container and will be highly porous like in the case of filters. The porosity of the sintered component in general is determined by many factors such as; particle shape and inclusions, packing, pressing technique, pressure level and degree of heating.

Metallic powders may be manufactured by a large number of mechanical and chemical techniques which produce particles of different configurations and purities. These aspects in turn have various effects on the densification mechanism during compaction and on the nature of bonds formed during sintering.

The powder can be compacted by various methods depending on the shape of the compact and its use. Compaction can be carried out in the die with single or multiple punches or in an envelope placed in a pressurised chamber. It can be compacted by extruding a canned powder or by a rolling

technique. Again, depending on the compaction technique employed and on the pressure and temperature levels applied, the properties of the compact will vary. Furthermore, for a particular sintering process, the sintering atmosphere, duration and temperature have considerable effects on the properties of the component.

The availability of a great number of powder materials and process variables widen the choice and options for the producer of sintered components. Furthermore, there are many technical and economic advantages in using sintered components, such as, simplicity of alloying and obtaining alloys which otherwise are unobtainable, no material waste, good tolerances and finish, no machining, low capital investment, light where weight is critical and useful where porosity is intended (bearings and filters) and the near finished preform shape offers great savings when metal forging is required.

Because of the presence of porosity, the strength of sintered components are lower than their counterparts in solid material. Therefore, a forging process becomes essential when full density is required. In this case, the material is allowed to deform in order to densify and, at the same time, fill the forging die cavity and consequently

it work hardens as well. Also, full density can be achieved by direct hot repressing which does not involve plastic deformation.

For the forging process, a knowledge of proper preform and die design is vital. The successful forging process is the one which allows the preform to fill the die cavity without cracking and the attainment of full density without excessive repressing.

Extensive research has been carried out on the plastic behaviour of solid materials and many theories have been developed. Because of the fundamental assumption of volume constancy, these solutions cannot be applied to porous materials. Hence, the need for a new solution. When the volume is constant, the hydrostatic stress component is usually ignored in the analysis, but for porous materials it should be considered. Furthermore, the presence of pores increases the likelihood of fracture, also, the nature of bonds to be established by closing-up the pores during deformation might have a significant effect on the properties of the product.

There have been many attempts to establish theoretical solutions for the plastic deformation of porous materials

or to modify the conventional theory of plasticity for solid materials to accommodate the change of volume.

However, the author believes that there is considerable need and scope for further research in this field. The aim of the experimental programme and the analyses developed in this study is to further the understanding of the plastic behaviour of sintered billets during the forging process in general and simple upsetting in particular.

1.2 Literature Survey

The subject of powder metallurgy has been given extensive consideration in recent years and much effort has been directed to the study of a wide range of processes and manufacturing techniques, namely; powder production, powder compaction, sintering of the compacts, forging and heat treatment of the sintered compacts. The aim of this literature survey is to gather up-to-date information on the characteristics of sinter-forged materials. Most of the work which has been done so far has been concentrated on the mechanical properties of sintered components and their dependance on the level of porosity in the material. There have been some attempts to analyse the plastic deformation of sintered materials and to relate it to the existing plasticity theories with due consideration to the

densification which takes place during the forging process. Furthermore, a few theoretical attempts have been aimed to analyse theoretically the behaviour of porous materials during plastic deformation.

The bulk of this survey is concentrated mainly on three areas:-

1. Mechanical properties of sinter-forged materials.
2. Deformation characteristics of sintered materials.
3. Plasticity theories for porous materials.

1.2.1 Mechanical Properties of Sinter-Forged Materials

In the manufacturing of any metallic component, the mechanical properties are the major factor determining the material used and the shape and size of the component. For porous materials, the mechanical properties are highly dependent on the porosity level. The manufacturing technique for sintered components permits the incorporation of many subroutine processes that help in reducing the porosity level and improving the mechanical properties. The selection of these processes is dependent on the particular use of each component. Hence, most of the research carried out in this field has been concentrated on one or more of these processes.

This survey is confined to ferrous materials only.

While establishing the effects of some characteristics of the raw material, ie the powder particles, Bargainnier and Hirschhorn (1) observed no significant effect of the powder particle size on hot forging of steel except poor reproducibility of final density resulting from fine powder.

Later on, Hupmann (2) observed an increase in Charpy energy of the finer particle size of water atomized iron powder after being hot forged in a closed die in order to achieve a high degree of lateral flow. Hupmann (2) and Antes (3) found that atomized iron preforms densify to a higher rate than sponge iron preforms. Also when Antes added carbon to the iron powder in the range of 0.41-0.61% he noticed no effect on the rate of densification, but the load requirement to achieve a given density was increased. Antes and Stock (4) observed the same effect of carbon additions on yield strength in hot forging of steels; the impact strength was also increased at room temperature, but decreased once a fully martensitic structure was achieved. Zapf (5) tested the effect of the addition of 1-10% nickel in hot recompaction of iron compacts and found that nickel increases the ultimate tensile strength and hardness, but decreases elongation and electrical conductivity. Cundill,

Marsh and Ridal (6) investigated forged iron powders with a variety of additions of alloying elements and obtained properties comparable to low alloy steel forgings. They observed that blended iron alloys gave much higher tensile strength, ductility and impact resistance than those obtained from pre-alloyed iron. Obara et al (7) studied the cold forgeability of reduced electrolytic and atomized iron powders. The reduced powder exhibited the best results.

Amongst the factors which enhance densification is lubrication. Bargainnier and Hirschhorn (1) reported that lubrication increases the density from 92 to 96% and reduces ejection load by 30% in the closed die hot forging of steel powder. Araki, et al, (8) investigated friction at the tool-workpiece interface using the wedge indentation method and they concluded that the coefficient of friction for a porous material is lower than for a pore-free material.

Forging at high temperatures greatly promotes densification and forgeability of sintered materials. Huseby and Scheil (9) hot forged steel powder compacts and they observed that two ranges of favourable temperatures ($730-915^{\circ}\text{C}$) and ($1037-1148^{\circ}\text{C}$) exist. They also observed that material flow is good at the lower range. Marx, Davies and Guest (10), in their hot upset forging of sponge iron billets to 61%

reduction of height, showed that at 925°C excellent properties could be obtained. However, they recommended the temperature of 1100°C as the best choice for industrial application because the lower temperature is very critical and hence difficult to control. Later, Suzuki and Shimamura (11) hot forged three kinds of pure iron at temperatures from 900 to 1200°C and obtained better tensile strength at 1000°C and better impact resistance at higher temperatures and also recommended the temperature 1100°C as the optimum by using a high energy-rate forging machine. Furthermore, they related the increase of tensile and hardness strengths to the grain size, which is finest at 1000°C , and the impact and elongation properties to the forged density. Similar results were obtained by Shah and Ramakrishnan (12) who also recommended heat treatment after forging in order to improve the properties. In fact, the lower range of forging temperature has another advantage when economics are concerned as mentioned by Huppmann (13). He found that forging forces for iron powder preforms are very low below the γ to α transformation temperature. This means significant savings in heating, die wear and oxidation. Bargainnier and Hirschhorn (1) studied the possibility of combining sintering process with hot forging and thereby saving the reheating process. They could obtain the same

results when forging at the higher temperature only (1100°C). Also they noticed that surface cracking and oxygen levels were decreased and carburization depth increased*. Maclean, Campbell and Dower (14, 15) investigated the difference in the properties of hot forged material depending upon whether it was sintered before hot forging or not. They could obtain comparable results to conventional materials by full sintering followed by either hot forging at 950°C with substantial deformation (30%) or by restriking at 1150°C with limited deformation (10%). They stated that for maximum impact resistance, full sintering must be employed. Also, when sintering is omitted and high tensile strength is required, very high forging temperatures (1150°C) must be reached.

The deformation which takes place as a result of forging not only densifies porous materials but may also result in work hardening. Such deformation may induce compressive stresses as well as tensile stresses which tend to open the pores rather than closing them unless the material is strong enough to sustain the tensile stress. Obara, Nishino and Saito (7) studied the deformability of three kinds of iron powder using forward, backward and complex extrusion processes which induced gross deformation. They could obtain satisfactory results and densities exceeding 99% at reductions higher than 60%. Bockstiegel and Bjork (16) in a dissociated ammonia atmosphere.

studied the influence of preform shape on material flow and residual porosity in hot forging of iron compacts and observed a good material flow when complicated shapes were considered and that simpler preform shapes may lead to better forgeability results, ie, lower load and higher density. Downey (17) carried out extensive investigation into the effect of preform shapes and modes of deformation on material flow and fracture. Aren (18) successfully hot forged iron preforms into a gear profile. Iron compacts are also adaptable to rolling. Billington, Fallas and Torabi (19) hot rolled iron compacts of three densities and concluded that there are three stages in deformation: restacking and rearrangement, local plastic deformation and bulk plastic flow leading to grain elongation and recrystallization.

The main theme of most of the previous work was to achieve a high density level when the forged material reached its final shape. Huseby and Scheil (9) found that a forged density of steel above 98% is very important for ultimate properties. In their tests, ductility and notch bar impact strength dramatically increased near full density.

Bargainnier and Hirschhorn (1) observed in hot forging of steel that carbon and oxygen levels decreased with an increase in density. Furthermore, near full density could

be achieved even under cold forging conditions. Antes (3) concluded that by simple uniaxial upsetting or plane-strain compression of atomized iron and steel preforms full density may be reached provided that the preform density is not too low. Also, for a low preform density the load required to achieve a given density will be increased. Furthermore, he observed that a linear relationship exists between preform density and final density for a fixed type and amount of straining.

It was mentioned earlier that the properties of sintered and sinter-forged porous materials are mainly a function of density. This was reported by Antes (3) and furthermore, he observed that the increase of hardness with density is at a higher rate with forged billets due to strain hardening. A higher increase in hardness was obtained by Bargainnier and Hirschhorn (1) with carbon additions to the iron powder. Also they observed that the resultant hardness levels were relatively insensitive to the experimental variables, such as particle size, preform density and forging temperature in closed die forging of steel to full density. The hardness values obtained are comparable to those of solid material.

Cundill et al (6), Suzuki and Shimamura (11) and Amato et al (20) forged a variety of sintered iron and steel and

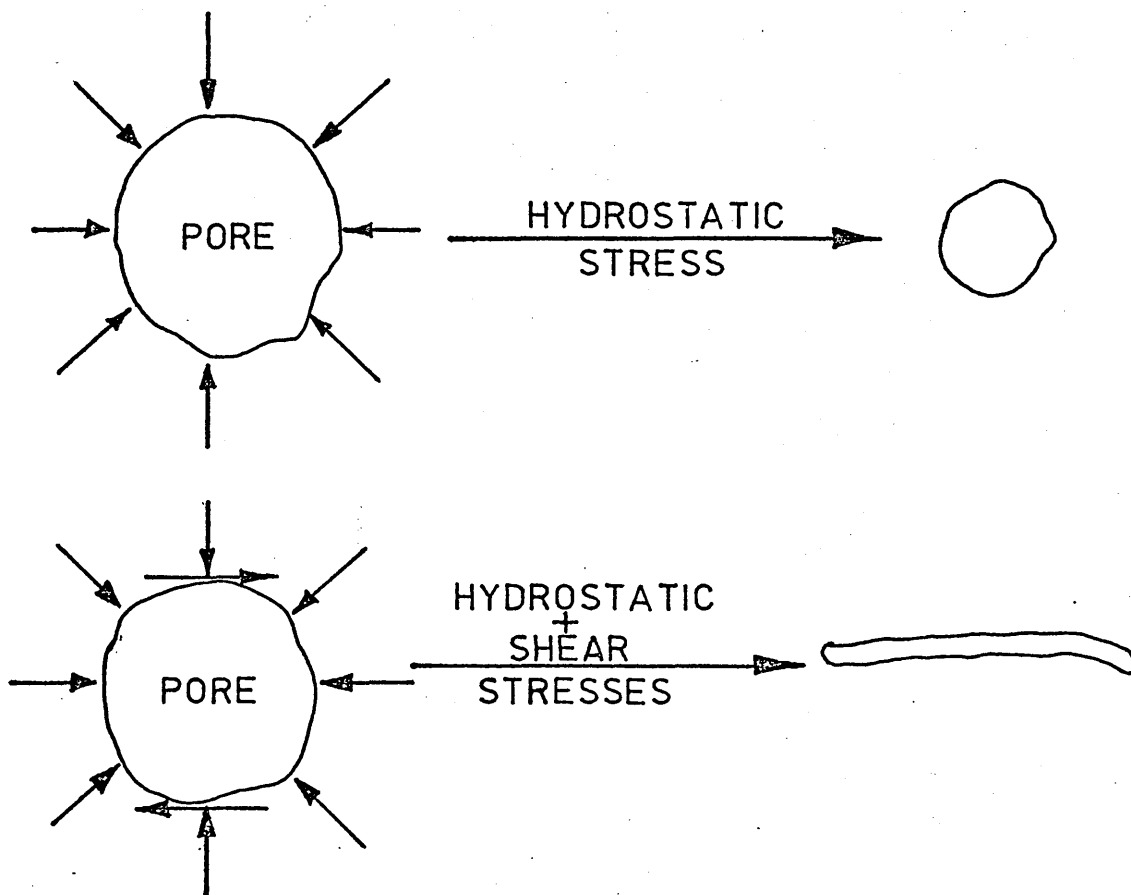
obtained comparable tensile strengths to those of solid counterparts either by hot forging, heat treatment or by using a good quality powder.

As for the property of impact resistance, it was improved by using finer powder particles (2), sintering at higher temperatures (21), and by deformation to full density (21, 22). Moyer (23, 24) reported a sharp increase in impact resistance when the density exceeded 98%, but it did not become equal to the impact resistance of wrought material (20). However, it decreased due to surface oxides (6) and oxygen contents in general (21). Antes and Stock (4) measured the impact and tensile strengths of hot powder metal formed Molybdenum steels and found them higher with upsetting than re-pressing, but ductility was the same for both.

1.2.2 Deformation Characteristics of Sintered Materials

The deformation mechanism of porous materials is mainly characterised by the closing up of pores which is the major difference from solid materials. There are two techniques to close up a pore, one by applying a hydrostatic stress only and thereby decreasing the volume of the pore but an infinite pressure would be required to eliminate it completely (25). The second mechanism is by combining shear stress

with the hydrostatic stress and as a result of this combination, pores flatten and close during deformation. These two mechanisms are explained diagrammatically as shown below.



The rate of densification is also affected by the kind of deformation (26). There are three basic kinds of deformation which, singly or combined, represent any forging process. These are: uniaxial strain (repressing), biaxial strain (plain strain) and triaxial strain (upsetting). Therefore, densification is expected to be higher with the upsetting

process because flow is higher (27). Parts produced by repressing usually have up to 2% residual porosity (26). The total amount of material flow has other advantages such as work hardening, directionality of grain structure and die filling.

Antes and Stock (4) and Moyer (23, 24) have clearly demonstrated that particle shear flow is indispensable for full toughness in powder forging, except with very low oxygen contents of the powder (28), and two causes are suggested (29):

- a) Sliding contacts promote bonding across void surfaces by breaking oxide films,
- b) Shear changes the geometry of voids, making them easier to collapse under compressive stresses. Both loose powders (30, 31) and sintered preforms (32) require much lower pressure to reach a given density if shear is enforced (27).

However, porous materials in general yield under lower stresses than fully dense materials. This is caused by the existence of porosity and by the nature of their grain structure prior to any deformation. Also, the material can flow inward (densification) and outward

(deformation) at the same time. This character, has another advantage, which is the reduction of the hoop stresses at the free bulging surface, hence, allowing higher reduction of height before fracture. However, the optimum condition in forming a porous material is to achieve final shape and full density simultaneously. Achieving full density is very important for the optimum strength conditions as mentioned in the previous section. The data obtained by Antes (26) indicates that forgeability, ie material flow and densification, increases with increasing preform density. It also indicates a trend of increasing forgeability with increasing temperature with the maximum forging temperature decreasing with decreasing density. Porous materials are very prone to oxidation at high forging temperature and oxidation decreases forgeability.

The ratio of the lateral strain to the axial strain in an uniaxial stress system is referred to as 'Poisson's ratio'. The value of this ratio for solid materials during plastic deformation is equal to 0.5, where the constant volume assumption is valid. Therefore this value is expected to be less than 0.5 for porous materials due to the densification which takes place during deformation, ie for the same axial strain, the higher porosity billets deform laterally less than the lower porosity billets. When full density is

approached, Poisson's ratio becomes 0.5 (ref 17, 21, 22, 33). Downey (17) and El-Wakil (21) reported that Poisson's ratio is only a function of the current density while Alkatib (33) and Hagerty (34) reported a decrease in Poisson's ratio at the early stages of deformation up to about 25% reduction of height followed by a uniform increase until full density was reached. This behaviour indicates a higher densification rate at the beginning of compression immediately following an initial process of particle sliding and rearrangement (33).

Speed of compression affects lateral flow, and consequently Poisson's ratio, by way of influencing the mechanics of densification, ie the mechanics of pore closure. At very low speeds (eg quasistatic compression) pore closure in the axial direction is accompanied with some degree of deformation in the lateral direction, hence densification and lateral flow proceed almost simultaneously. At higher speeds, conditions may be such that pore collapse is associated with little lateral deformation and consequently material may reach high relative density prior to being laterally deformed.

As impact speed increases, the stress level due to strain rate and inertia effects should also increase. Hence hydrostatic stresses induced into the system are increased

which in turn enhances densification and decreases lateral strain. Also high impact speeds increase interface friction which in turn enhances barrelling, this partly counteracting the densification effects of deformation. Fischmeister (26) reported that cracking tendency has been assessed by hot torsion, tensile and bending tests, and by the amount of barrelling that produces cracks when forging cylindrical preforms between flat dies. It decreases with reduced and faster deformation, presintering, tool lubrication and with lower preform density, but increases with oxidation. Downey and Kuhn (17, 35, 36) have developed a procedure to optimize preform dimensions for cylindrical forgings so as to allow maximum material flow while avoiding barrelling cracks, based on experimental and calculated (17) limit curves for crack formation. Another attempt to optimize the forging conditions of sintered sponge iron was carried out by Downey and Kuhn (66). They utilized a forming limit concept previously developed for cold forming of conventional materials (65). The approach involved comparison of surface strains, in the regions where fracture is likely to occur, with a fracture relationship for the material. It was found that fracture surface strains fit a linear relationship regardless of any other factors involved. Hence, when testing a model material, one can show how far from the focus the

model fails or how much further the material can be safely strained. Accordingly, the designer can adjust the preform or the die shape, or the friction conditions in order to avoid further fracture and complete the forming process with maximum strain hardening where required.

Nagawa et al (62) examined the cold forgeability of sintered billets of reduced iron in seven forms at three initial density levels. In general, they successfully cold forged the material, especially at high density levels and through narrow cavities. This latter point is of more importance to the designer of sintered components. For example, backward extrusion to form a thick walled cylinder and forward extrusion into a small orifice were successfully carried out, but high forging forces were required which lead to high densification before die filling, while in cases where the material was extruded through a relatively large die cavity, internal bursts and external cracks were observed (33, 62, 64).

Deformation of sintered billets of non-axisymmetrical cross-sections such as square, rectangular, semi-circular and triangular is not yet properly explored. In the absence of geometrical symmetry, the effect of interface friction on material flow becomes variable and consequently the

analysis of stresses and strains becomes very complicated. For this reason, fewer investigations have been carried out in this field on conventional materials and even less work has been carried out on porous materials.

An example of this work on solid materials is the investigation carried out by Aku, Slater and Johnson on plasticine to simulate the dynamic compression of prismatic blocks of hot metal (67). They forged prisms of the following shapes:- triangular, square, rectangular, square with central square hole and square with a square recess at one side. It appeared to them that the patterns for the cubes, the rectangular and triangular prisms were in agreement with Riedel's theory (68), ie, the two dead metal zones or pressure cones transmit the compression force to the material and this transmission takes place in a circular form so that the corners of the specimen are only affected indirectly by radial extension. Similar flow patterns have been observed by Kurrein (69) during the deformation of cubes and rectangular sections of rolled iron, hot-forged by a drop hammer, and by Johnson et al (70) during the slow compression of rectangular blocks of tellerium-lead and aluminimum between very rough, parallel, overlapping platens.

On porous materials, the author (33), in a previous investigation has thrown some light on the progress of deformation for prismatic iron blocks of square, rectangular and cross-shaped cross-sections during upsetting between smooth, parallel, overlapping platens with and without the use of lubricants. He plotted the progressive changes in profile and applied successfully the sand heap analogy to predict compression loads.

1.2.3 Plasticity Theories for Porous Materials

There have been many attempts to formulate the stress-strain relationship which governs the plastic deformation of porous materials. These attempts can be classified into two groups. The first is purely mathematical and based on a number of assumptions and conditions. The second is based on the findings of some basic experimental relationships which describe the effect of densification on the stress-strain relationship known from conventional plasticity theories.

Mathematical solutions are developed from the attempts to analyse a uni-pore element which represents a single cell in a porous body. Often many assumptions have to be made to simplify the solution. Storozhevskii (37) presented a number of possible models and selected a parallelepiped cell with an ellipsoidal pore for his solution. He assumed

that the volume of the porous body is made up of regular shaped elements or by their deformation (cubic, hexagonal, prism, rhombic dodecahedron, cubic octahedron ...) which fill the space without any gap or super-impositions. Also he assumed that all the pores have the same shape and size and are evenly distributed. Furthermore, model and pore have the same centre of mass (central single-pore model) and the cross-sections for which a solution by the relative relaxation method (38) was determined, are parallel to the co-ordinate planes. Kreher and Schopf (39) studied the relationship between the hydrostatic pressure and the mean pore volume of a porous body of a homogeneous non strain-hardening material with spherical holes. Applying Tresca's yield condition to the solid part with a yield stress in tension at a quasistatic loading condition and by using a self consistent method, results comparable to experiments were obtained. This method considers the interaction between different pores unlike the work carried out by Chu and Hashin (40) in which they suggested a composite sphere model where the pressure is acting at infinity and the material is composed of hollow spheres of constant material/pore volume ratio. On the basis of plasticity theory and using a Polytropic force relationship, Dorofeev (41) calculated the density distribution in powder blanks during dynamic hot free upsetting. He assumed the cylindrical blank to be a

composite of concentric cylindrical shells and claimed that the formula obtained gave good agreement with experimental data. Further description of the densification of a porous body during plastic deformation with allowance for work hardening was attempted by Skorokhod and Martynova (42) on two basis:-

- a) The mechanics of plasticity using a spherically symmetrical matrix model for a porous body and
- b) The root mean square viscous strains and stresses using a statistical model for a porous body.

The values of stresses obtained using the first method were higher than the second one. Mori, et al, (43) applied the rigid plastic finite element method for the analysis of forming of porous materials to predict the density distribution in axi-symmetric upsetting and plane-strain distribution. Equivalent stress and strain rate values given by empirical equations obtained from experiments were used in the solution. Haynes (44) investigated the effect of porosity on tensile strength of sintered materials in an attempt to establish a yield criterion for a minimum acceptable ductility where the least-highly stressed parts of a material should not exceed their yield point before the most highly stressed

parts reach their fracture stress. He derived a quantitative expression relating the yield stress/tensile strength ratio of the matrix material to the limiting porosity content. Applying the upper bound approach on a porous matrix of idealized geometry, Kahlow and Avitzur (45) investigated analytically (and experimentally) the effects of voids and their characteristics on the minimum effective pressure to initiate a permanent void volume change. Also, Shima, et al, (46) derived an upper bound solution and utilized it to estimate an approximate extrusion pressure and a final density ratio in a plane-strain condition.

The second group of solutions for the plastic deformation of porous materials ignores the geometrical analysis of cells and voids and instead is based on the empirical relationships between porosity and stress-strain characteristics of the sintered material during plastic deformation. The yield stress of porous materials (Y_o) is less than the yield stress of the solid matrix (Y) and with densification it increases until full density is reached. Hence, Y_o is a function of Y . Also, densification is usually accompanied by deformation of the solid matrix and consequently work hardening takes place which adds to the strength of the material. Furthermore, densification indicates that the hydrostatic stress component has an effect on yielding and

is a function of porosity too. Therefore, any yield criterion for porous materials should consider the aforementioned parameters. The conventional yield criterion by Von Mises states that 'yielding is a function of the second invariant of stress tensor only', and by including porosity functions, a modified relationship can be obtained. Along these lines investigators have recently proposed yield criteria for sintered materials. These criteria will be reviewed in some detail in a separate chapter and will be compared with the experimental results of the present investigation in an attempt to testify their applicability.

1.3 Objectives of the Present Work

The ultimate objective of this work is to provide the designer of sintered preforms for forging with the basic information about the physical and technical characteristics of the sintered iron preform and the processing variables respectively. Also to develop a theoretical solution for the basic modes of plastic deformation of porous material. Accordingly the programme is set to:-

1. Examine the effect of sintering time and temperature on the mechanical properties of the sintered billet before and after upsetting and on the flow and fracture characteristics.

2. Examine the effect of the sintered billet dimensions on flow and fracture at different friction conditions.
3. Examine the flow behaviour in some basic modes of deformation and determine the fracture limit.
4. Present useful nomograms of practical importance to the designer of sinter-forged components.
5. Modify the conventional Von-Mises theory of plasticity for solid materials by introducing porosity and work-hardening factors.
6. Modify the numerical analysis solution of M S J Hashmi for predicting boundary conditions of upset specimens and apply it to sintered materials.

CHAPTER 2

EXPERIMENTAL EQUIPMENT AND TEST PIECE PREPARATION

2.1 Materials

2.1.1 Powder

It was intended in this project to carry out the work on a powder mixture comparable to a mild steel wrought material and this was achieved by mixing pre-determined ratios of iron powder and natural graphite, no other alloying elements being added. Atomized iron powder, type AHC100.29, was chosen because of its high compressibility and purity and was mixed in a double cone mixer for a period of two hours with 0.25 mass% natural graphite. On sintering this gave a combined carbon content of approximately 0.2 mass% as shown in Figure (3.2).

The physical and chemical properties of the two powders are as shown in Table (2.1).

2.1.2 Lubricants

The following lubricants were used at different stages of the test programme:-

- (i) Zinc stearate powder, 3 mass%, suspended in benzene (C_6H_6), 97 mass%, for die wall lubrication during the compaction process.
- (ii) Polytetra fluorethylene (PTFE) sheets (teflon) of 0.125 mm thickness to achieve frictionless conditions in the compression of sintered billets.
- (iii) Natural graphite powder, 20 mass%, suspended in benzene, 80 mass%, for the compression of sintered billets under friction conditions comparable to those encountered in commercial forging practice.
- (iv) Tallow die lubricant for the closed die forging tests.

2.2 Tools

2.2.1 Powder Mixing Tools

A stainless steel double cone mixer of 1.25 l capacity was designed and manufactured for mixing the graphite powder with the iron powder. The rotating chuck of a cylinder grinding machine was used to hold the mixer and rotate it

at a speed of 40 rpm. Figure (2.1) shows a photograph of the mixer.

2.2.2 Powder Compaction Tools

The compaction units used in the present investigations are shown in Figure (2.2). These were designed to produce compacts with diameters of 15, 20 and 25 mm and with heights up to 40 mm. These diameters were dictated by the capacity of the existing compression machines, especially the 1000 kN Denison testing press. The larger unit was designed to produce compacts which could be machined to prismatic billets of various shapes but having cross-sectional areas equal to those produced by the smaller unit. This area, chosen for both types of billets, was 314 mm^2 . All units were of the floating die type, thus producing conditions of double end compaction. During compaction, the cylinder is initially supported by a rigid base which is removed after slightly pressurizing the powder which in turn holds the compression cylinder in position. The compression cylinders for all units and the punches were made of a high carbon, high chromium tool steel, hardened and tempered to 60 Rockwell C scale. For each unit, a mild steel ejection base in conjunction with the compression cylinder and the upper punch was used for the ejection of the compacts.

2.2.3 Sintering Unit

A special furnace was built to cater for the sintering prescribed for this experimental programme. This furnace, shown in Figure 2.3(a), was heated by means of four crystolon (silicon-carbide) heating elements positioned around and parallel to the central tube as shown in Figure 2.3(b). The elements were connected in series and supplied with power from a 240 volt AC supply. The nominal length of the zone was 710 mm and on calibration it was found that a uniform temperature could be maintained over a 230 mm length of this zone. Temperatures up to 1300°C were recorded. The furnace temperature was monitored by a thermocouple (13% platinum-radium) which was in contact with the outer surface of the central tube at the centre of the furnace and connected to an energy regulator and temperature controller. The energy regulator was used to reduce the heating up speed to one hour for the first 1000°C . The temperature controller was used to maintain the temperature at one level within $\pm 2^{\circ}\text{C}$. A second thermocouple was used to measure and calibrate the temperature inside the combustion tube. The combustion tube was inserted inside the central tube and projected outside each end by 76 mm so that wet tissues could be wound around it for maintaining these ends at lower temperatures. The two ends of the combustion tube

were fitted with insulation brick inserts and then plugged with rubber bungs. Bottled 5% hydrogen in argon gas mixture can then be introduced at one end of the tube and allowed to pass through the furnace, leaving through a needle tube inserted through the rubber bung at the other end. The needle tube in turn is then connected to a fine tube which leads into a water jar. This technique was very effective in maintaining a controlled atmosphere inside the combustion tube at a very small flow rate of the expensive gas. After charging each batch of compacts to be sintered, the gas was allowed to pass through at a high flow rate to replace the air inside the combustion tube, then the second end is plugged. To protect the two rubber bungs from burning, long tissue papers were wound around the two ends of the combustion tube and suspended so that their ends dipped in jars of water beneath them. Again this technique proved very useful in maintaining the two ends at comparatively low temperatures. All these arrangements are shown in Figure (2.3a).

2.2.4 Compression Machines and Tools

The following compression machines, special dies and fixtures were used at various stages of the present investigations:-

Compression Machines: Two standard testing machines were used. The first was a 1000 kN Denison Universal Testing Machine and the second was a 2500 kN Denison Press Model T.1.A machine. This second machine was used for the closed die forging tests. For tests carried out on both machines, the load readings were taken directly from the press dial and the displacement readings were taken by a dial gauge fitted on to the base and operated by the upper ram.

Tools: All forging tools and dies were manufactured from a high carbon, high chromium, tool steel with a ground finish for all surfaces to be in contact with the billets during testing. These tools are listed as follows:-

1. Two upsetting discs.
2. Two recessed discs with a 20 mm diameter x 5 mm deep recess at their centres.
3. Four hollow discs. Two with 10 mm diameter holes and the other with 12 mm diameter holes. For each pair, four entry radii of 1,2,3 and 4 mm were machined.
4. Triangular Cross-Section Forging Die Set

The set is composed of two punches and a compound compression chamber as shown in Figure (2.4). The inner part of the cylinder was made from hardened tool

steel material and a triangular cavity was cut using an electric discharge machine which used a spark erosion technique. The inner circle diameter of the triangular cavity is just above 20 mm and its height is 50 mm.

5. Multi-Cavity Forging Die Set

The set is composed of six pairs of punches, three pairs of profile inserts, three pairs of cavity divider inserts and a compound holder, as shown in Figure (2.5). Six combinations of cavity profiles can be obtained with this set. These combinations are shown in Table (2.2). The central cylindrical cavity was designed to take specimens of 20 mm diameter and up to 30 mm in height. The punches were machined using a numerically controlled milling machine.

2.3 Measurements

Generally, all the dimensional measurements were taken using a 0.01 mm micrometer and a 0.05 mm vernier. Weighing was carried out using a balance (Ohaus 310 g) accurate to 0.01 gm. This balance has an adjustable arm on which a beaker can be placed for the purpose of weighing suspended

specimens while immersed in water. The reduction in height of the test pieces during upsetting was controlled by using a 0.01 mm displacement dial gauge mounted on the press.

For measuring the profile of the test piece during upsetting and for obtaining the deformation pattern, the test piece surfaces were inscribed with a 2mm square grid, then a photograph of the test piece was taken at each step of compression using FP4 films of 120 ASA (see Figure (4.3)).

Impact, hardness and tensile fracture strength tests were carried out on specimens after sintering and also after deforming the specimen.

For impact tests, an Avery Izod impact testing machine of 13.56 Joules capacity was utilized. This machine was only suitable for testing test pieces of 12.5 mm x 12.5 mm cross-section, since the impact test pieces which could be machined from the sintered billets were very small, a special specimen holder was made to replace the original one. The dimensions of the impact test piece were proportionally reduced from the standard ones. These dimensions are shown in Figure (2.6).

In measuring the Vickers hardness number, machine loads of 5 and 10 kg were used for sintered and deformed conditions respectively. A set of vices were used to hold and position the specimens. The number of test points on each specimen was dependent on its size and they were generally 2 to 4 mm apart. Vickers hardness testing was found to give more consistent hardness values than standard Rockwell hardness testing.

For tensile tests a Hounsfield Tensometer and an Instron 1112A testing machine were used. The load was continuously recorded on a chart and the measurements were then read off the chart. The tensile test specimens were machined from billets before and after deformation and their dimensions shown in Figure 2.7, were dictated by the available sizes of chucks, the size of the billet and the ease of machining.

2.4 Test Piece Preparation

2.4.1 Powder Compaction

Compacts were prepared by firstly lubricating the die cavity and punch faces (die wall lubrication) using a spray of zinc stearate in benzene (section 2.1.2) and then left to dry. Meanwhile a pre-determined quantity of powder was weighed to an accuracy of ± 0.01 g. The die was assembled on the die holder and the powder was poured in the die cavity and tapped by hand. The upper punch was inserted

in the die and the whole assembly was placed at the centre of the press. The compression load was then applied (up to about 10 kN and then released in order to allow the die holder to be removed, then re-applied) gradually until the level for the required density was reached. The load was held at this value for five seconds and then released.

The die holder assembly was replaced by the ejection base, the load was gradually re-applied, and the ejection load was noted.

After each compaction run, the die cavity wall and punch faces were thoroughly cleaned and inspected for signs of distortion or deterioration. The lubrication was re-applied and the whole process repeated.

The dimensions of the compact were measured to an accuracy of ± 0.01 mm and used for density calculations. With the aid of displacement dial gauge, compacts of heights to an accuracy of ± 0.02 mm could be reproduced. Compacts having densities outside $\pm 0.05 \text{ kN.m}^{-3}$ of the desired values were rejected, and it was noticed that about 5% of the compacts had to be rejected. Figure 2.9 shows the compaction pressure-densification characteristics of the powder.

2.4.2 Sintering

In general, batches of 10 compacts were sintered at 1120°C and held for 60 minutes at temperature using the controlled atmosphere furnace described earlier in section 2.2.2.

The compacts were allowed to cool to room temperature inside the furnace. The flow of the hydrogen-argon gas mixture was maintained during the whole cycle of heating, soaking and cooling.

The weight and dimensions of each sintered compact were noted after grinding the two ends of each billet (sec 2.4.3).

From these measurements the density for each billet (sintered compact) was calculated and regarded as the basic value. There was a small change in density due to sintering, although there was a slight shrinking in volume, this was partly counterbalanced by a 0.1 mass% loss of carbon.

2.4.3 Machining

Whenever required, billets were machined without using any coolant. All the sintered billets were initially ground to ensure parallel and clean ends and an equal height.

The compacts were produced with an extra height of 0.2 mm to cater for this grinding operation.

Further machining was carried out to produce:-

1. Impact test pieces (Figure 2.6) in the axial direction of the sintered billets and in the lateral direction of the upset billets with their narrow sides in the vertical direction.
2. Tensile test pieces (Figure 2.7) in the axial direction of the sintered billets and in the lateral direction of the upset billets.
3. Hardness test pieces by sectioning the billet exactly at its centre in the axial direction and then grinding it. Also grinding a 3 mm wide strip along the curved surface of the test piece and in parallel to the sectioned surface.
4. Prismatic test pieces of square, rectangular and triangular cross-sections. It was ensured that these test pieces were obtained from the central position of the sintered billets, where possible, by machining equal parts from all sides as shown in Figure 2.8.

2.4.4 Metallographic Examination

Sectioned specimens in the sintered and upset conditions were polished and etched in 2% nital and photographs of the grain structure were taken.

TABLE 2.1 - POWDER PROPERTIES

Powder Type	Apparent Density Mg/m ³	Flow sec/ 50 gm	Compress- ibility Mg/m ³ at 412 NM/m ²	Upper Particle Size Limit (Taylor- mesh)	H ₂ Loss %	Carbon Content Mass %	S Content Mass %	P Content Mass %	Ash Content Mass %
Atomized Iron Hoganas AHC- 100.29	2.9	25	6.65	100	0.1	0.01	0.025	0.01	
Natural Flake Graphite				-350		96-97			

Fig (2.1) Stainless steel double cone mixer

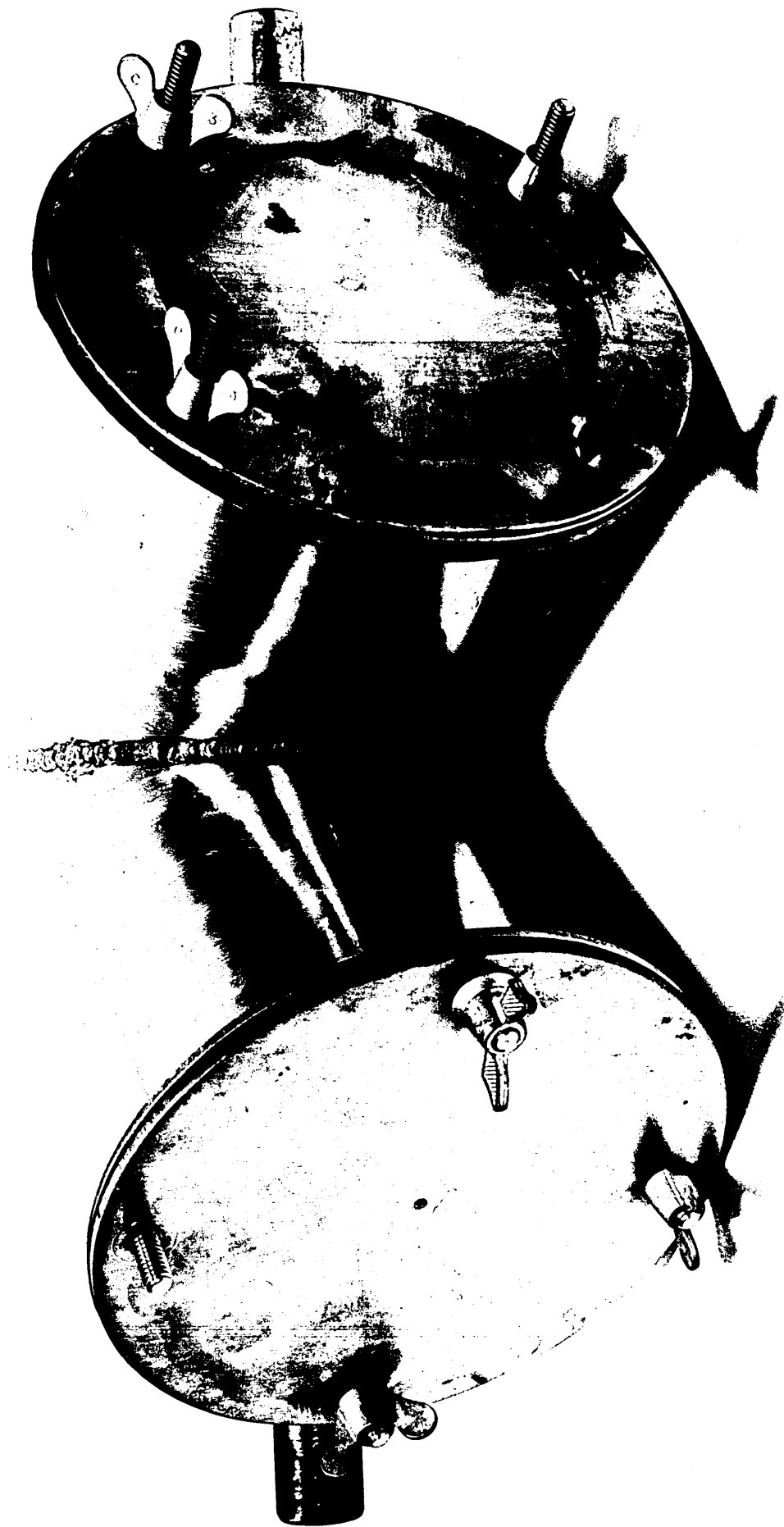
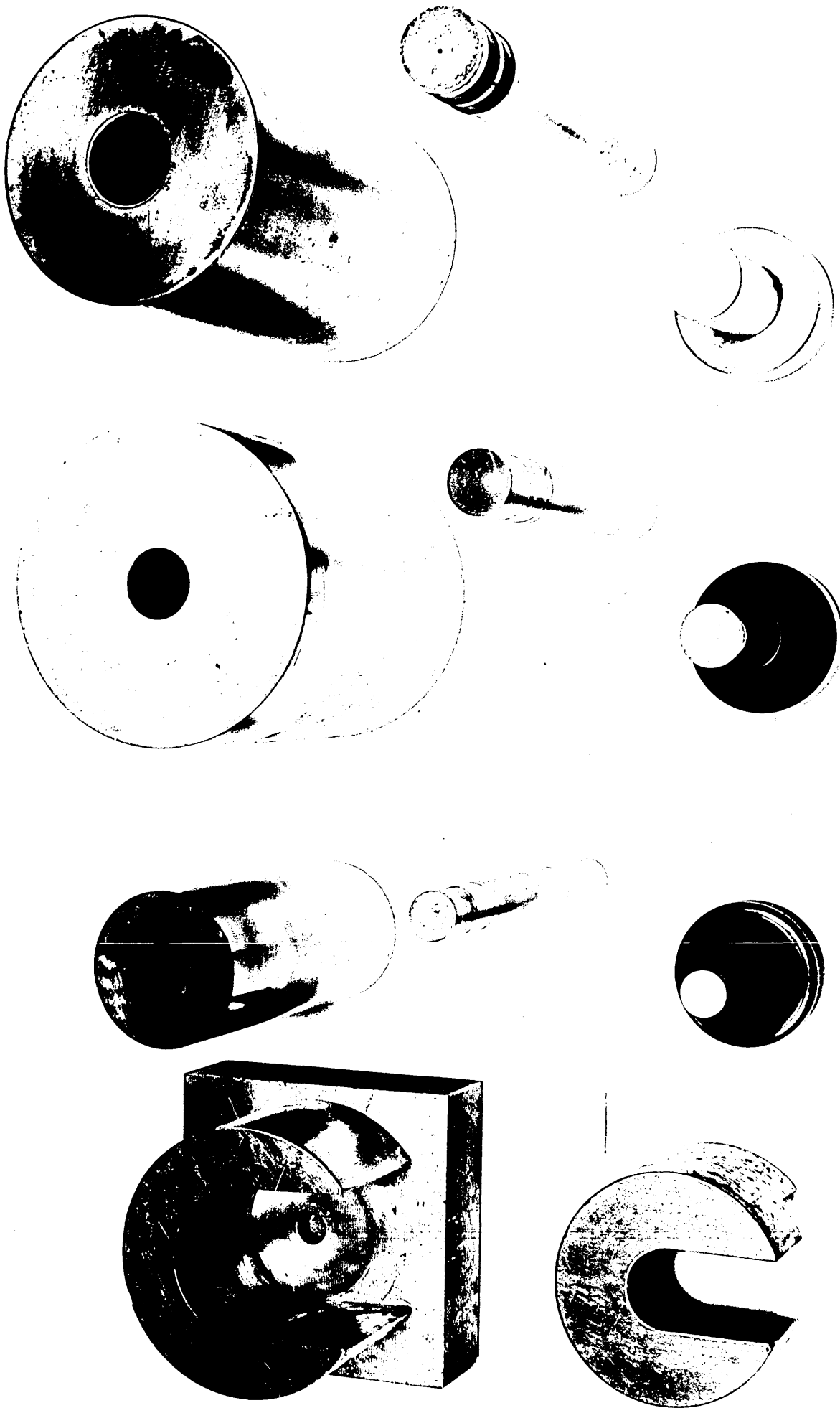


Fig (2.2) Three compaction units with two ejection holders and one assembly base
Each unit comprises a compaction cylinder, an upper punch and a lower punch



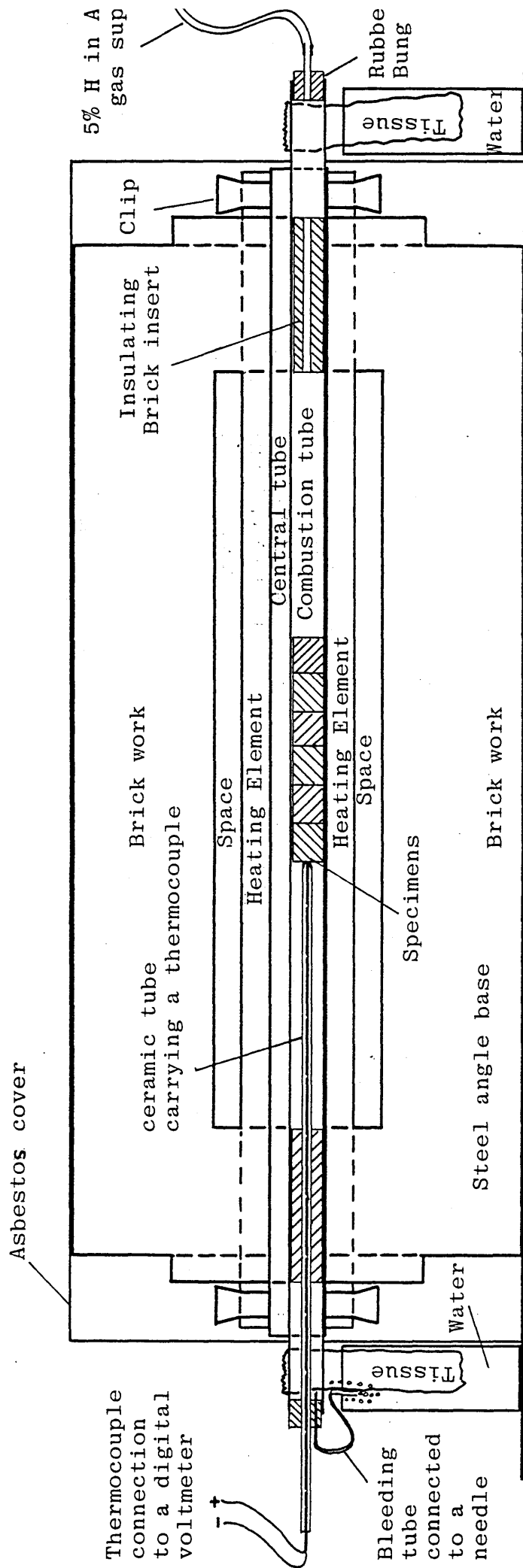
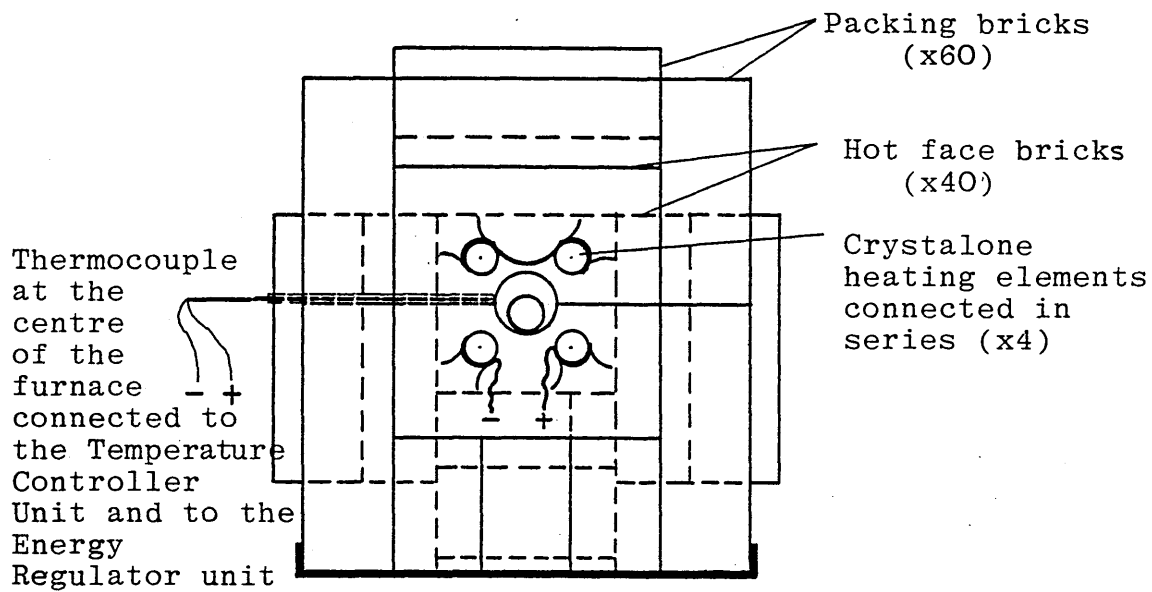
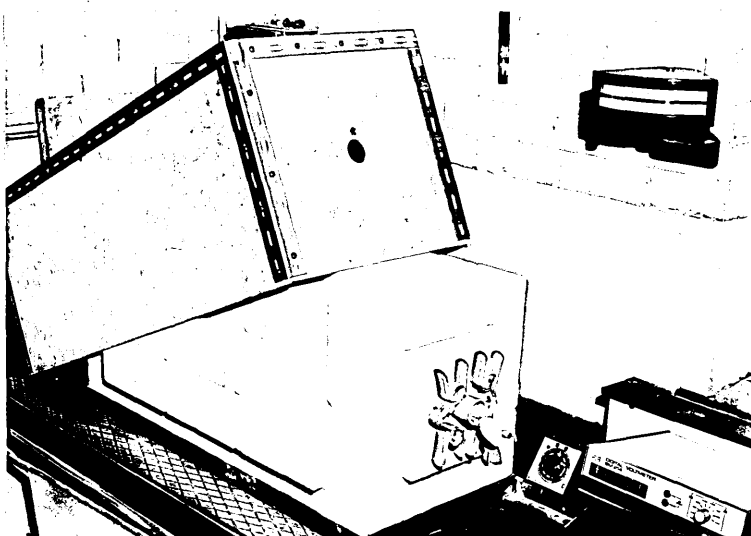


Fig (2.3a) Longitudinal cross-section of the sintering furnace (scale 1:5)



(b)



(c)

Fig (2.3b) End view of the sintering furnace

Fig (2.3c) A photographic view of the furnace

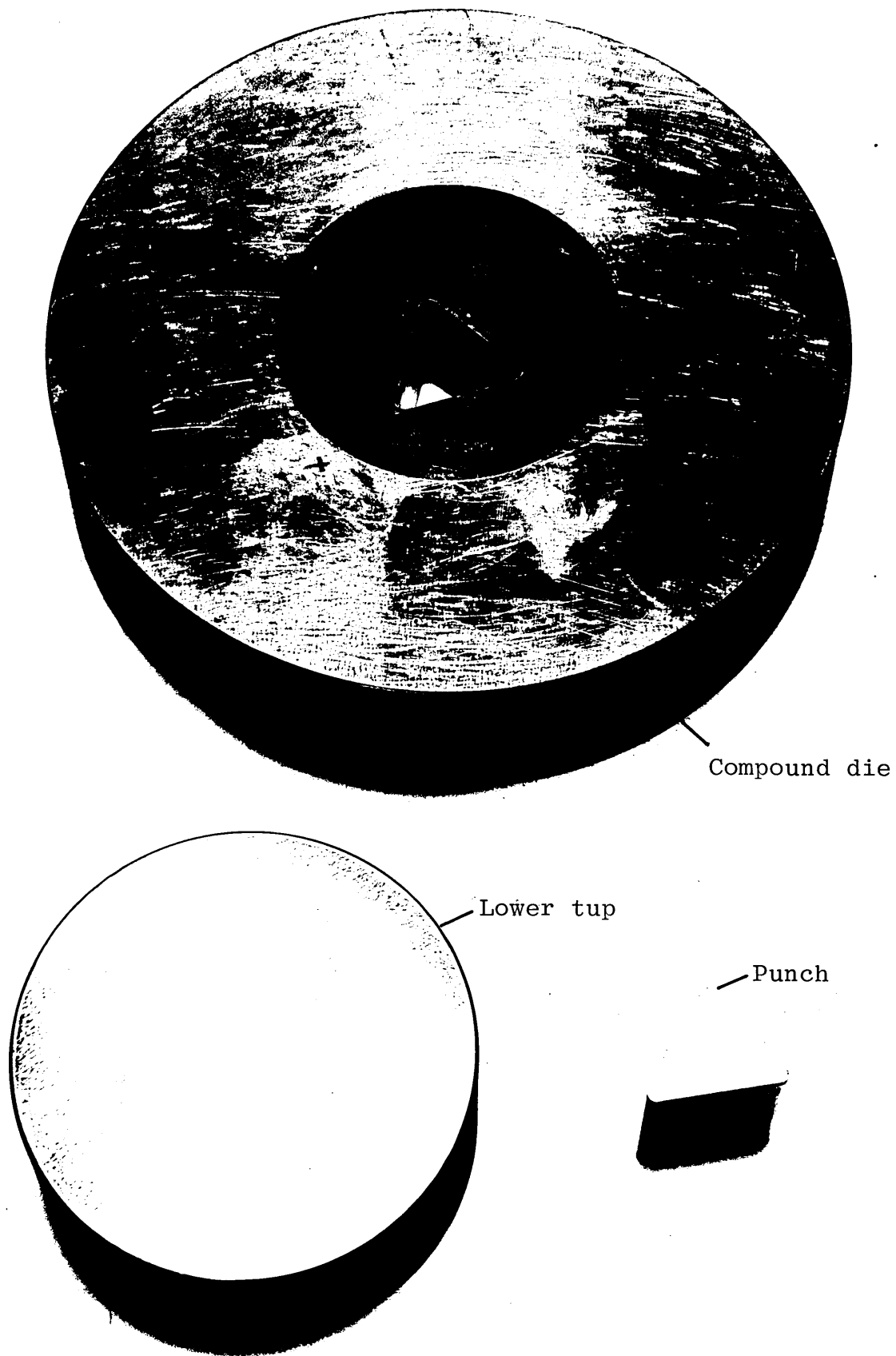


Fig (2.4) Triangular cavity die set

Compound
die holder

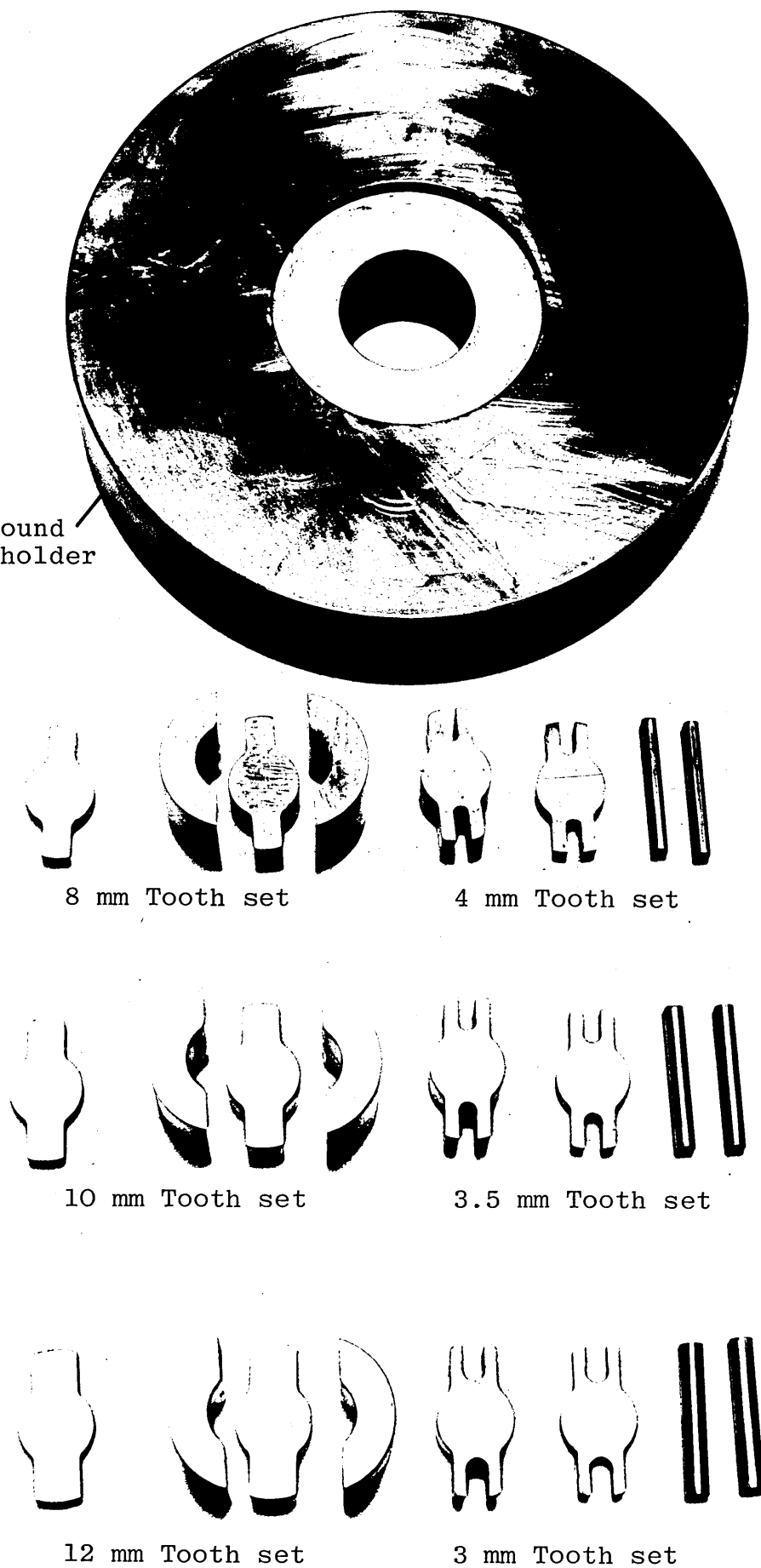


Fig (2.5) Multi-cavity forging die set

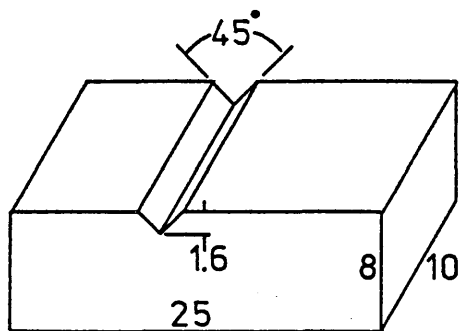
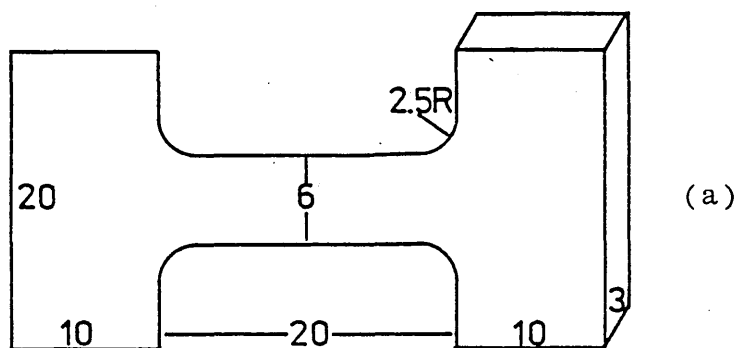
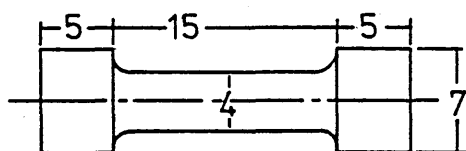


Fig (2.6) Impact Testpiece (Scale 2:1 mm)



(a)



(b)

Fig (2.7) Tensile testpieces (a) flat

(b) cylindrical

(Scale 2:1 mm)

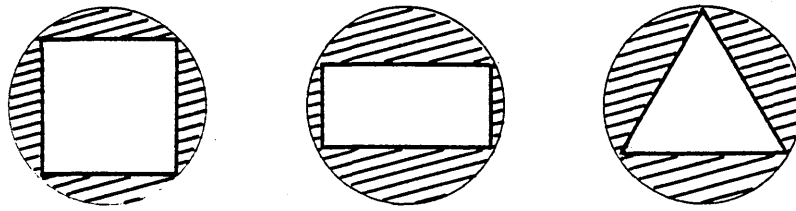


Fig (2.8) Prismatic testpieces, machined from the centre of cylindrical billets (scale 1:1)

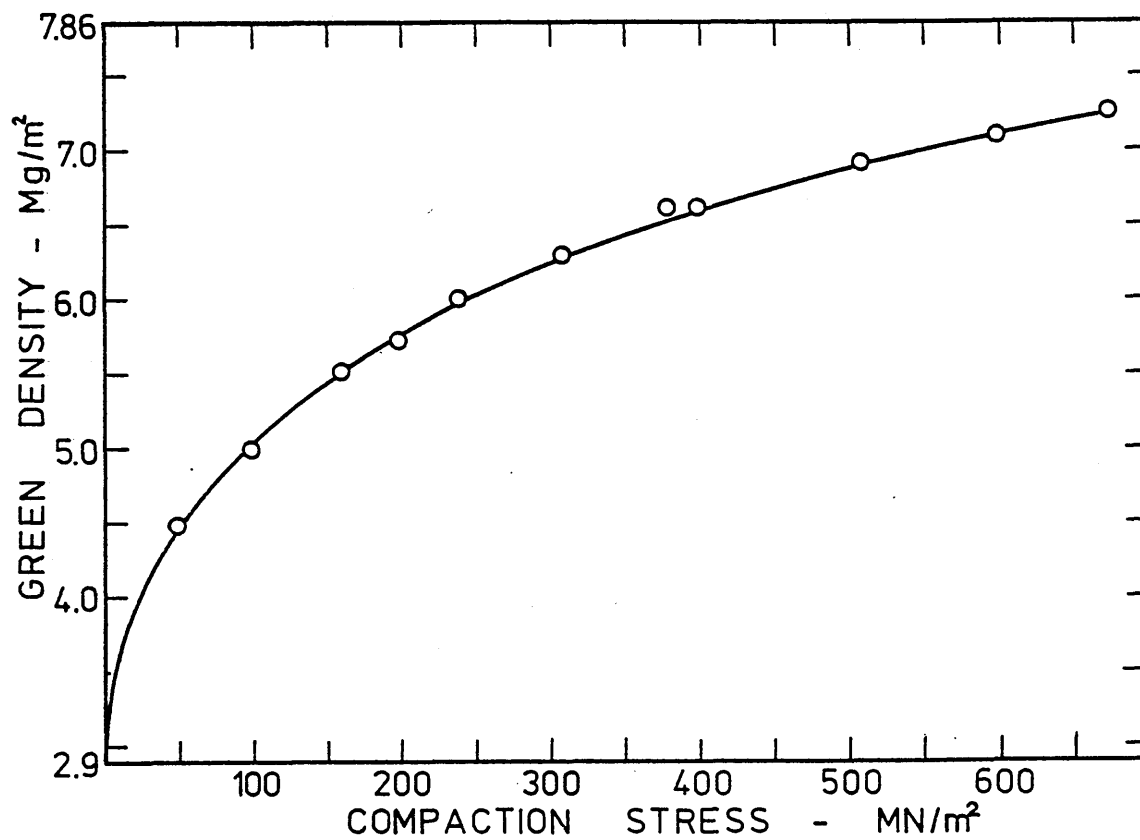


Fig (2.9) Green density-compaction stress relationship of atomised iron powder, using floating dies technique with die wall lubrication

CHAPTER 3

SINTERING CONDITIONS AND ASPECT RATIO

3.1 Introduction

Sintering is one of the major steps in the production of sintered components and it has considerable effect on the mechanical properties of such components since it influences the degree of diffusion between powder particles, the grain size and the status of alloys and phases of the material. In a controlled furnace atmosphere, the main two sintering parameters are time and temperature. The effect of increasing sintering time and temperature on the mechanical properties of sintered components have been reported in detail in references (10, 53-57). However, the effects of sintering time and temperature on the deformation characteristics and forged properties of sintered components need yet to be fully examined. For this purpose a wide range of sintering times (15, 30 60 and 120 minutes) and temperatures (900, 950, 1000, 1050, 1100 and 1200°C) were selected and the metallurgical and mechanical properties were examined before, during and after the upsetting process. Low and high density compacts were subjected to various mechanical and metallurgical tests to obtain data related to densification, lateral flow, fracture limit, Izod impact, toughness, fracture tensile

stress, Vickers hardness, grain structure, carbon in solution and level of oxygen content.

While sintering time and temperature are process variables, the aspect ratio of a sintered compact is a physical property of great importance. In forging of solid materials, where

volume constancy is applicable, the higher the aspect ratio, the more the material has to flow to achieve a given final aspect ratio. For sintered materials, densification takes place during the forging process, hence, for a given final aspect ratio, the initial aspect ratio must be higher than that for the solid material of the same initial diameter.

But changing the height and diameter results in changing the frictional effect between the specimen and the platens which consequently affects the densification mechanisms, the degree of bulging and barrelling of the free surface, the distance between the dead metal zones and the tendency to buckling.

Possibly for sintered materials, it is more important to state the lowest initial density (highest aspect ratio) from which the metal may be forged successfully without causing any fracture.

Therefore, it was planned to investigate in detail the effects of aspect ratio on upsetting specimens at room temperature of three initial densities (70, 80 and 90%) and seven aspect ratios (0.5, 0.626, 0.832, 0.993, 1.331, 1.754 and 2.326) at two interface friction conditions (graphite and no-lubricant).

3.2 Test Procedure and Results

3.2.1 Sintering Conditions

Using the 25 mm compaction unit, 25.2 mm long compacts at density levels of 70% and 90% were prepared and subsequently sintered at six temperatures (900, 950, 1000, 1050, 1100 and 1200°C) using four different soaking periods (15, 30, 60 and 120 minutes) at each temperature. Each specimen was then ground at both ends to achieve the same height (25 mm) and degree of end surface finish. These specimens were quasistatically upset at room temperature between polished flat platens with and without the use of 0.125 mm thick PTFE sheets as lubricant. When upsetting with lubricant the loading was interrupted to introduce a new PTFE sheet at equal intervals of reduction in height corresponding to the logarithmic axial strain of 0.2, 0.4, 0.6 mm etc). Records of load, current height and diameter obtained from these tests are shown in Table (3.1). During upsetting with

no lubricant, however, the tests were carried out un-interrupted until surface fracture could be detected by the naked eye.

Thus, maximum reduction was limited by fracturing of the specimen which indicates the effect of sintering conditions.

The resultant data is included in Table (3.1). Figure (3.1)

shows a photograph of a typical sample of a fractured specimen upset without using a lubricant and a typical sample upset using PTFE sheets as a lubricant. Chemical analysis was carried out on samples machined from the sintered specimens in order to obtain carbon and oxygen levels at various sintering conditions. These results are shown in Figure (3.2).

The fracture tensile stress and the impact toughness of the specimens were obtained as described in section 2.3 and the results are shown in Table (3.2).

For hardness measurements, a very lengthy test procedure was undertaken. A Vickers hardness testing machine was used to determine the hardness on the end-faces, sides and mid-longitudinal section of the sintered and upset specimens (see section 2.4.3). The resultant hardness values varied consistently in three zones (A, B and C) on each sintered specimen. These zones are illustrated in Figure (3.3) together with their hardness values versus sintering

temperatures. For upset specimens, such variation could not be observed and therefore the hardness measurements at the longitudinal cross-section were considered in this study and are included in Table (3.2) alongside those obtained from zone B for the sintered condition.

3.2.2 Aspect Ratio

The specimens were prepared using the three die compaction sets, hence, three initial diameters (15, 20 and 25 mm) were employed, and by changing the height of the compact, a large number of aspect ratios were obtained. The main parameters involved in determining the heights were the constant mass and the initial density at different aspect ratios. The volume of the specimens of 15 mm diameter x 35 mm height, 20 mm diameter x 20 mm height and 25 mm diameter x 12.5 mm height worked out to be nearly the same. Based on these heights, further specimens were prepared in order to investigate the effect of diameter at constant height and density, and the effect of height at constant diameter and density on deformation characteristics and fracture. All the compacts were sintered at 1100°C for 60 minutes. Most of the tests were carried out by upsetting the specimens to different reductions of height between polished flat dies without using a lubricant. The results are shown in Table (3.3) and a photographic comparison of

the profiles at various stages of compression is shown in Figure 3.13. Other tests were carried out by upsetting the specimens to fracture between polished flat dies with graphite as a lubricant and the results are shown in Table 3.4. For all these tests, at least two initial densities were considered. For upset specimens the maximum diameter was considered in the calculation of the final aspect ratio, since it represents the optimum lateral flow in closed die forging.

3.3 Discussion

3.3.1 Effect of Sintering Conditions

Study of the behaviour of sintered specimens before and after upsetting should indicate the effects of sintering time and temperature on deformation characteristics and mechanical properties. It is well established that during the sintering process, diffusion takes place at contact areas between powder particles. Additionally, there are rounding of pores, relief of internal stresses, grain growth, and in mixtures of iron and graphite, carbon alloying and carbon and oxygen losses. Most of these reactions would improve sintered properties if sintering time and temperature were to increase (53-57).

Upon examination of Figure (3.4), the yield stress of the sintered specimens is found to increase with sintering temperatures of up to 1100°C . This increase in yield stress may be attributed to the above mentioned diffusion and other factors. However, for sintering temperatures in excess of 1100°C as seen from Figure (3.4) a decrease in yield stress is evident. This softening is probably due to the grain growth (illustrated in Figure 3.5(c)) and increasing depletion of carbon and oxygen (shown in Figure 3.2(a) and (b)). Consequently, upsetting stresses were highest for sintering temperatures at around 1100°C as shown in Figure(3.7). This suggests that resistance to deformation is **greatest** corresponding to this sintering temperature. It may be noted that many investigators (4, 10, 58) have chosen to sinter iron compacts at around 1100°C to achieve optimum properties.

Stress-strain diagrams obtained from simple upsetting tests illustrate the resistance of the material to deformation. Figure (3.6) shows such stress-strain diagrams and it is evident from this figure that, the effect of sintering time on the deformation resistance is relatively insignificant and follows no definite trend. However, for a given density the resistance to deformation is seen to increase with strain in a consistent manner with each sintering temperature.

This statement may be supported by the fact that the slopes of the curves passing through the same temperature points within an envelope remains nearly unchanged. In other words, the rate of increase in the deformation resistance is unaffected by sintering temperature. This increase is attributed to densification and work hardening. It is evident from Figure(3.7)that, for a particular axial strain the deformation resistance represented by the upsetting stress is maximum at around 1100°C for both densities. At a particular axial strain of 0.6 the effect of sintering temperature on densification, as presented in Figure (3.8) which shows that for initial densities of 70% and 90% the average increase in the relative densities over the whole range of temperatures due to upsetting is around 16 and 8 percent respectively.

However, the curves do not show any maximum values at 1100°C in contrast to what has been evident in Figures (3.4) and (3.7). The relative densities obtained at 1200°C are seen to be higher than that at 1100°C . This behaviour is thought to be due to the mechanics of deformation in upsetting of porous materials. Here, densification and deformation may be said to take place either by sliding of powder particles or by collapse of pores. The first situation which occurs where the welds between the particles are weak as compared to the strength of the matrix, and the latter takes place

where the welds are reasonably stronger. The strength of these junctions between particles increases with sintering time and temperature as a structure of grains with normal grain boundaries develops but still containing porosity at the grain boundaries. Collapse of pores promotes densification, hence the continuous rise of density for sintering temperatures even in excess of 1100°C , and the corresponding decrease in lateral flow as shown in the same Figure(3.8).

The effect of sintering temperature and time on deformation to fracture is shown in Figure (3.9). It is clearly evident that for higher sintering temperatures and longer times, greater reductions in height are obtained before fracture initiates. It is also evident from Figure(3.9) that reductions of height ranging between 40% and 50% were possible without causing any fracture.

To determine the basic properties of the sintered and the upset compacts over the whole range of temperatures employed in this investigation, tests were carried out to determine the fracture tensile stress, impact toughness and hardness of the material.

From Figure (3.10) it is seen that the fracture tensile stress for both densities increases with sintering temperature irrespective of whether the specimens were upset or not. The

increase in fracture tensile stress, however, is more significant in the case of upset specimens and also with the specimens of higher initial densities. This indicates how sensitive the fracture tensile stress is to initial density and sintering temperature and consequently to the contact area between the powder particles. Initial density is a measure of the degree of contact between powder particles, and sintering temperature influences pore shape and grain boundary formation, pores becoming more rounded and less deleterious with the higher sintering temperatures.

The variation of impact toughness with sintering temperature, as shown in Figure (3.11), shows that impact toughness increases with temperature almost in the same manner as the fracture stress does. Here, it may be noted that the impact toughness for upset specimens is always lower than that for sintered ones. This behaviour might be reasoned as due to the fact that the material's hardness increases with deformation and consequently the material's toughness decreases. Also, the cross-section of the pore after upsetting becomes highly elongated with sharp tips acting as stress-raisers as shown diagrammatically on page 1.1 3 as an example and these, consequently, enhance fracture. Therefore, if full density is not reached by upsetting, as in the present case, the impact toughness would decrease. However, a sharp

increase of impact toughness at full density was reported by Downey (17) and Moyer (24).

It was found that hardness values varied slightly over the surfaces of the specimen, therefore, average values were taken in Figure(3.12) which shows that hardness increases due to upsetting, indicating the effect of densification and work hardening. However, in contrast to the effect of sintering temperature on the other properties, sintering temperature did not significantly affect hardness values for both the sintered and upset specimens. This is possible since hardness should decrease with grain growth, carbon losses and stress relief, whilst it would increase due to carbon alloying (pearlite structure)* and rounding of pores (stronger structure)*. The combined effect of these reactions may maintain the hardness of the material at the same level throughout the temperature range employed.

3.3.2 Effect of Aspect Ratio

The results presented in Figure (3.14), (a) to (c) show the variation of the fracture strain of the upset specimens with initial density, height and diameter respectively.

Figure 3.14(a) shows a substantial increase in the permissible lateral strain before fracture occurs with the increase in the initial relative density values from 70 to 90%. The largest

* as seen in Figure 3.5 (c).

lateral strain before fracture is obtained for the highest aspect ratio at all density levels. Also the rate of increase in lateral strain is highest with the highest initial aspect ratio. This behaviour could be clarified further by splitting the effects of initial height from initial diameter as shown in Figures (3.14 (b)) and (3.14 (c)) respectively where the lateral strain has increased with the increase of initial height and with decrease of initial diameter. Both of these conditions are represented by the highest initial aspect ratio in this series of tests. Consequently, the double effect led to a higher rate of rise of lateral strain at fracture in Figure (3.14 (a)). The results presented in Figure (3.14) were obtained from single tests.

Figures (3.15) (a) and (b) show the variation of axial strain with aspect ratio for initial densities of 70 and 90 percent, respectively. The limiting axial strain before fracture occurs, is also shown in these figures. This graphical information should be of use in design considerations for sintered components. Accordingly the following empirical relations were obtained for 90 and 70 percent densities using a statistical regression analysis of the experimental data.

$$\text{For 90\%} \quad \epsilon_a = 0.147 (A_{R0}/A_R)^{1.44} \dots\dots\dots (1)$$

$$\text{For 70\%} \quad \epsilon_a = 0.144 (A_{R0}/A_R)^{1.7} \dots\dots\dots (2)$$

In these equations, ϵ_a is the axial strain, A_{R0} and A_R are the initial and current aspect ratios respectively. The variation of upsetting stress with current relative density at different reductions of height and different aspect ratios is shown in Figure 3.16. It is evident that for given initial density, the effect of aspect ratio on the stress is rather insignificant. The experimental data in Figure (3.16) may be represented by means of an empirical relationship of the form:

$$\sigma = 629.3 \rho_0^{-0.73} \rho^{11.59 \rho_0^{1.98}} \dots\dots\dots (3)$$

where σ denotes the upsetting stress, ρ_0 and ρ are the initial and final relative densities respectively.

In Figure (3.17) the upsetting stress is plotted against the axial strain for various aspect ratios. It is seen that a higher upsetting stress is required for lower aspect ratios regardless of initial density.

Finally, the relationship between the initial and final aspect ratios over the entire experimental range is shown in Figure (3.18), where the solid lines represent the

following equations:

$$AR_o = 0.21 e^{4.67 AR_f} \quad \text{for} \quad \rho_o = 90\% \dots\dots\dots (4)$$

$$AR_o = 0.26 e^{3.23 AR_f} \quad \text{for} \quad \rho_o = 70\% \dots\dots\dots (5)$$

where AR_o and AR_f are initial and final aspect ratios respectively.

Comparing the computed results with the experimental data, it is seen from Figures (3.15), (3.16) and (3.18) that the empirical equations represent remarkably well the characteristics which include the variables such as the initial and final aspect ratios, axial strain, upsetting stress and initial and final relative densities of the sintered specimens.

With graphite as lubricant, deformation generally improved, hence, lower final aspect ratios could be achieved in comparison with the unlubricated case, as shown in Figure (3.18). The effect of graphite in these particular tests is comparable to the effect of increasing initial density from 70% to 90%, ie, the behaviour of 90% initial density specimens upset without a lubricant is comparable to the behaviour of the 70% initial density upset with graphite as a lubricant. Porous materials, in general, react

favourably with lubrication and the present tests are no exception. This characteristic adds to the versatility of using porous materials in forging processes.

ABLE (3.1a), UPSETTING RESULTS FOR 70% INITIAL RELATIVE DENSITY

int- ring emp C	SINTERING TIME - MINUTES											
	15			30			60			120		
	Load kN	Height mm	Dia- meter mm	Load kN	Height mm	Dia- meter mm	Load kN	Height mm	Dia- meter mm	Load kN	Height mm	Dia- meter mm
00	* 23	24.85	25.11	23.5	24.85	25.11	24.5	24.85	25.11	22.5	24.80	25.10
	90.4	20.35	26.79	87	20.36	26.79	88	20.35	26.80	88	20.30	26.82
	147	16.7	28.67	144	16.67	28.70	146	16.65	28.72	146	16.60	28.72
	219	13.63	30.88	215	13.16	30.82	216	13.63	30.74	217	13.61	30.78
	** 215	14.41	-	212	14.42	-	221	14.26	-	220	14.26	-
50	* 23.5	24.87	25.10	23.5	24.90	25.10	24	24.90	25.05	23.5	24.90	25.11
	87.5	20.35	26.79	87	20.38	26.81	89	20.38	26.72	86	20.40	26.75
	143	16.67	28.71	142.5	16.69	28.72	146	16.69	28.61	141.5	16.69	28.63
	211	13.67	30.69	212	13.63	30.72	217	13.66	30.59	209	13.68	30.57
	** 210	14.52	-	212	14.57	-	224	14.24	-	222	14.22	-
000	* 26	24.86	25.11	25.5	24.86	25.11	25.5	24.85	25.09	25.5	24.85	25.09
	99	20.36	26.78	96	20.36	26.78	97	20.35	26.77	94.5	20.35	26.76
	159	16.67	28.66	157	16.66	28.62	159	16.66	28.63	156	16.65	28.61
	235	13.66	30.79	233	13.65	30.70	235	13.64	30.80	231	13.64	30.71
	** 225	14.41	-	234	14.18	-	227	14.49	-	259	13.71	-
050	* 25.5	24.88	25.11	26	24.88	25.10	25.5	24.89	25.10	25.5	24.89	25.10
	96.5	20.39	26.78	94	20.38	26.76	92.5	20.39	26.76	95.5	20.37	26.77
	156.5	16.72	28.65	155	16.65	28.67	152.5	16.71	28.62	156.3	16.69	28.62
	235	13.64	30.61	229.5	13.64	30.64	229	13.63	30.58	235	13.64	30.63
	** 241	14.05	-	232	14.47	-	248	14.09	-	259	13.68	-
100	* 25.5	24.89	25.11	25.5	24.89	25.11	25.5	24.89	25.02	25.5	24.88	25.09
	94	20.39	26.78	96	20.37	26.77	95	20.37	26.66	93.5	20.37	26.76
	160	16.68	28.66	158	16.67	28.63	158	16.68	28.48	156	16.68	28.58
	236	13.66	30.65	233	13.65	30.59	237	13.65	30.43	233	13.64	30.53
	** 232	14.60	-	248	14.00	-	256	13.83	-	253	13.81	-
200	* 25.5	24.90	25.11	25.5	24.89	25.00	25.5	24.88	25.08	26	24.90	25.08
	95.4	20.39	26.75	98	20.11	26.78	92.3	20.36	26.74	93	20.39	26.72
	159	16.69	28.59	156	16.67	28.54	154.5	16.67	28.56	155.5	16.69	28.55
	236	13.67	30.53	234	13.63	30.43	231	13.64	30.48	232	13.66	30.45
	** 256	13.75	-	256	13.74	-	258	13.70	-	264	13.60	-

Yielding Starts
Upsetting without a lubricant till fracture.

TABLE (3.1b) UPSETTING RESULTS FOR 90% INITIAL RELATIVE DENSITY

Sintering Temp. °C	SINTERING TIME - MINUTES												
	15			30			60			120			
	Load kN	Height mm	Dia- meter mm	Load kN	Height mm	Dia- meter mm	Load kN	Height mm	Dia- meter mm	Load kN	Height mm	Dia- meter mm	
00	*	114	24.88	25.15	111	24.88	25.15	121	24.89	25.15	114	24.89	25.14
		185	20.37	27.39	186	20.36	27.40	185	20.38	27.38	186	20.38	27.38
		280	16.68	29.92	280	16.69	29.92	280	16.68	29.91	280	16.68	29.92
		392	13.68	32.61	391	13.64	32.69	390	13.65	32.69	391	13.64	32.70
	**	400	14.24	-	384	14.59	-	391	14.49	-	418	13.88	-
50	*	119	24.87	25.10	119	24.90	25.10	124	24.90	25.15	117	24.90	25.15
		187	20.34	27.34	185	20.38	27.34	188	20.38	27.39	187.5	20.37	27.41
		280	16.68	29.86	277	16.70	29.85	285	16.67	29.94	380	16.72	29.92
		387	13.66	32.61	387	13.63	32.60	393	13.62	32.66	390	13.67	32.67
	**	397	14.39	-	409	14.20	-	416	14.07	-	425	13.86	-
000	*	129	24.88	25.15	130	24.89	25.14	129	24.89	25.15	133	24.89	25.14
		195	20.39	27.38	192	20.39	27.38	195	20.38	27.38	191	20.38	27.43
		291	16.69	29.91	290	16.68	29.91	294	16.68	29.90	289	16.68	29.99
		408	13.66	32.65	404	13.65	32.69	410	13.66	32.64	404	13.64	32.80
	**	405	14.53	-	415	14.34	-	415	14.48	-	466	13.53	-
050	*	134	24.90	25.11	131	24.89	25.10	134	24.90	25.10	131	24.90	25.09
		201	20.39	27.35	196	20.40	27.34	199	20.30	27.34	200	20.39	27.37
		303.5	16.70	29.87	303	16.63	29.93	301	16.70	29.86	304	16.67	29.93
		422	13.69	32.56	417	13.67	32.57	421	13.62	32.60	426	13.65	32.53
	**	435	14.15	-	411	14.69	-	442	14.12	-	480	13.57	-
100	*	136	24.88	25.15	133	24.88	25.16	134	24.85	25.04	134	24.82	25.15
		208	20.38	27.37	203	20.37	27.29	199	20.35	27.31	195	20.30	27.37
		311	16.71	29.86	310	16.67	29.79	305	16.64	29.82	301	16.60	29.88
		435	13.69	32.54	429	13.65	32.40	422	13.64	32.40	419	13.62	32.54
	**	420	14.93	-	439	14.47	-	426	14.57	-	496	13.26	-
200	*	126	24.84	25.14	121	24.83	25.14	130	24.83	25.13	132	24.81	25.14
		203	20.34	27.38	203	20.33	27.37	198	20.33	27.38	195	20.31	27.25
		308	16.63	29.90	309	16.64	29.88	304	16.64	29.88	298	16.62	29.73
		429	13.63	32.53	431	13.63	32.49	422	13.63	32.53	417	13.61	32.37
	**	458	13.82	-	479	13.60	-	483	13.36	-	475	13.47	-

* Yielding starts

** Upsetting without a lubricant till fracture

TABLE (3.2) - MECHANICAL PROPERTIES

Initial Density %	Mechanical Properties	Sintering Temp. °C	SINTERING TIME - MINUTES							
			15		30		60		120	
			S	U	S	U	S	U	S	U
70	Ultimate Tensile Strength N/mm ²	900	72	94	76	91	79	91	81	108
		950	70	99	69	101	73	90	59	106
		1000	75	93	86	105	84	109	83	108
		1050	67	104	72	100	76	116	101	112
		1100	86	112	80	118	95	142	89	155
		1200	86	135	87	129	94	135	94	135
	Impact Toughness N.m	900	50	42	51	43	55	45	59	47
		950	53	42	55	47	62	48	73	46
		1000	57	49	66	57	77	53	92	56
		1050	68	51	84	49	99	55	117	63
		1100	90	51	102	54	140	63	145	63
		1200	105	62	123	63	151	68	182	72
	Vickers Hardness HV (5 kg)	900	36	76	33	77	32	78	33	80
		950	28	75	32	78	29	77	31	77
		1000	38	84	35	82	36	84	36	81
		1050	30	82	30	80	33	80	33	83
		1100	31	84	28	82	30	85	29	86
		1200	30	82	31	83	31	84	31	84
90	Ultimate Tensile Strength N/mm ²	900	203	277	212	346	211	385	216	425
		950		400	206	397	213	413	214	417
		1000	226	413	230	496	241	428	244	425
		1050	245	434	240	450	246	437	267	468
		1100	247	459	269	471	267	492	257	488
		1200	266	476	265	504	278	491		506
	Impact Toughness N.m	900	282	146	286	155	302	169	317	187
		950	309	153	330	164	360	161	370	206
		1000	357	200	383	186	410	256	438	286
		1050	418	249	454	285	500	320	546	343
		1100	525	300	570	403	625	387	695	387
		1200	558	406	597	410	655	434	713	438
	Vickers Hardness HV (10 kg)	900	66	151	65	151	64	152	64	152
		950	65	149	65	149	64	149	65	149
		1000	70	151	71	150	68	152	67	151
		1050	75	156	72	155	72	157	71	157
		1100	71	158	70	163	70	159	68	159
		1200	68	156	67	157	64	156	65	158

S = as sintered, U = as upset

TABLE (3.3) SIMPLE UPSETTING WITHOUT A LUBRICANT

	INITIAL CONDITIONS				TEST AND FINAL MEASUREMENTS				
Relative Density	Diameter mm	Height mm	Aspect Ratio AR ₀	Mass g	Load kN	Reduction % of Height	Aspect Ratio AR _f	Axial Strain	Lateral Strain
70%	15	12.5	0.833	12.22	115.3	50.2	0.319	0.696	0.217
		20	1.33	19.39	96.5	48.3	0.524	0.661	0.217
		35	2.33	34.01	127	57.3	0.695	0.85	0.303
	20	12.5	0.625	21.50	198	47.2	0.264	0.639	0.187
		20	1.00	34.03	175	46.6	0.417	0.628	0.199
		35	1.75	60.06	204	55	0.571	0.799	0.264
	25	12.5	0.50	34.10	306	40.5	0.252	0.519	0.142
		20	0.80	54.36	289	46.3	0.342	0.622	0.185
		35	1.40	94.88	289	51.1	0.511	0.715	0.244
80%	15	35	2.33	38.53	197	60.94	0.59	0.94	0.368
	20	20	1.00	38.97	263	48.5	0.384	0.663	0.246
	25	12.5	0.5	38.95	424	39.9	0.246	0.508	0.171
90%	15	12.5	0.833	15.69	243	54.3	0.260	0.784	0.333
		20	1.33	25.11	220	55.3	0.40	0.806	0.352
		35	2.33	43.95	281	64.8	0.488	1.04	0.472
	20	12.5	0.625	27.74	500	52.8	0.208	0.751	0.325
		20	1.00	43.91	355	49.8	0.355	0.69	0.299
		35	1.75	77.36	410	59.3	0.456	0.899	0.409
	25	12.5	0.50	43.84	626	42	0.225	0.545	0.223
		20	0.80	69.92	605	50.38	0.283	0.701	0.309
		35	1.40	122.27	570	55	0.422	0.799	0.355

ABLE (3.4) SIMPLE UPSETTING WITH GRAPHITE AS LUBRICANT

INITIAL CONDITIONS					TEST AND FINAL MEASUREMENTS				
ensity	Diameter Do.mm	Height Ho.mm	Aspect Ratio ARo	Mass g	Load kN	Reduction of Height R%	Aspect Ratio AR _f	Axial Strain	Lateral Strain
0%	15	12.5	0.83	12.26	140	56.9	0.26	0.841	0.323
		20	1.33	19.51	142	59.2	0.381	0.897	0.356
		35	2.33	34.13	148	61.4	0.600	0.952	0.402
	20	12.5	0.63	21.54	272	57.3	0.195	0.851	0.316
		20	1.00	34.52	286	60.4	0.278	0.926	0.357
		35	1.75	60.17	275	62.2	0.445	0.973	0.402
	25	12.5	0.5	34.22	548	60.4	0.141	0.926	0.340
		20	0.8	54.26	420	59.4	0.231	0.901	0.340
		25	1.0	67.77	385	56.8	0.313	0.839	0.322
		35	1.4	94.84	375	57.9	0.416	0.866	0.346
0%	15	35	2.33		CANCELLED DUE TO BUCKLING				
	20	20	1.00	39.15	376	59.3	0.278	0.898	0.385
	25	12.5	0.5	38.93	1000*	61.3	0.129	0.95	0.400
0%	15	12.5	0.83	15.7	310	60	0.215	0.916	0.438
		20	1.33	25.12	284	61.5	0.321	0.955	0.465
		35	2.33	43.9	341	69.4	0.397	1.184	0.584
	20	12.5	0.63	27.67	600	57.2	0.180	0.848	0.396
		20	1.00	44.35	586	61	0.249	0.942	0.451
		35	1.75	77.46	478	62.3	0.410	0.976	0.477
	25	12.5	0.5	43.64	1000*	56.7	0.147	0.836	0.390
		20	0.8	69.77	753	60.7	0.202	0.933	0.442
		25	1.0	87.17	724	58.1	0.274	0.871	0.418
		35	1.4	122.4	700	60.1	0.357	0.918	0.447

Press maximum loading limit, yet specimen did not fracture.

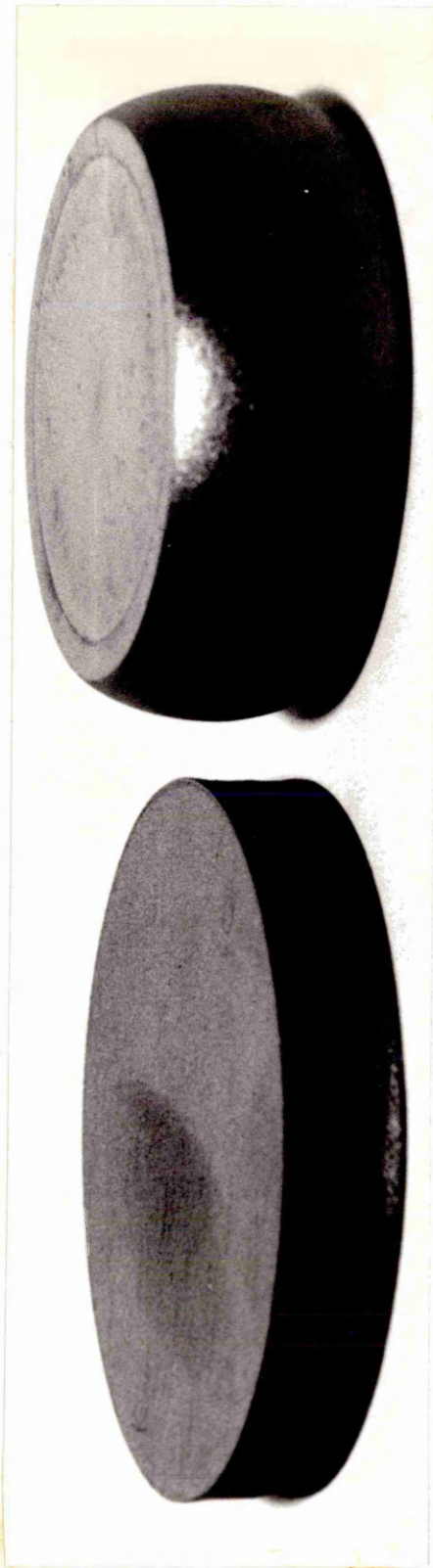


Fig (3.1) Samples of upset sintered iron specimens, left: with PTFE
as lubricant, right: without using a lubricant

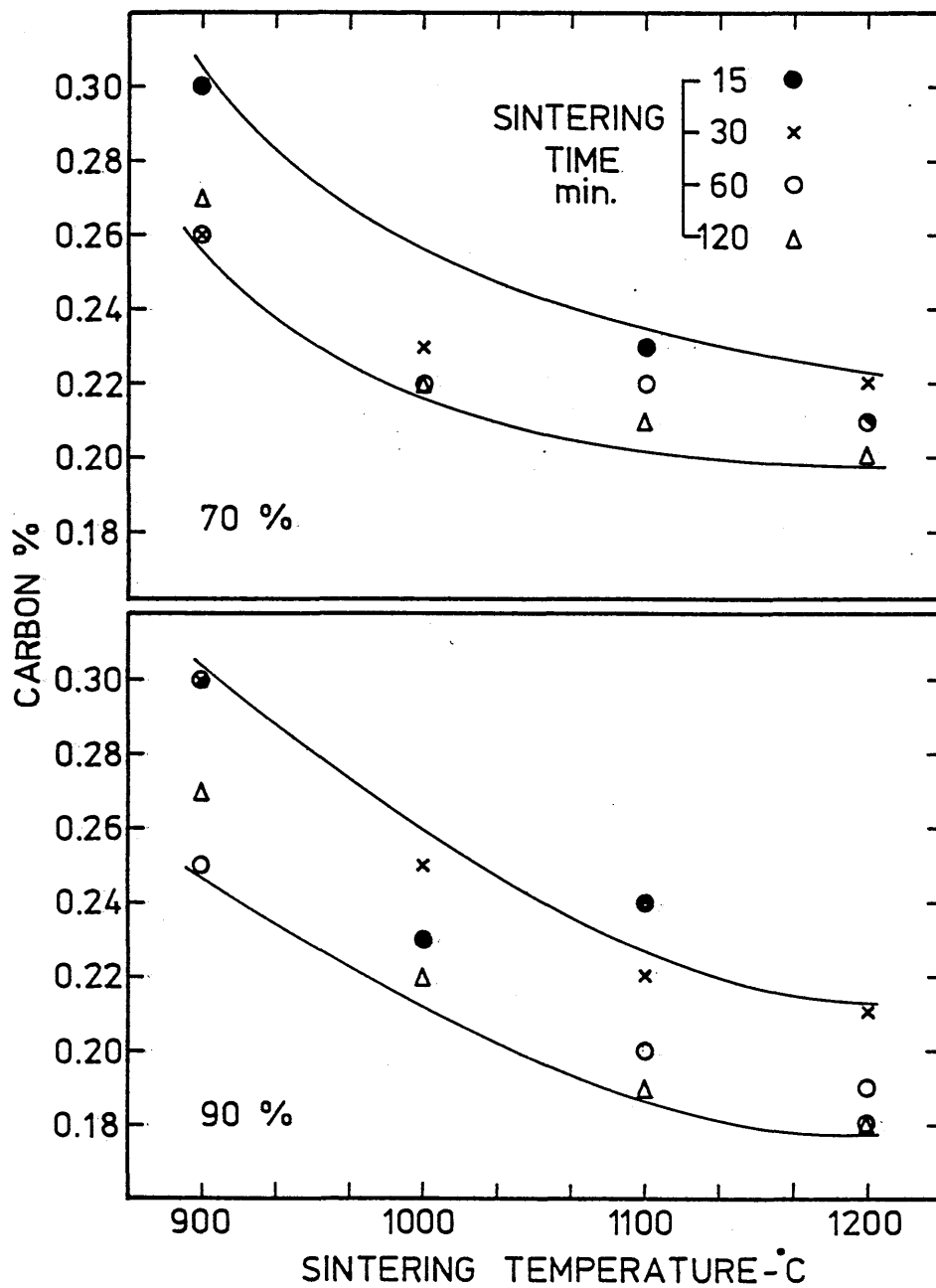


Fig (3.2a) Carbon losses v sintering temperature
at four sintering times

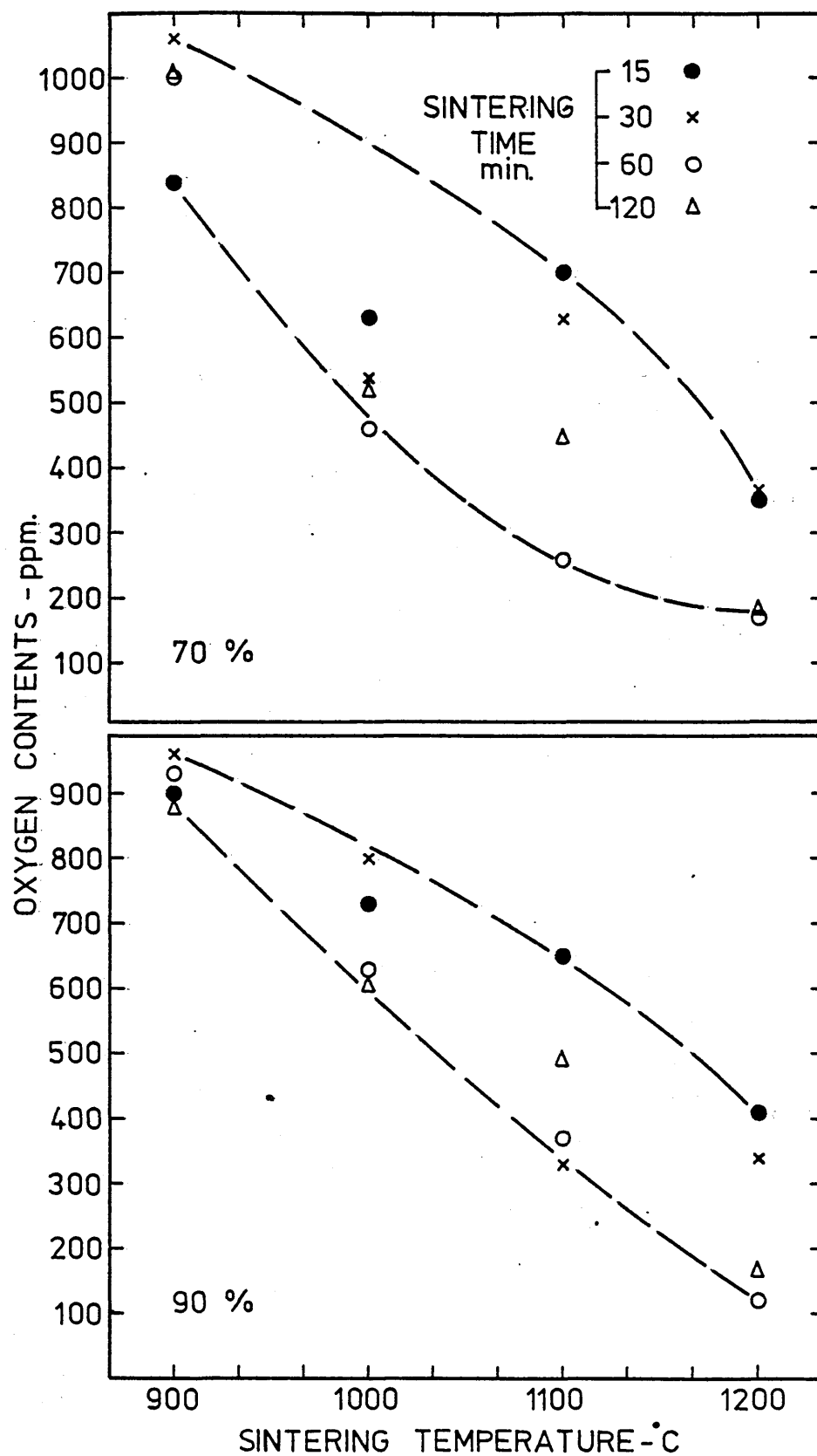


Fig (3.2b) Oxygen losses v sintering temperature
at four sintering times

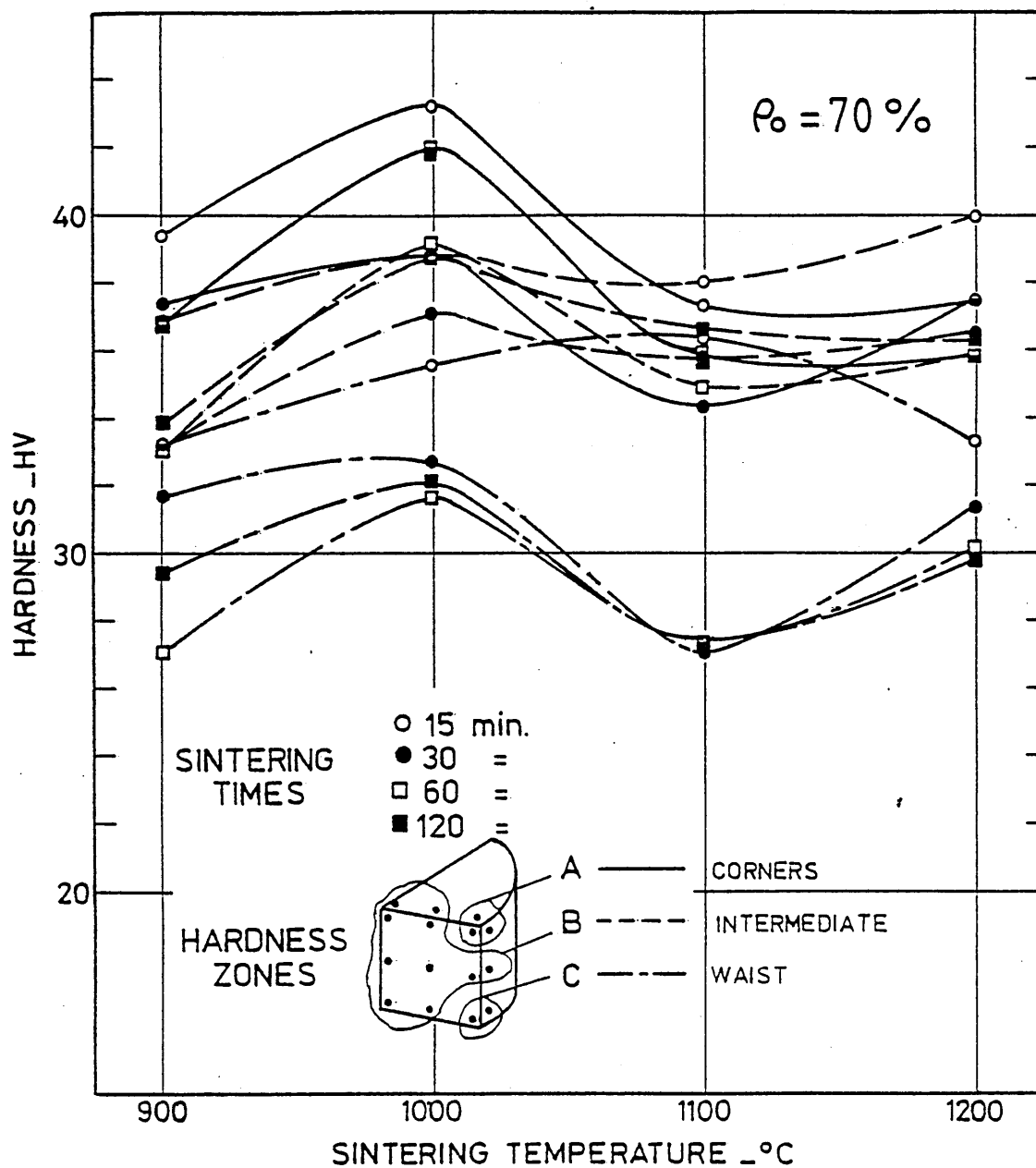


Fig (3.3a) The variation of Vickers Hardness throughout specimens of 70% initial relative density, sintered at various sintering times and temperatures

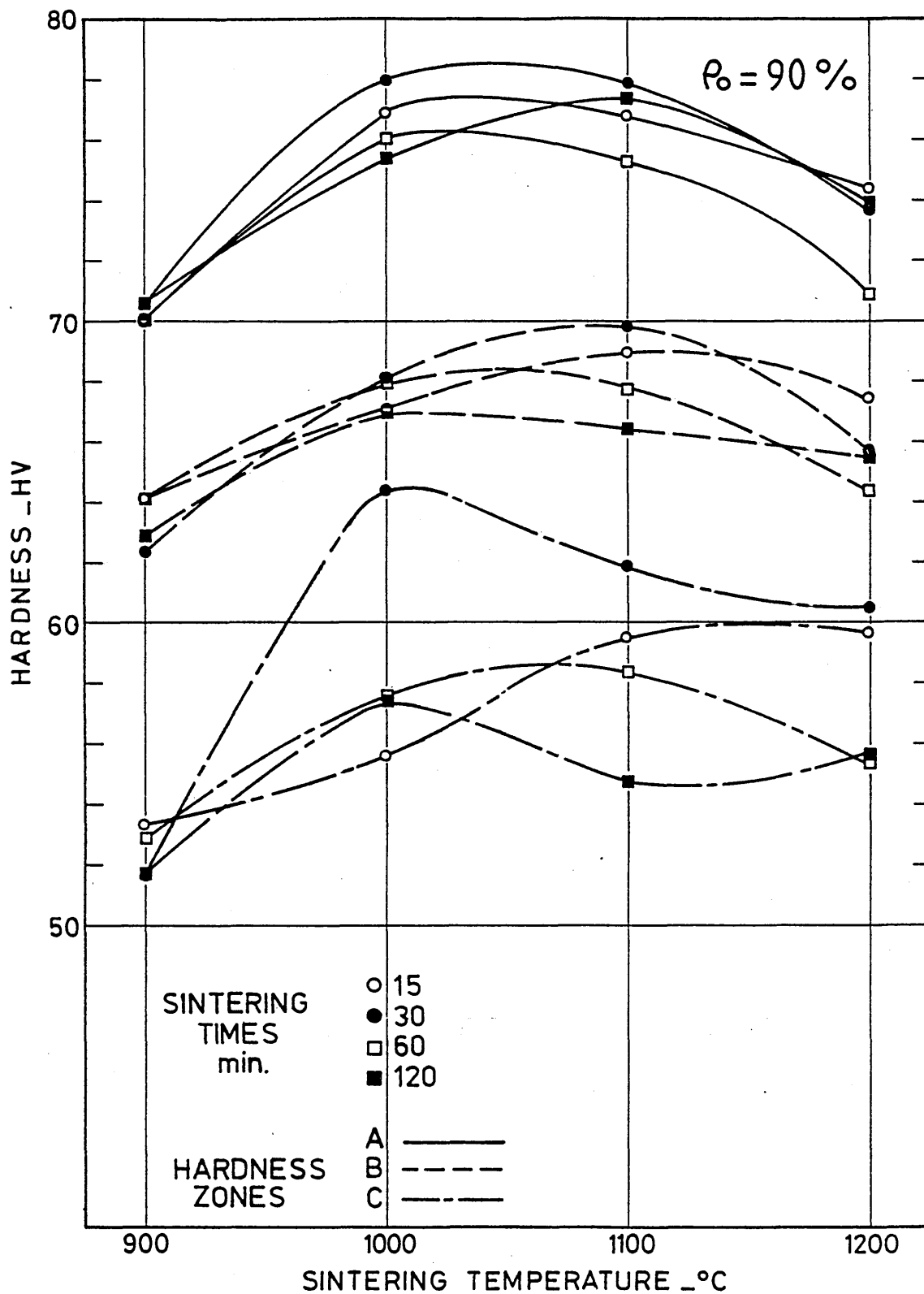


Fig (3.3b) The variation of Vickers Hardness throughout specimens of 90% initial relative density, sintered at various sintering times and temperatures

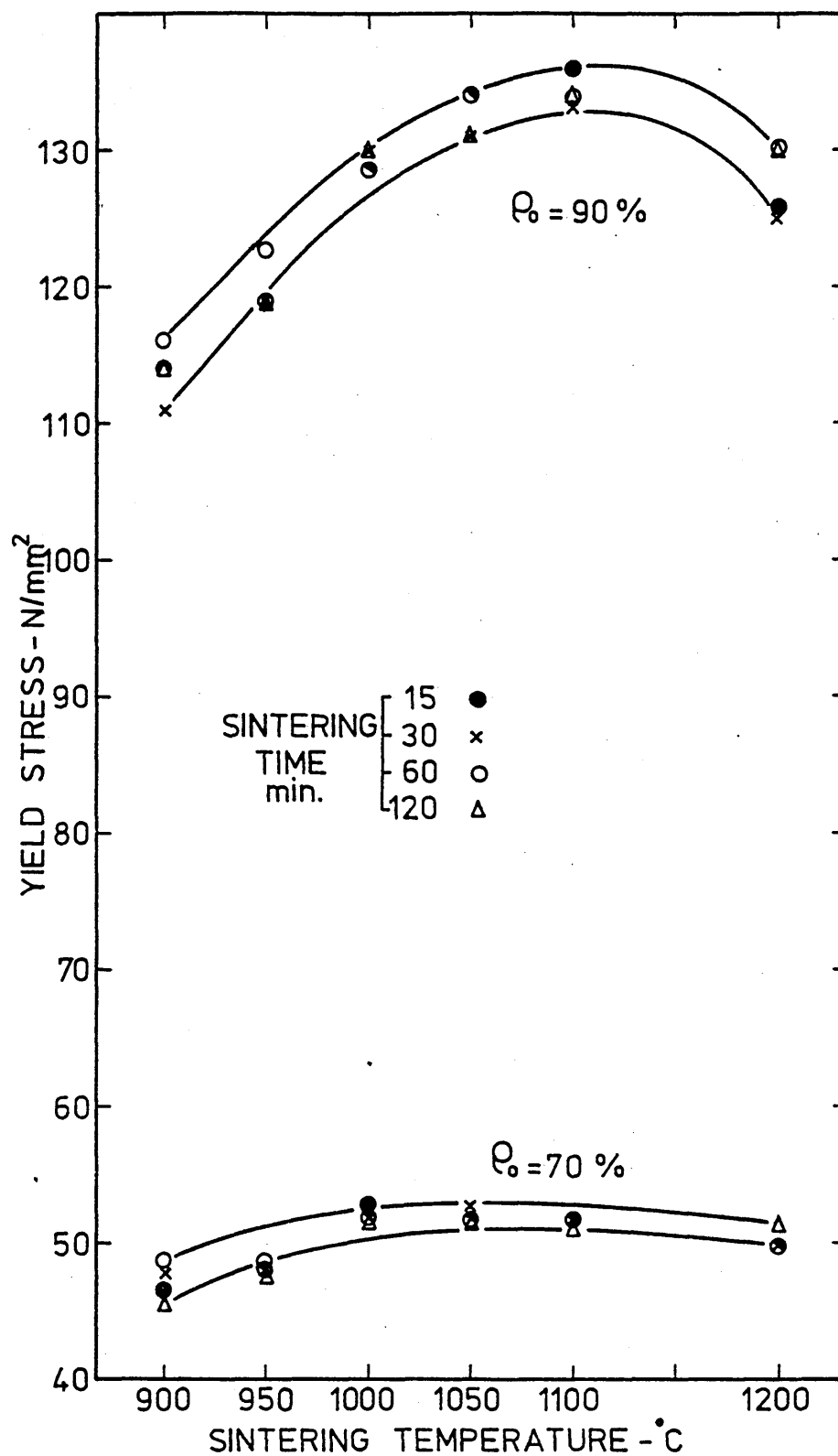
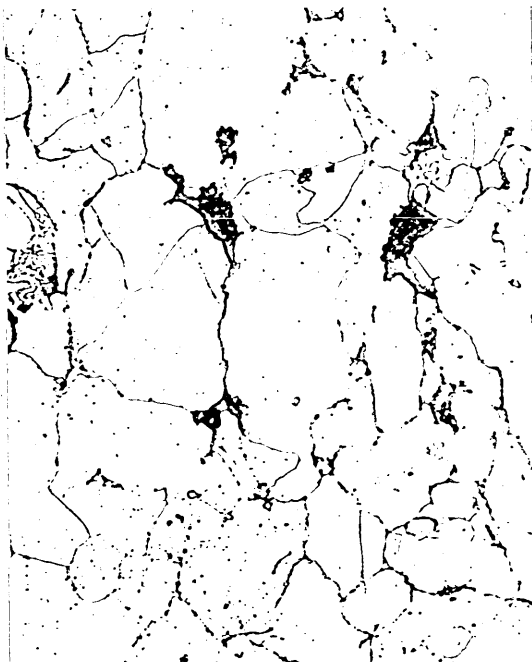
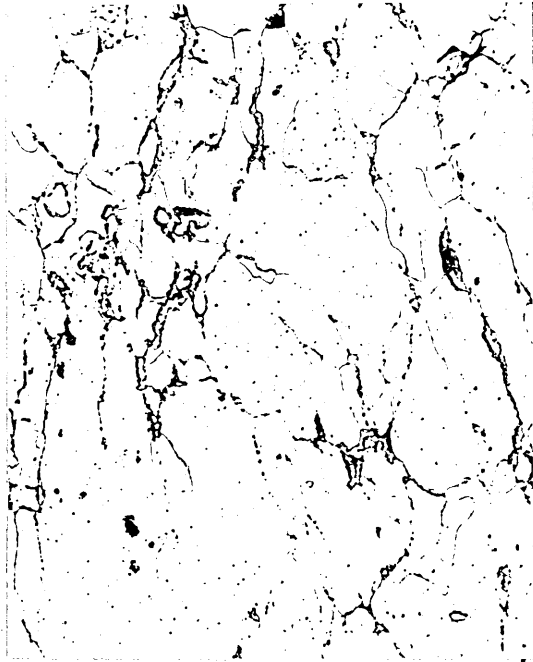


Fig (3.4) The effect of varying sintering time and temperature on yielding



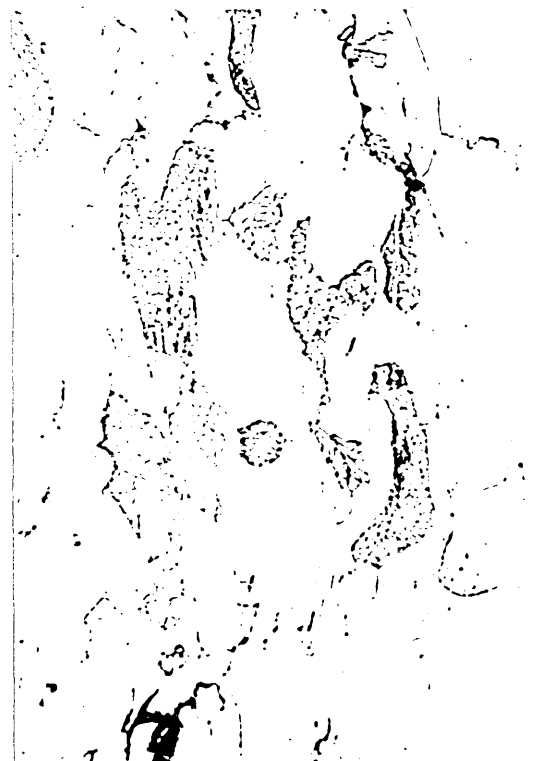
a) sintered for 15 min at 900°C



b) sintered for 15 min at 900°C then upset to 0.6 true axial strain



c) sintered for 120 min at 1200°C



d) sintered for 120 min at 1200°C then upset to 0.6 true axial strain

Fig (3.5) Metallographic grain structure for specimens of 90% initial relative density. Etched with 2% Nital. x 163 mag.

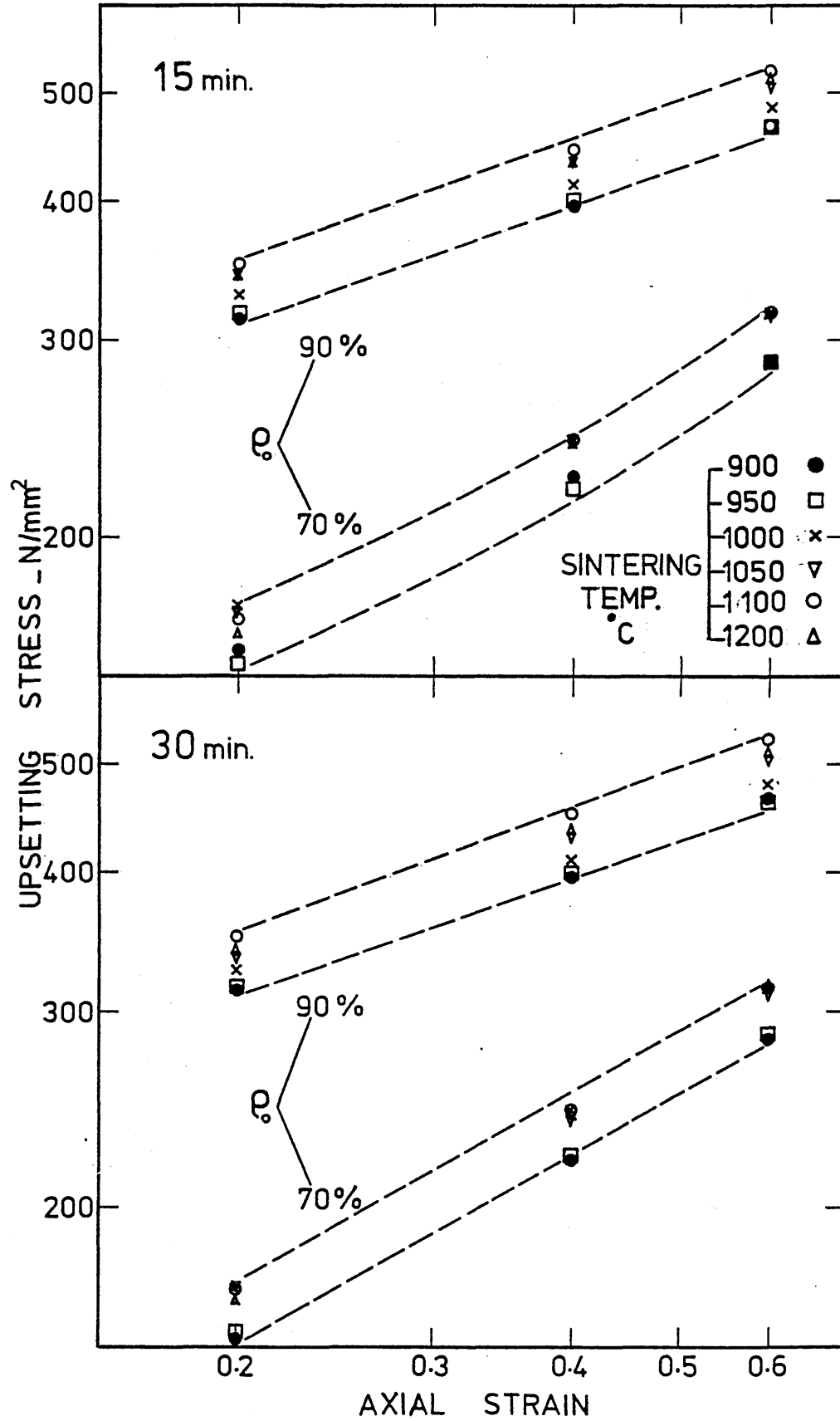


Fig (3.6a) The effect of varying sintering time (15,30 min) and temperature on the stress-strain relationship of sintered iron

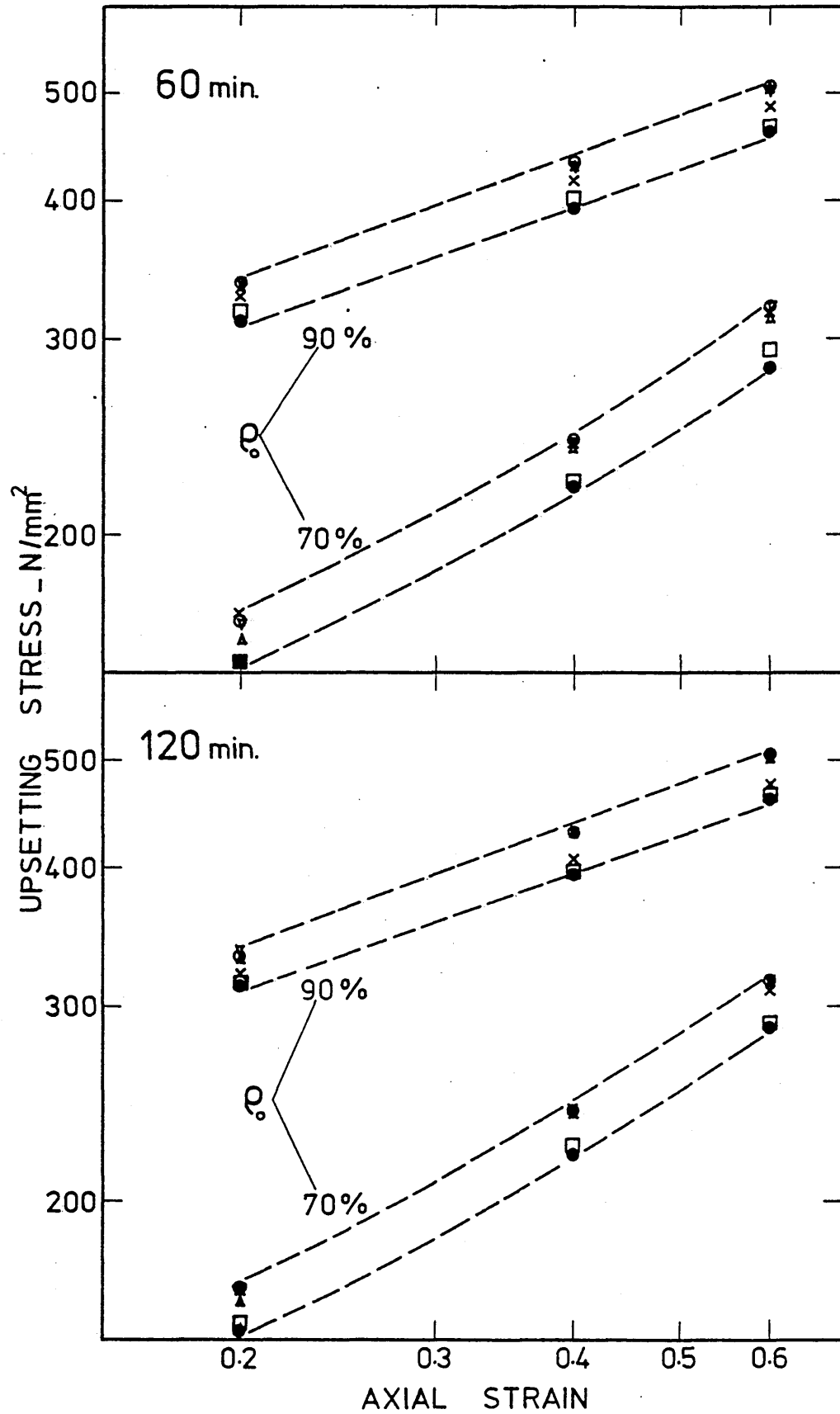


Fig (3.6b) The effect of varying sintering time (60,120 min) and temperature on the stress-strain relationship of sintered iron

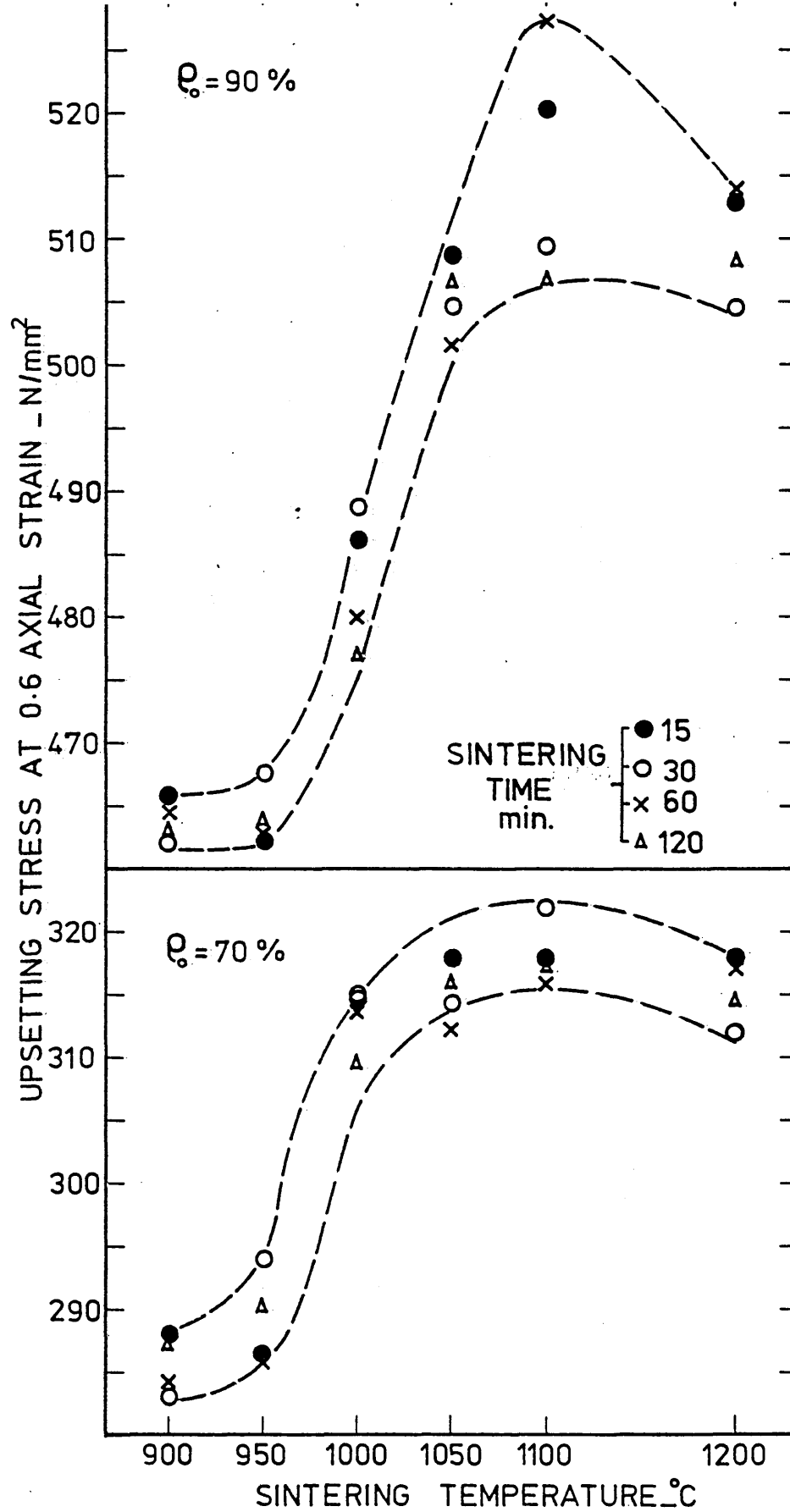


Fig (3.7) The effect of sintering time and temperature on upsetting stress at high reduction level for specimens of two initial relative densities

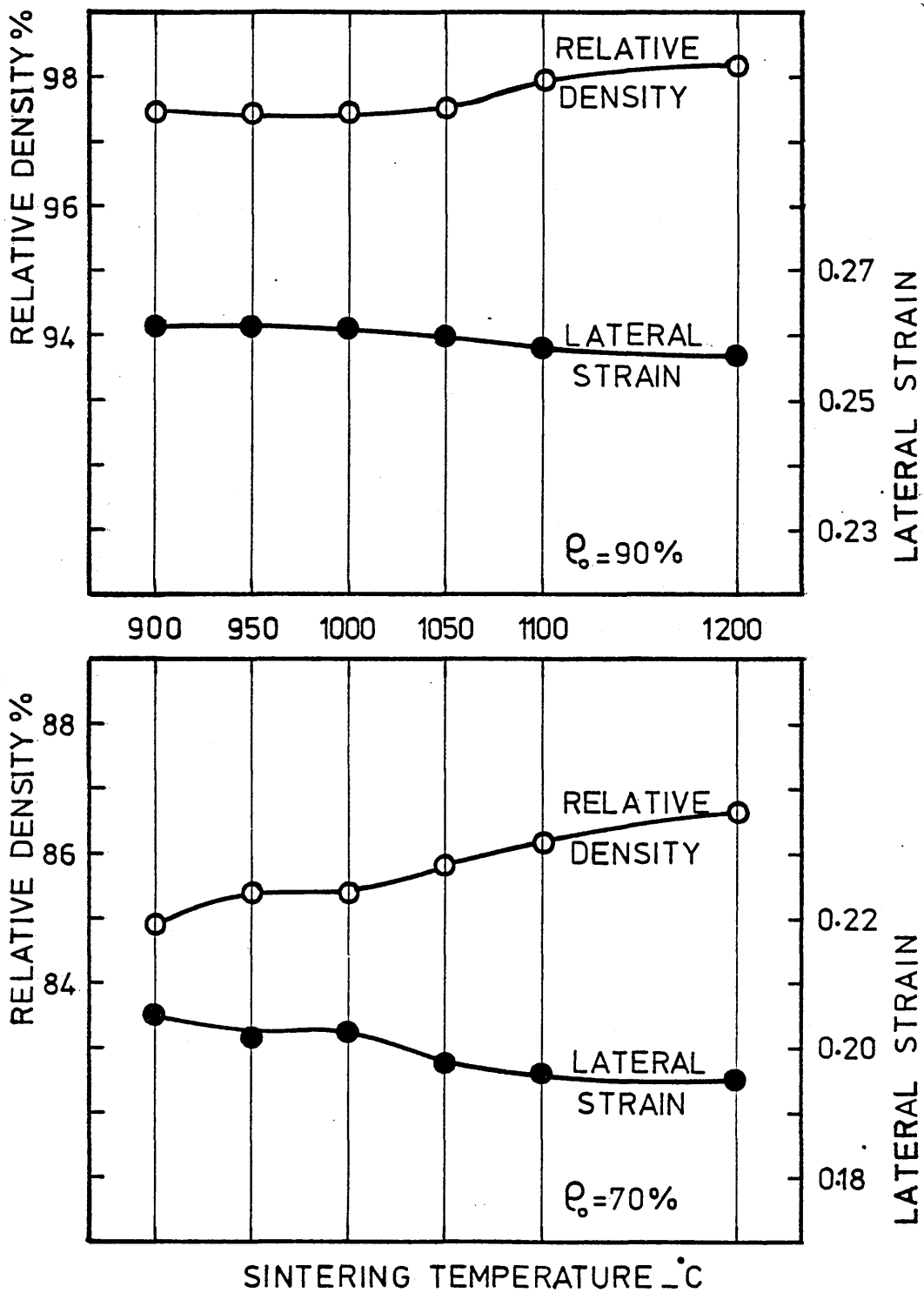


Fig (3.8) The effect of sintering temperature on the final density and the corresponding lateral strain of specimens of two initial densities upset to 0.6 true axial strain

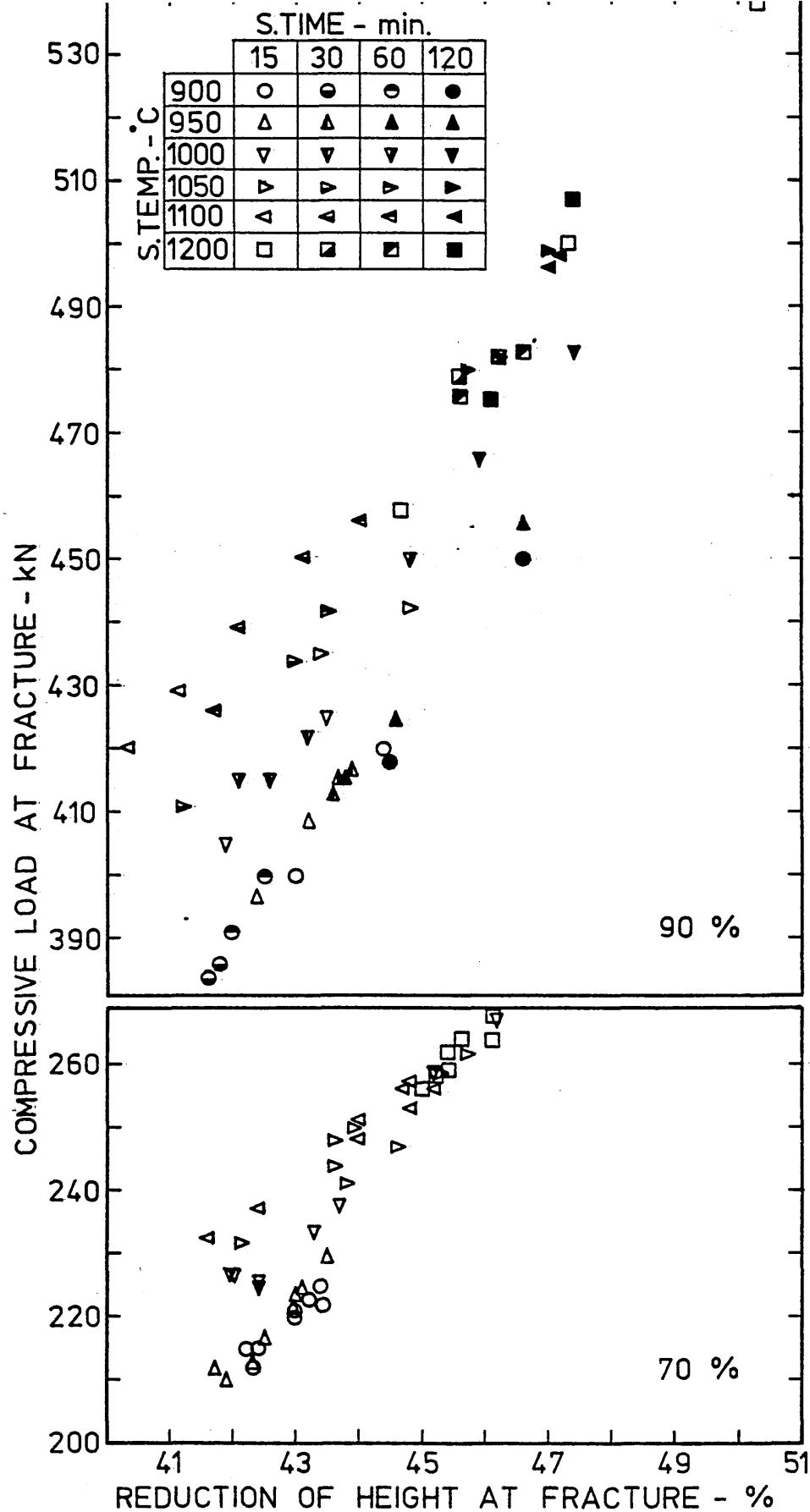


Fig (3.9) Compressive load-reduction of height relationship for specimens of two initial densities, compressed till fracture between flat dies without using a lubricant

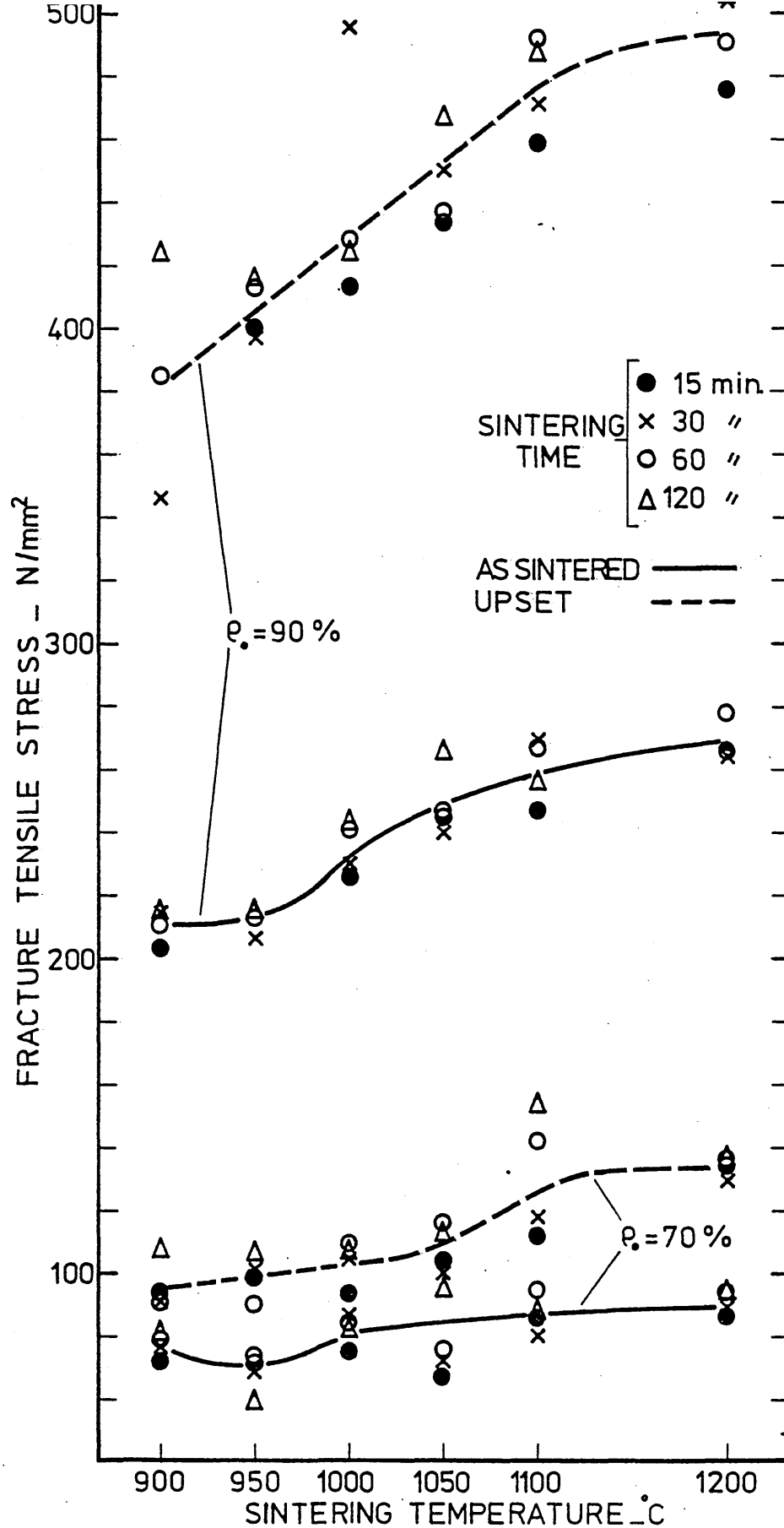


Fig (3.10) The effect of sintering time and temperature on the fracture Tensile stress of specimens of two initial densities before and after being upset to 0.6 true axial strain

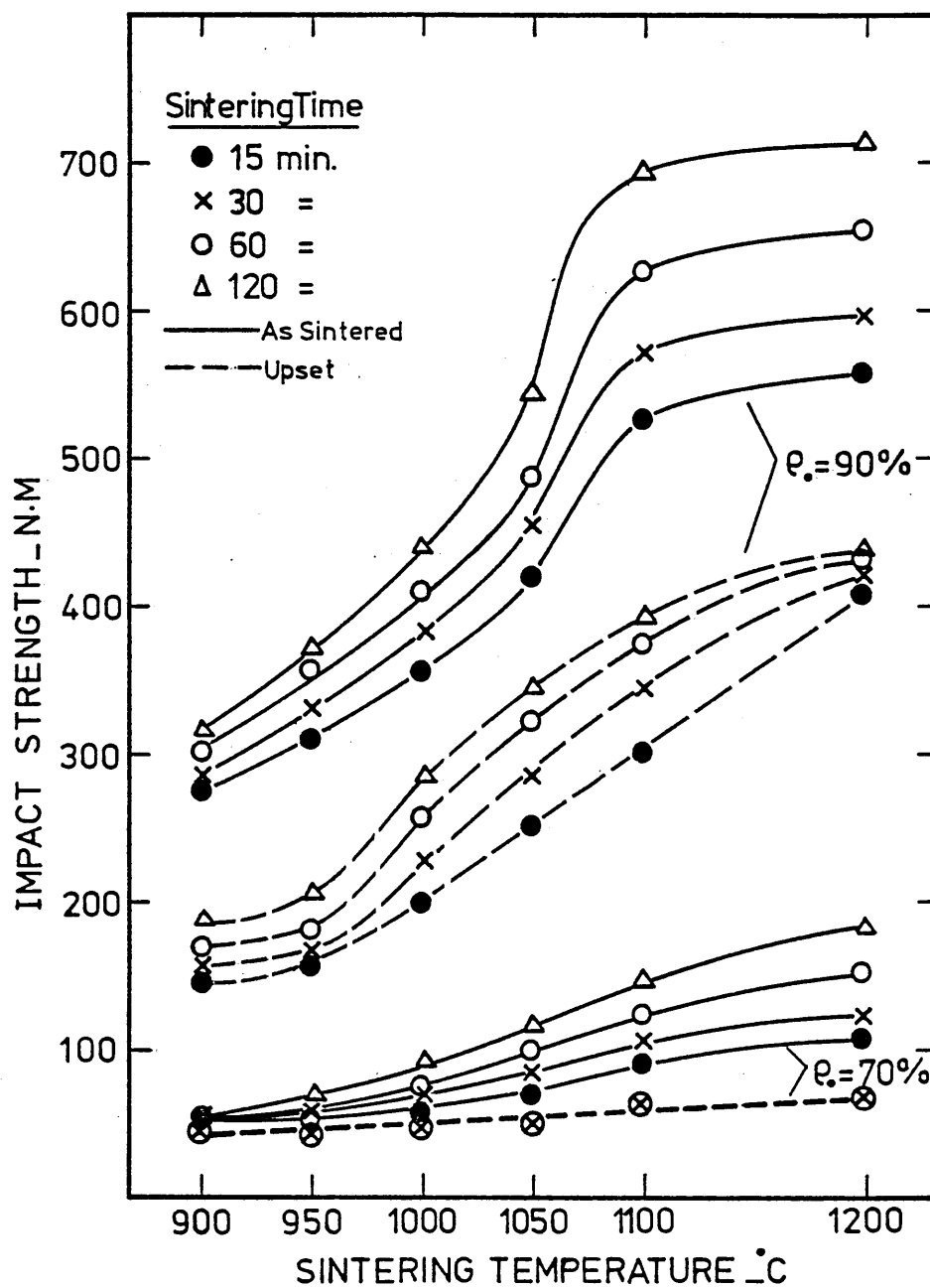


Fig (3.11) The effect of sintering time and temperature on the impact strength of specimens of two initial densities before and after being upset to 0.6 true axial strain

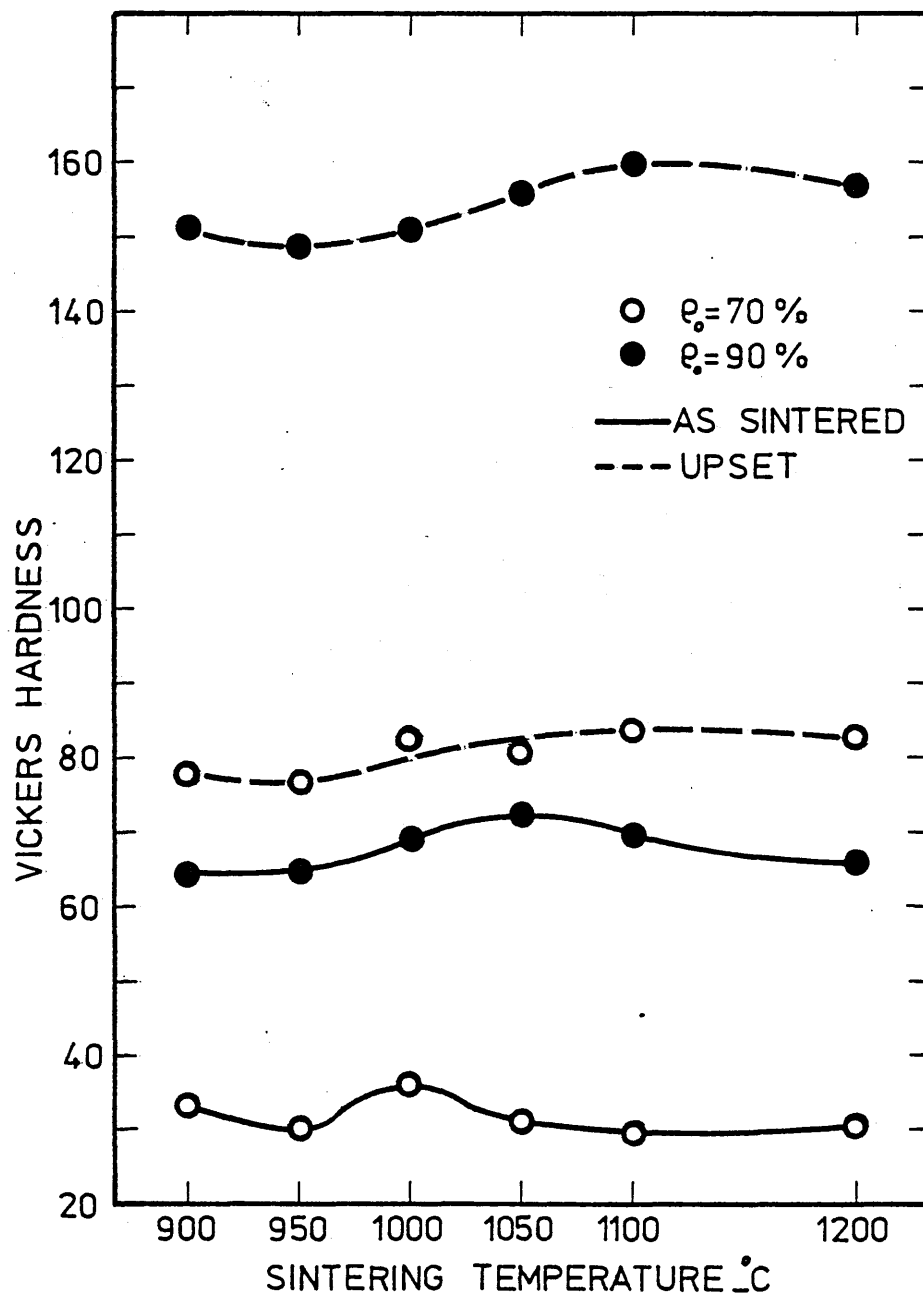


Fig (3.12) The effect of sintering time and temperature on the hardness of specimens of two initial densities before and after being upset to 0.6 true axial strain

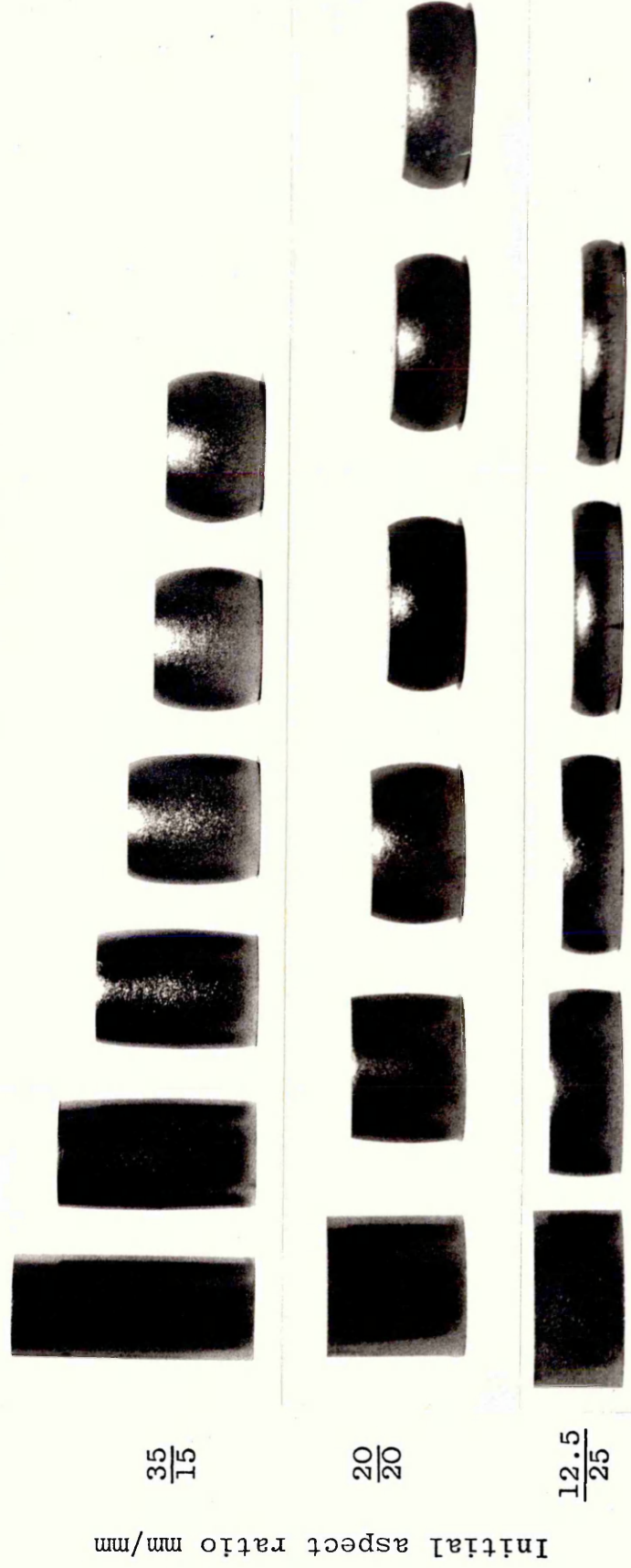


Fig (3.13) Specimens of various initial aspect ratio but of equal mass.

Incrementally upset without using a lubricant (scale 1:1)

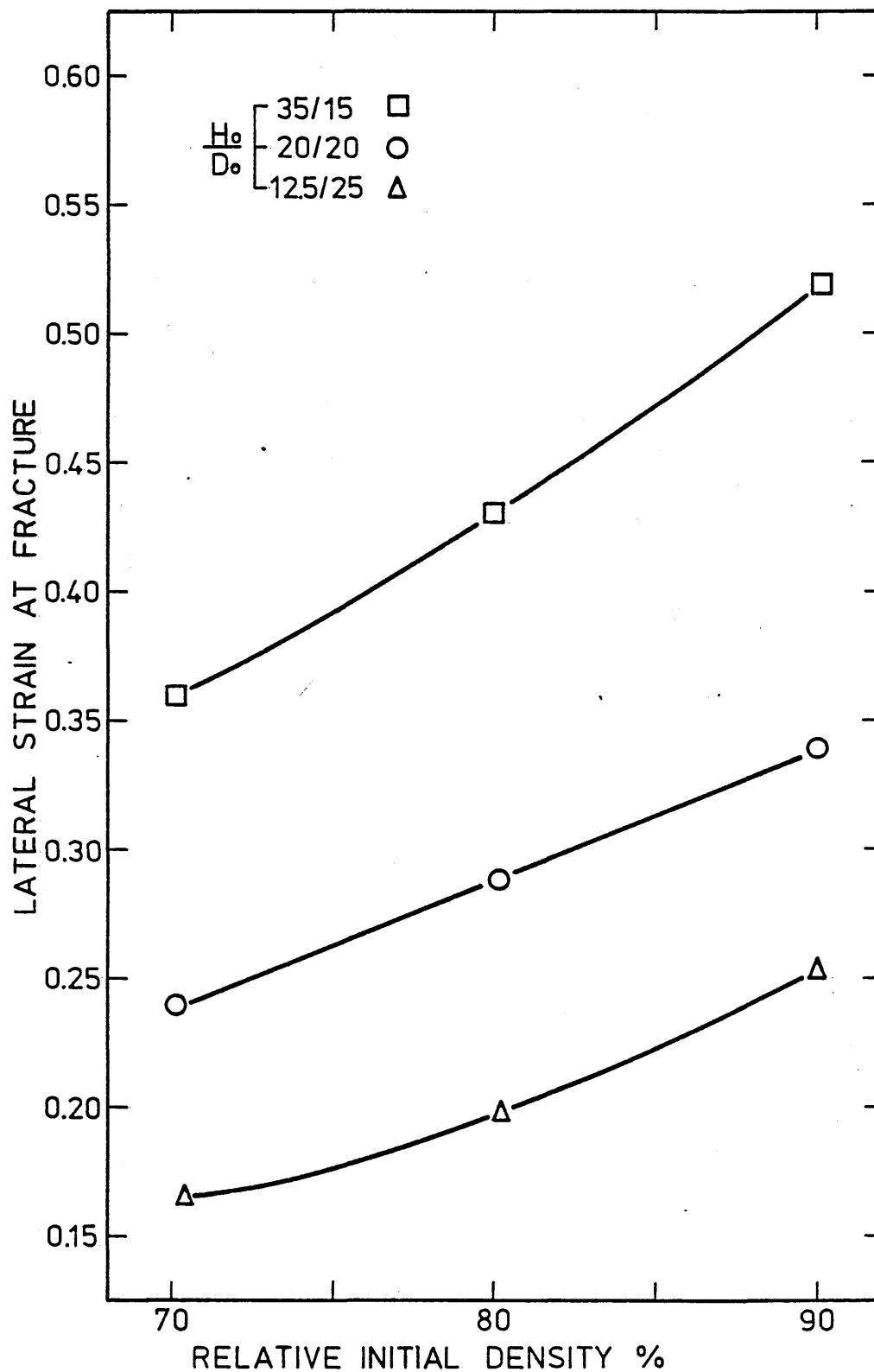


Fig (3.14a) The variation of lateral strain at fracture with the initial density of specimens of various initial aspect ratios but of equal mass

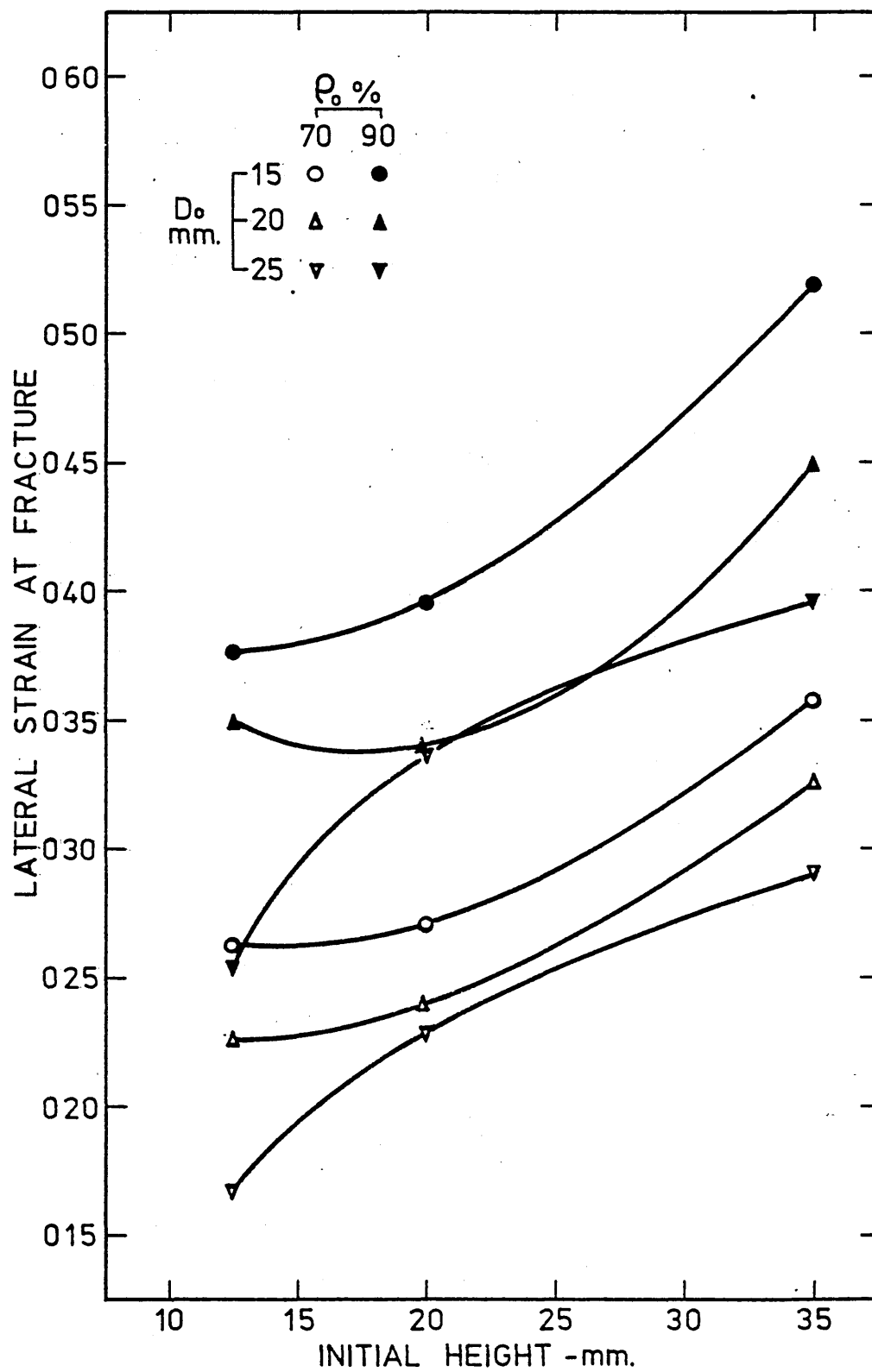


Fig. (3.14b) The variation of lateral strain at fracture with the initial height of specimens of two initial densities and three initial diameters (D_0)

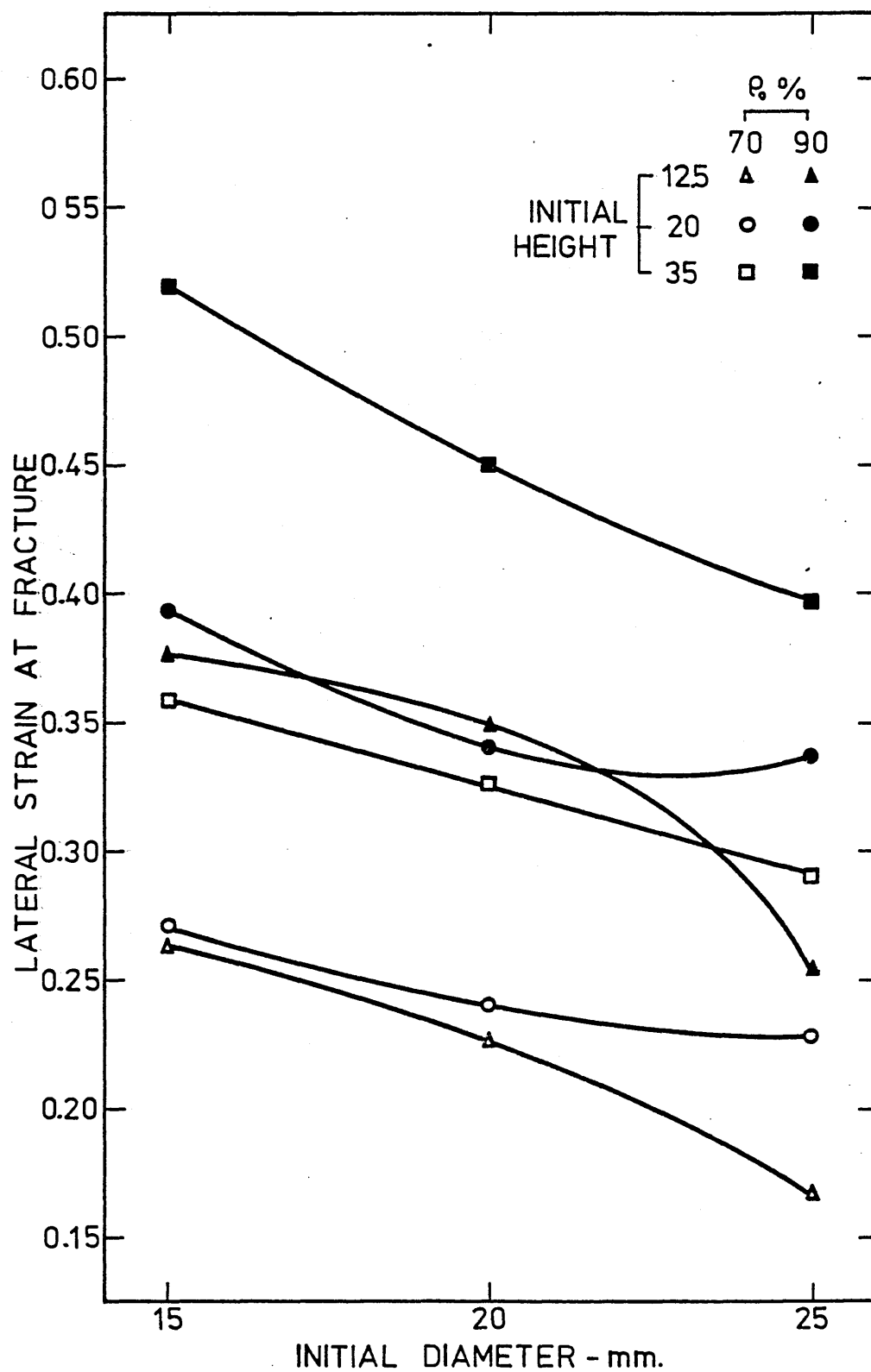


Fig (3.14c) The variation of lateral strain at fracture with the initial diameter of specimens of two initial densities and three initial heights

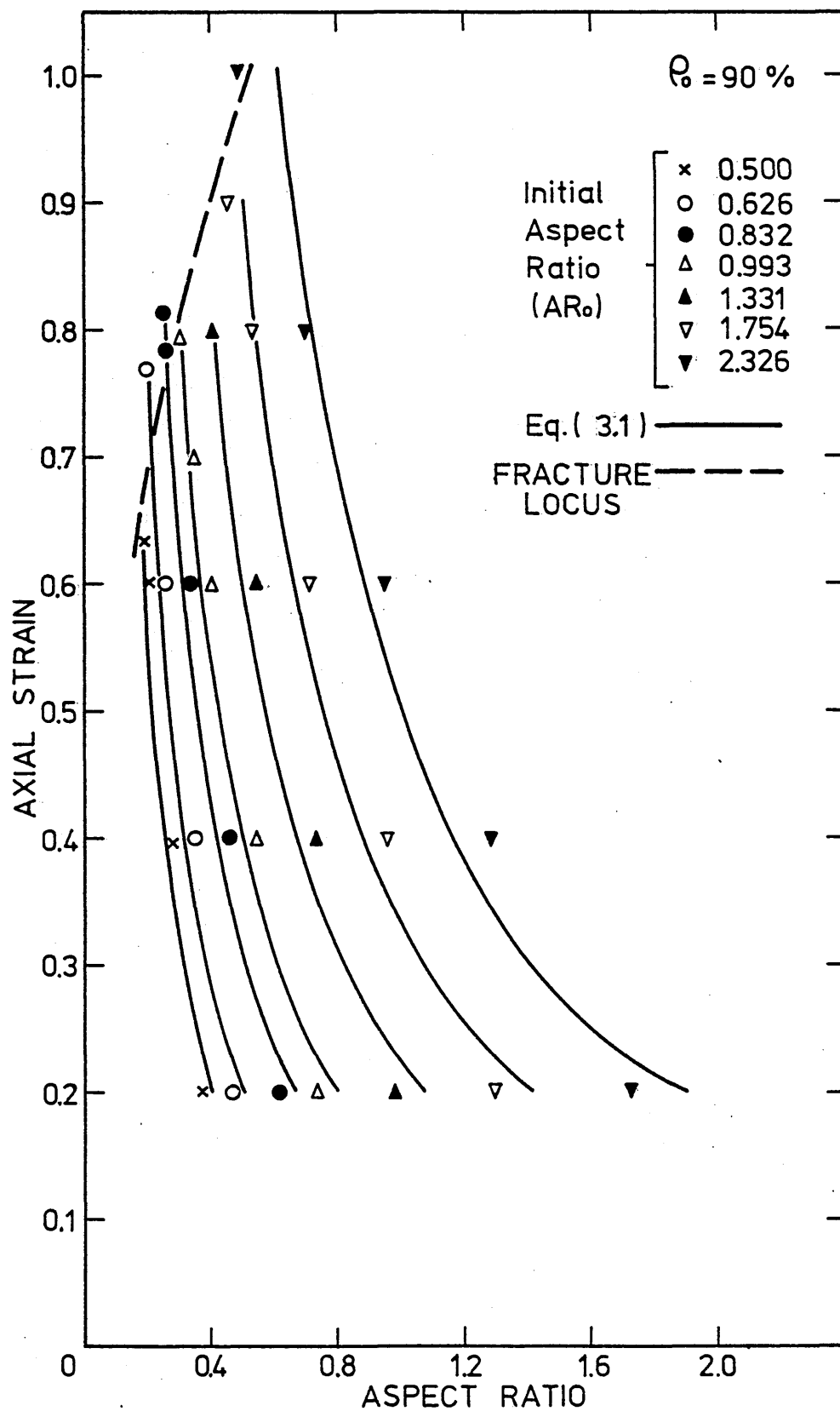


Fig (3.15a) The variation of axial strain with aspect ratio for specimens of 90% initial relative density and of various initial aspect ratios, upset with using a lubricant

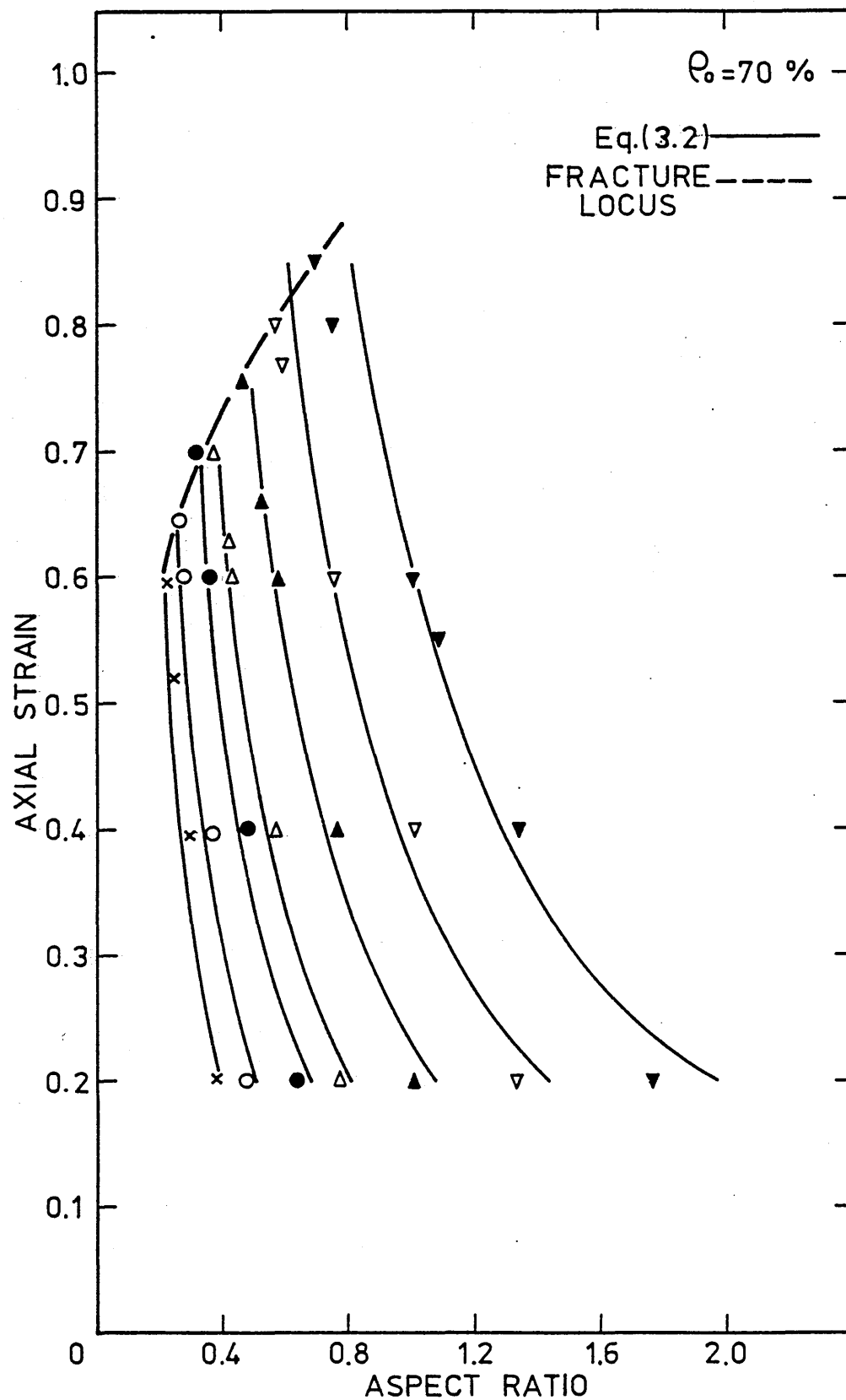


Fig (3.15b) The variation of axial strain with aspect ratio for specimens of 70% initial relative density and of various initial aspect ratios, upset with using a lubricant

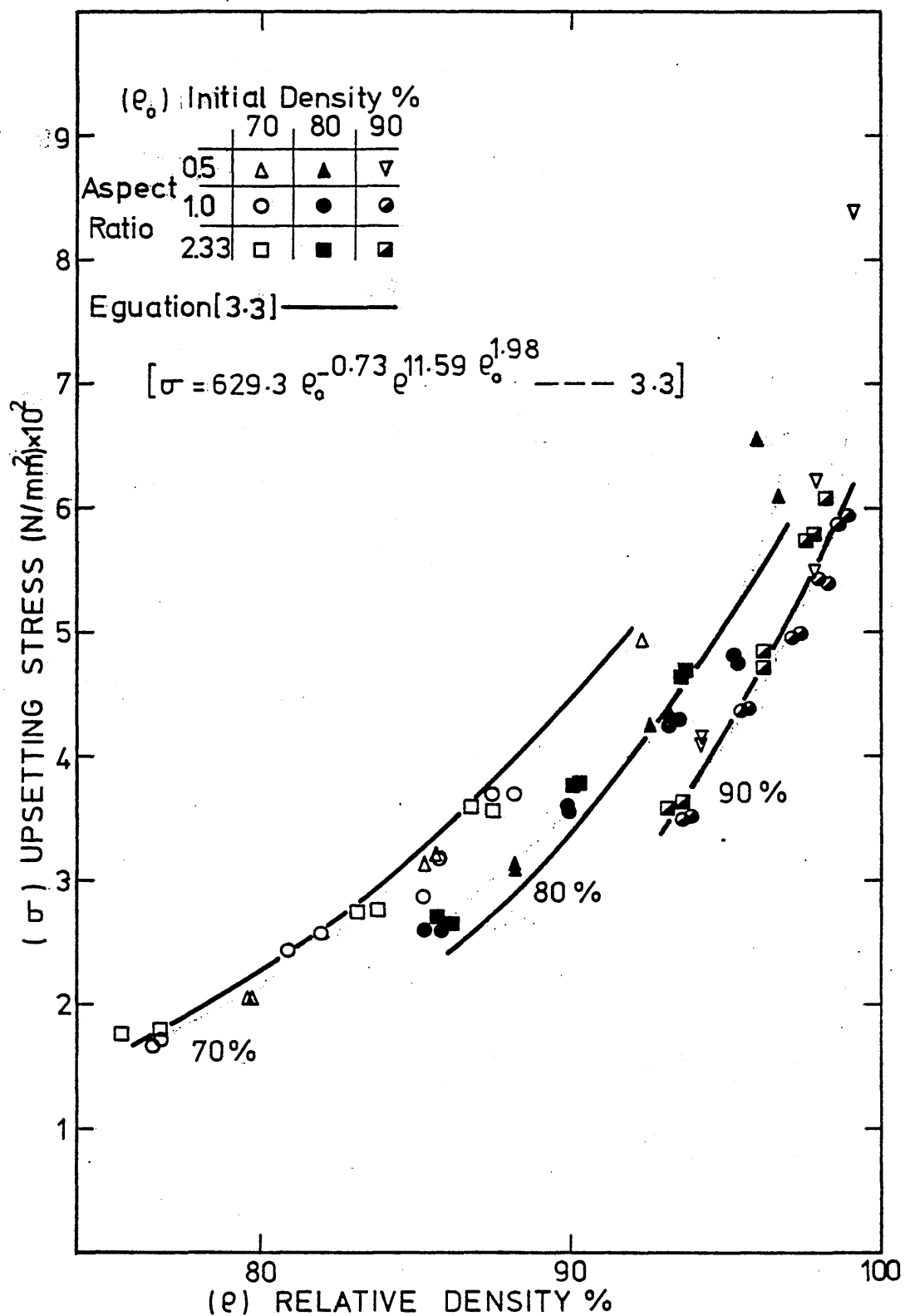


Fig (3.16) The variation of upsetting stress with the relative density of specimens of three initial densities and aspect ratios but of equal mass

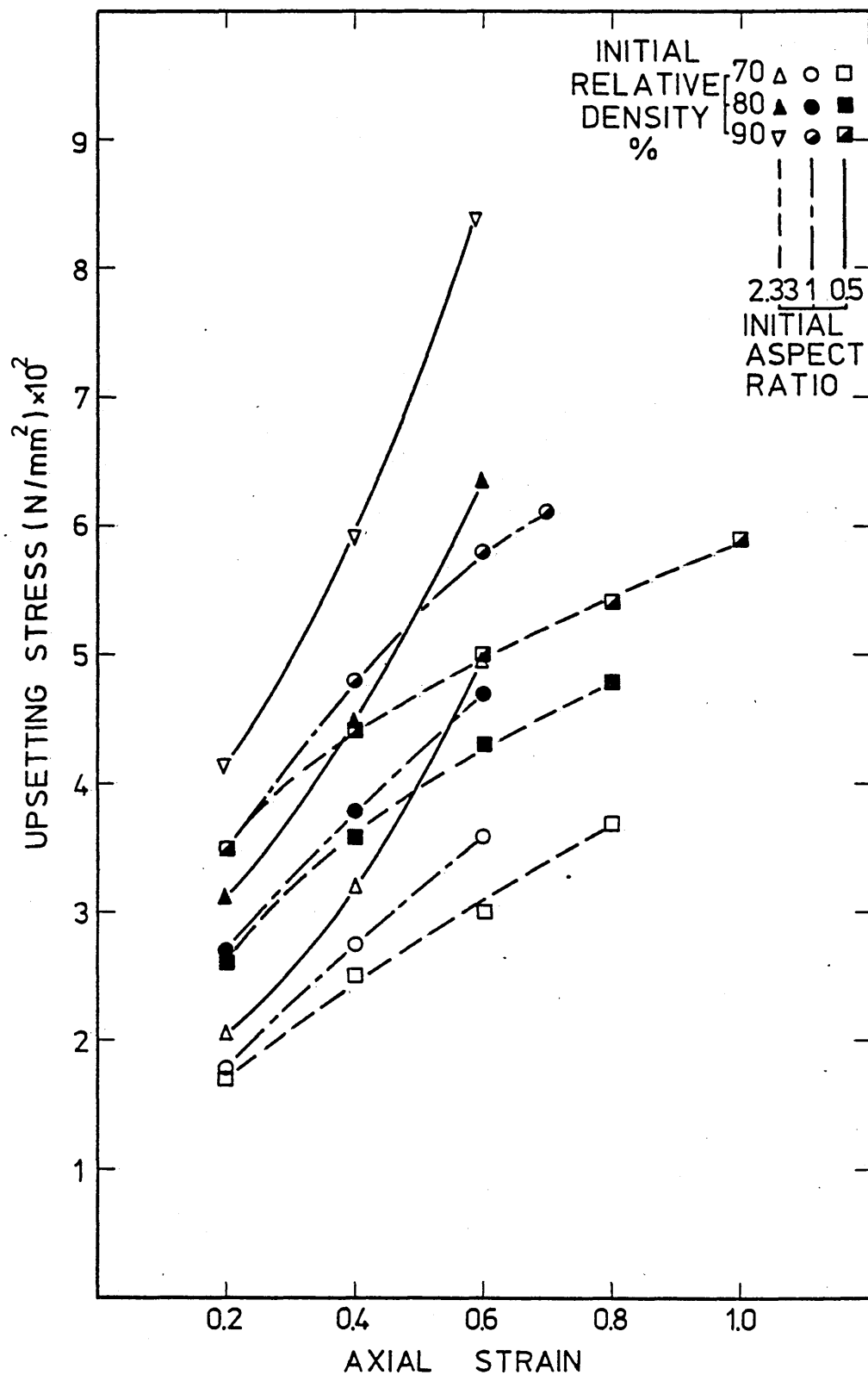


Fig (3.17) The stress-strain relationship for specimens of three initial densities and aspect ratios, but of equal mass, upset between polished flat dies

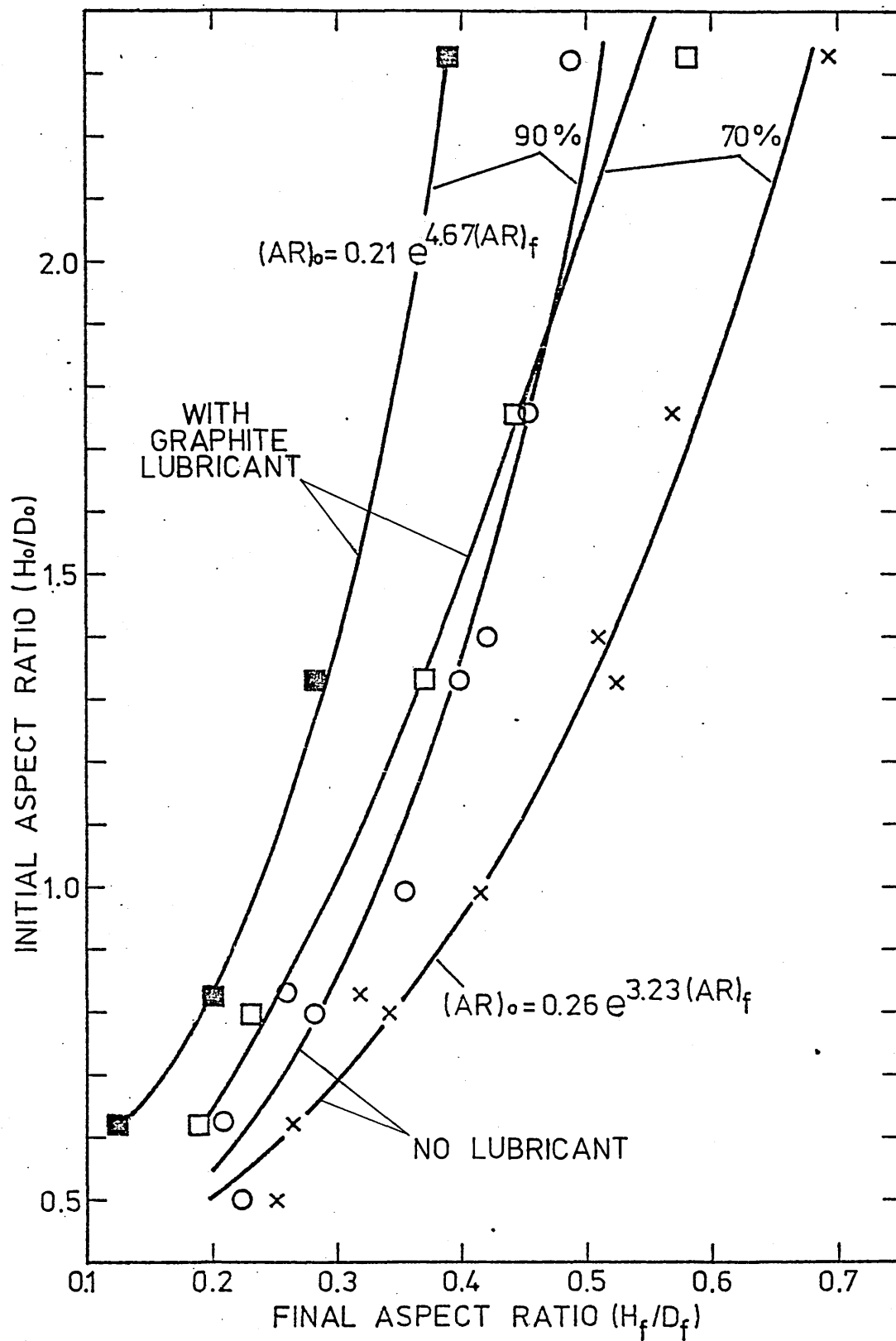


Fig (3.18) The variation of initial aspect ratio with final aspect ratio for specimens of two initial densities upset with and without using a lubricant

CHAPTER 4

FLOW AND FRACTURE OF MATERIAL OF VARYING GEOMETRY

4.1 Introduction

In general, during a forging process, the material flows into the direction of least resistance. This resistance may be caused by either internal or external factors: The internal resistance is determined by the properties of the material and the geometry of the forged component, ie, the shape of its cross-sectional area, presence of holes, hubs and flanges, inside and outside corners and height to width ratio. The external resistance is caused mainly by interface friction and die wall configuration and is affected by the applied pressure and temperature. Interface friction varies directly with contact area, therefore, free surfaces nearer to the axis of the forged component are expected to expand relatively easily compared with those at a distance. Hence, in the absence of symmetry, the analysis of the material flow becomes very complicated and this is one of the reasons why relevant studies in this field are mostly experimental.

By use of model studies various aspects of geometry and forging die configuration can be separated and investigated

independently in order to understand the effect of each variable involved.

In this study porous material billets of different cross-sections were upset under different die configurations in order to provide some basic information to the designer of sintered and forged components. This was followed by forging of a more specific component which involves rather different patterns of material flow. These patterns simulate the shape of a gear with two and four teeth and also with different widths of teeth. Gears are very basic components for machine tools and the gear teeth in particular must be tough and hard enough to withstand wear and various forces during their operation. Production of gear teeth by a well designed forging process results in material with properties which are superior to those found in teeth formed merely by machining. Porous materials deform under lower stress levels than wrought material, hence, they have a greater potential for cold forging if premature fracture can be avoided.

4.2 Present Work

The present work may be considered as general observations on various modes of deformation during upsetting of sintered iron specimens. These modes were obtained by either varying

the specimen cross-section or by varying the configurations of the upsetting die by introducing extrusion holes or recesses. Later on an attempt to establish a forgability limit by utilizing a closed die with a triangular cavity is reported. This is followed by studying in some detail the formation of a gear tooth.

4.2.1 Upsetting of Billets of Different Cross-Sections

As shown in Figure (4.1), blocks of various cross-sections were machined from cylindrical, sintered billets of 25 mm diameter x 25 mm height and of two initial relative densities, 70% and 90%. The surfaces of these billets were then mechanically inscribed with 2 mm x 2 mm square grids.

After preliminary upsetting tests, only four of these cross-sections were selected for further testing. The cross-sections retained were: square, rectangular, triangular and semi-circular. The excluded cross-sections fractured prematurely due to the presence of narrow edges and sharp corners in their features as shown in Figure (4.2).

The four selected cross-sections were quasistatically upset between smooth, overlapping, high-speed steel platens. The test was repeated using PTFE sheets as lubricant.

After every increment, each specimen was photographed from top and front. These photographs are shown in Figure (4.3), thus the strain on every square on the surface of these blocks was recorded and can be easily measured. Such results provide useful data for both practical applications and theoretical analysis of stresses and strains. The experimental results are shown in table (4.1)

In general, vertical cracks caused by hoop stresses were the cause of fracture, especially where surface curvature changes direction as illustrated by the sketch in Figure (4.4). The corners are pushed away without opening up, hence this change of curvature. Similar behaviour of wrought material was reported by Aku, et al (67).

4.2.2 Upset Extrusion

As mentioned in section 2.2.4, four platens with central holes of different entry radii were used for upset-extrusion tests. The hole diameters are 10 and 12 mm and the radii are 1, 2, 3 and 4 mm for every two platens, hence, the double side platens can produce a large number of die set combinations.

It was intended to test cylindrical specimens of two initial relative densities, 70 and 90%, and of 20 mm

diameter and of three different heights, 10, 20 and 30 mm. After testing with the smaller extrusion holes of the larger entry radii, it was observed that all the specimens fractured prematurely at the hub surface. Since the remaining die set combinations were likely to cause earlier fracture, therefore, it was decided to abandon this test programme at this stage.

This result indicates that porous materials cannot be easily extruded, especially with higher porosity contents, and changing the entry radii is not likely to improve the situation. As others have reported (71, 72) a draft angle of about 45° is essential to increase the density rapidly and to reduce the surface tension and hoop stresses. Larger entry radii should then improve material flow.

During extrusion into a die with a draft angle of 90° , new surfaces are being formed at a higher rate in comparison with the hub surface area, hence, the early fracture. Once an extruded head is formed, the critical stage is over. This has been shown by the author in reference (33) where he successfully extruded billets with a machined extrusion head. However, this point needs to be investigated further in order to see what would happen if the extrusion hole diameter is increased. Also the tapered

entry to the extrusion hole and the reduction in diameter needs to be investigated at various porosity levels.

4.2.3 Upsetting with Capped-Ends

As mentioned in section 2.2.4, two recessed platens were made for holding 20 mm diameter specimens during upsetting. These specimens were of three initial relative densities, 70, 80 and 90%, and three initial heights, 20, 25 and 30 mm. The depth of the recess was 4.5 mm. The results are shown in table (4.2).

This test was designed to study the formability of porous material with partial restraint as might be the case in some closed-die forging. Restraining the ends of a cylindrical specimen could also simulate the sticking interface friction condition. However, the material was successfully formed as shown in Figure (4.5). It can be seen that lateral strain, increased with the increase in initial relative density while the axial strain till fracture decreased due to the decrease of total densification.

A very interesting feature observed from this test was the improved formability of higher porosity specimens due to the reduction of free surface bulging which often leads to fracture. In other words, reducing the free surface by

use of recessed tools improves the formability of long billets. Therefore, the ratio of the specimen's free height to its total height is important. This importance may be further investigated by utilizing dies with through holes and using plug inserts of different heights in order to vary the height of the arrested part of the specimen.

4.2.4 Triangular-Cavity Closed Die Forging

Using the triangular cavity die shown in Figure (2.4) billets of 20 mm diameter, three different heights, 10, 20 and 30 mm and three initial relative densities, 70, 75 and 80% were forged at room temperature without using any lubricant. The results are shown in Table (4.3). In order to detect the onset of the fracture, the test had to be interrupted frequently.

It was intended to use this die as a measure of forgeability of sintered iron preforms over the full range of densities by measuring the extent of die filling until fracture.

However, full die filling without fracture could be achieved with the 80% initial relative density preforms.

Hence, preforms of higher initial relative densities were excluded from this test programme.

The extent of die filling is taken as a ratio between the height of the achieved triangle and the initial diameter of the preform, thus, as shown in Figure (4.6), better die filling was achieved with preforms of higher initial relative density but with a lower degree of straining.

In order that these results can be readily used by the designer of sintered components, Figure (4.7) has been drawn and fitted into an empirical equation by a computer based multiple regression analysis program. This equation is given by:

$$\epsilon_a = 0.651 \rho_o^{0.591} (AR_o)^{0.0534} \rho_o^{-2.216} \dots (4.1)$$

where ϵ_a = Axial strain

ρ_o = Initial relative density (range 70-80%)

AR_o = Initial aspect ratio

The final product at full density has a fixed mass and the initial density and aspect ratio can be varied in order to produce a good die filling with maximum work hardening. Hence, results corresponding to the same mass have been calculated and plotted on Figure (4.7) in order to show the sharp increase in axial strain associated with lower initial density and higher initial aspect ratio.

4.2.5 Closed Die Forging of Cylindrical Preforms into Cavities of Various Widths

The multi-cavity die set described in section 2.2.4 was used to investigate the extent of cavity filling at fracture. The specimens tested had three initial relative densities, 70, 80 and 90%, one initial diameter, 20 mm, and three initial heights, 10, 20 and 30 mm. Before the start of every test, all die surfaces in contact with the specimen were lubricated with a die lubricant (Tallow).

The compressive load was applied by a Denison press to a pre-determined level. After ejection the forged specimen was inspected for any cracks and measured for reduction of height and lateral spread. Then, the test was repeated on a second specimen with the load adjusted according to the cracks observed on the first specimen. Hence, the approximate fracture conditions were recorded in these tests and the results are given in Table 4.4. These results give an idea of the severity of fracture when it occurred. It is also evident that the level of load was affected by the degree of lubrication and the extruded backflash, especially with specimens of higher initial density and at higher loads. After each test, all die surfaces which came in contact with the forged specimen

were cleaned and hand polished before being relubricated.

In order to evaluate the material flow into a cavity, the ratio between the depth of the formed tooth to its width was considered as a measure. In general, the material exhibited a good degree of filling under moderate loads. Each of the variables considered had a different effect upon the extent of cavity filling. These effects are more or less similar to those observed in upsetting.

The effect of increasing the specimen height is shown in Figure 4.8, where better cavity filling was obtained with longer specimens. This effect may be presented in the form of a relationship between the initial and final aspect ratios. This information might be more useful to the designer of sintered components, since it sums up the dimensional relationship of the forged component (see section 3.3). Figure 4.9 shows the relationship between the initial and final aspect ratios which follows the same trend as that shown in Figure 3.18 for simple upsetting. In fact, the results for the 70% initial relative density and 8 mm cavity coincides with that for the corresponding billet in unlubricated simple upsetting. Therefore, it should be useful to fit the relationship between the initial aspect ratio and the final aspect ratio into an

empirical relationship by the multiple regression analysis in the form of:

$$AR_f = T (AR_o)^V \dots\dots\dots (4.2)$$

where (AR_o) and $(AR)_f$ are the initial and final aspect ratios respectively.

T and V are constants and their values for the various initial conditions are given in table (4.5).

The decrease in cavity width also contributed towards improving cavity filling, especially for the single tooth cavity where the decrease was more significant as shown in Figure (4.10). With the narrower cavity, the material is forced to densify at a higher rate, thus avoiding premature fracture. The effect of initial density is shown in Figure 4.11 where better filling is obtained with higher initial density.

To sum up the effects of all the variables involved in this test in one nomogram, the ratio between the depth of the formed tooth to its width was plotted against the ratio of its initial height to the initial width. This nomogram is shown in Figure (4.12).

TABLE 4.1

Incremental upsetting of rismatic locks	PTFE Lubricant				No Lubricant			
	Specimen 1		Specimen 2		Specimen 1		Specimen 2	
	Height mm	Load kN	Height mm	Load kN	Height mm	Load kN	Height mm	Load kN
Rectangular 2.4 x 11.2 mm	20.41	50.2	20.45	50.4	20.43	49.6	20.48	49.5
	16.76	82.5	16.71	82.5	16.77	80	16.77	82
	13.71	123.5	-	-	13.73	116.5	13.69	120
	11.21	173	-	-	-	-	11.25	165
	9.2	238	-	-	-	-	-	-
Square 7.58 x 17.58 mm	20.48	57.8	20.49	57.1	20.49	64	20.47	64.3
	16.77	96.5	16.75	95.5	17.76	94	16.75	107.5
	-	-	13.71	142	13.71	158.6	13.71	158.5
	-	-	11.25	199	11.67	211	12.05	200
Triangular	20.41	41.1	20.41	39.8	20.5	47	20.46	44.3
	16.75	66.5	16.77	64	16.77	75	16.73	70
	13.73	98.5	13.72	93.2	13.72	107.33	13.69	101.6
	11.25	135	-	-	11.24	145	11.23	139
Semi-circular = 12.5 mm	20.4	48.1	20.32	47	20.46	49.3	20.47	47
	16.67	79	16.63	78	16.75	83.1	16.74	79.7
	13.67	114.5	13.61	112.5	13.72	122	13.73	117.7
	-	-	11.15	152	11.69	160	11.25	167
Circular with concave cut	20.59	64.6	20.55	65	20.49	59	-	-
	16.73	109.6	16.83	108	17.69	91.7	-	-
	-	-	13.76	162.5	13.65	161	-	-
	-	-	11.25	231	11.22	229	-	-
	-	-	9.26	314	-	-	-	-
Circular with right angle cut	20.49	55	20.49	56	-	-	-	-
	16.76	89.3	16.77	91	-	-	-	-
	13.78	124	13.73	127.5	-	-	-	-
Circular with square cut	20.5	69	-	-	-	-	-	-
	16.78	107	-	-	-	-	-	-
Initial Height = 25 mm, Initial Relative Density = 70 %								

TABLE 4.2 Upsetting with capped ends

INITIAL CONDITIONS		No of Specimen	EXPERIMENTAL MEASUREMENTS			CALCULATED STRAINS	
Relative Density	Height mm		Load kN	Height mm	Diameter mm	Axial -ev *	Lateral **
70%	20	1	249	13.03	24.38	0.931	0.203
		2	251	13.02	24.38	0.933	0.203
		3	240	13.09	24.29	0.918	0.199
	25	1	191	16.20	24.72	0.761	0.215
		2	197	16.26	24.79	0.779	0.218
		3	187	16.28	24.62	0.751	0.211
	30	1	196	18.18	25.78	0.798	0.259
		2	191	18.33	25.61	0.782	0.252
		3	197	18.13	25.77	0.801	0.258
80%	20	1	283	13.92	24.86	0.752	0.222
		2	285	13.93	24.78	0.750	0.219
		3	284	13.96	24.77	0.745	0.218
	25	1	274	16.42	25.83	0.734	0.260
		2	253	16.74	25.48	0.694	0.246
		3	288	16.21	26.16	0.760	0.273
	30	1	260	18.80	26.54	0.736	0.287
		2	274	18.60	26.80	0.756	0.297
		3	268	18.69	26.70	0.746	0.293
90%	20	1	324	14.86	25.31	0.592	0.238
		2	326	14.87	25.28	0.590	0.237
		3	340	14.66	25.49	0.609	0.245
	25	1	330	17.00	26.78	0.662	0.294
		2	320	17.24	26.42	0.634	0.281
		3	312	17.40	26.18	0.617	0.272
	30	1	334	19.14	27.78	0.704	0.331
		2	352	18.78	28.19	0.738	0.346
		3	363	18.59	28.37	0.756	0.352
* Axial Strain = $\ln \left(\frac{\text{initial height} - \text{recessed height}}{\text{final height} - \text{recessed height}} \right)$							
** Lateral Strain = $\ln (\text{final diameter}/\text{initial diameter})$							

TABLE 4.3 Triangular cavity closed die forging


INITIAL CONDITIONS		No of Specimen	EXPERIMENTAL RESULTS				
Relative Density	Height mm		Load kN	Height mm		Relative Density %	Axial Strain
70%	10	1	500	5.14	23.85	-	0.666
		2	600	4.67	25.45	97.68	0.761
		3	540	4.78	25.05	97.42	0.738
	20	1	400	10.04	24.63	-	0.689
		2	500	8.96	26.13	98.17	0.803
		3	570	8.87	26.52	98.64	0.813
	30	1	550	13.75	25.96	-	0.780
		2	600	12.95	27.26	98.58	0.840
		3	600	12.99	27.13	98.00	0.837
75%	10	1	800	4.74	26.73	99.33	0.747
		2	740	4.85	26.05	97.73	0.724
		3	740	4.87	25.90	97.73	0.719
	20	1	400	10.41	24.82	96.63	0.653
		2	400	10.42	24.78	96.83	0.652
		3	770	9.29	27.36	99.19	0.767
	30	1	600	14.98	25.86	-	0.694
		2	800	13.41	28.20	99.51	0.805
		3	800	13.39	28.19	99.65	0.807
80%	10	1	700	5.45	24.83	99.07	0.607
		2	800	5.10	26.21	99.51	0.673
		3	900	5.01	26.65	99.55	0.691
	20	1	700	9.90	27.13	98.96	0.703
		2	800	9.75	27.62	99.13	0.718
		3	930	9.51	28.02	99.13	0.743
	30	1	700	14.46	27.77	99.09	0.730
		2	900	14.17	28.44	99.44	0.750
		3	1000	14.08	28.53	99.50	0.756

TABLE 4.4a Multi-cavity closed die forging

INITIAL CONDITIONS				EXPERIMENTAL READINGS AND OBSERVATIONS					
Cavity Width	Density and diameter	Height mm	Spec No	Load kN	Height mm	Maximum Diameter mm	Tooth Width mm	Tooth Dep/Wid Ratio	Cracks Obser
3 mm	70% 19.9 mm	10	1	400	6.42	-	-	-	NF
			2	450	6.25	25.37	3.01	0.88	F-
		20	1	300	13.04	-	-	-	NF
	80% 19.93 mm		2	400	12.38	25.68	3.01	0.928	F-
		30	1	400	18.68	-	-	-	NF
			2	460	18.15	26.61	3.01	1.078	F
	80% 19.93 mm	10	1	500	6.90	-	-	-	NF
			2	560	6.77	27.33	3.02	1.202	F-
		20	1	500	13.68	-	-	-	NF
	90% 19.96 mm		2	560	13.38	27.96	3.02	1.302	F-
		30	1	500	20.23	-	-	-	NF
			2	600	19.36	30.21	3.02	1.66	F-
	90% 19.96 mm	10	1	600	7.52	27.84	3.03	-	F-
			2	700	7.21	30.28	3.03	1.684	F-
		20	1	600	14.59	29.87	3.03	-	F-
3.5 mm	70% 19.9 mm		2	700	13.38	33.96	3.03	2.275	F-
		30	1	600	21.98	29.46	3.03	-	F-
			2	700	20.92	32.82	3.03	2.075	F-
	70% 19.9 mm	10	1	400	6.34	24.85	3.55	0.668	F-
			2	450	6.18	25.57	-	-	F-
		20	1	350	12.80	24.68	3.56	-	F-
	80% 19.93 mm		2	400	12.38	25.64	-	0.777	F-
		30	1	400	18.73	25.30	3.57	-	F-
			2	460	17.91	27.13	-	0.982	F-
	80% 19.93 mm	10	1	500	6.78	26.88	3.56	-	F-
			2	560	6.64	27.67	-	1.06	F-
		20	1	500	13.38	27.91	3.57	-	F-
	90% 19.96 mm		2	560	12.92	29.59	-	1.323	F-
		30	1	500	19.89	28.28	3.59	-	F-
			2	600	18.64	31.68	-	1.605	F-
	90% 19.96 mm	10	1	600	7.38	-	-	-	NF
			2	700	7.07	30.77	3.57	1.49	F-
		20	1	600	14.23	-	-	-	NF
	90% 19.96 mm		2	700	13.90	32.80	3.59	1.76	F-
		30	1	600	20.87	-	-	-	NF
			2	700	19.78	35.16	3.61	2.078	F-

NF: Not fractured,

F-, F, F+ are Fractured with small, medium and large cracks simultaneously

TABLE 4.4b Multi-cavity closed die forging

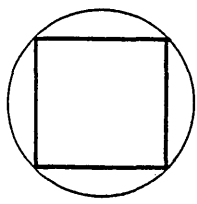
INITIAL CONDITIONS				EXPERIMENTAL READINGS AND OBSERVATIONS					
Cavity Width	Density and Diameter	Height mm	Spec No	Load kN	Height mm	Maximum Diameter mm	Tooth Width mm	Tooth Dep/Wid Ratio	Cracks Obser
4 mm	70% 19.9 mm	10	1 2	400 450	6.26 6.11	25.10 25.91	4.00 4.00	0.626 -	F- F
		20	1 2	400 430	12.20 12.00	26.12 26.62	4.00 4.00	- 0.814	NF NF
		30	1 2	400 460	18.28 17.54	- 27.74	4.01 4.01	- 0.950	NF F-
	80% 19.93 mm	10	1 2	500 560	6.69 6.46	- 28.91	4.00 4.00	- 1.1	NF F-
		20	1 2	500 560	13.04 12.54	- 30.52	4.01 4.01	- 1.294	NF F-
		30	1 2	500 600	19.30 17.74	- 33.41	4.03 4.03	- 1.644	NF F-
	90% 19.96 mm	10	1 2	600 700	7.07 6.84	- 31.59	4.01 4.01	- 1.428	NF F-
		20	1 2	600 700	13.71 12.84	- 35.12	4.03 4.03	- 1.855	NF F-
		30	1 2	600 700	19.51 19.03	- 36.01	4.05 4.05	- 1.957	NF F-
8 mm	70% 19.9 mm	10	1 2	400 400	6.12 5.99	27.24 28.11	8.19 8.19	0.448 0.501	F- F-
		20	1 2	350 330	11.97 12.07	28.60 28.08	8.20 8.20	0.53 0.499	F NF
		30	1 2	400 370	16.89 17.07	31.48 30.76	8.22 8.22	0.704 0.661	F+ F
	80% 19.93 mm	10	1 2	500 510	6.41 6.34	30.56 30.16	8.21 8.21	0.647 0.684	F- F-
		20	1 2	500 530	12.34 11.75	32.76 35.11	8.24 8.24	0.779 0.921	NF F-
		30	1 2	500 530	17.40 16.58	35.98 38.34	8.28 8.28	0.969 1.112	NF NF
	90% 19.96 mm	10	1 2	600 650	6.68 6.41	34.14 36.62	8.24 8.24	0.860 1.011	NF NF
		20	1 2	600 750	12.13 11.83	39.42 40.06	8.29 8.29	1.174 1.212	NF NF
		30	1 2	600 580	17.99 18.00	40.03 39.93	8.30 8.30	1.209 1.203	NF NF

TABLE 4.4c Multi-cavity closed die forging

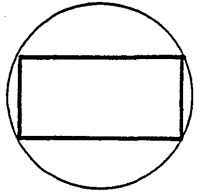
INITIAL CONDITIONS			EXPERIMENTAL READINGS AND OBSERVATIONS						
	Density and Diameter	Height mm	Spec No	Load kN	Height mm	Maximum Diameter mm	Tooth Width mm	Tooth Dep/Wid Ratio	Cracks Obser
10 mm	70% 19.9 mm	10	1 2	400 390	5.80 5.83	28.08 27.99	10.17 10.17	0.402 0.398	F NF
		20	1 2	400 340	10.57 11.13	32.36 29.97	10.18 10.18	0.612 0.495	F+ F-
		30	1 2	400 370	15.30 15.27	33.60 33.25	10.21 10.21	0.671 0.654	F+ F
	80% 19.93 mm	10	1 2	500 520	6.09 6.01	30.92 31.56	10.19 10.19	0.539 0.571	NF F-
		20	1 2	500 530	10.95 10.85	35.58 35.98	10.22 10.22	0.766 0.766	NF NF
		30	1 2	500 540	15.97 15.05	37.07 39.75	10.25 10.25	0.836 0.857	NF F-
	90% 19.96 mm	10	1 2	600 700	6.16 5.75	35.25 38.48	10.22 10.22	0.748 0.906	NF F-
		20	1 2	600 700	11.59 11.03	38.03 40.06	10.25 10.25	0.881 0.980	NF NF
		30	1 2	600 550	16.62 16.79	40.03 40.01	10.25 10.25	0.979 0.978	NF NF
12 mm	70% 19.9 mm	10	1 2	400 390	5.52 5.41	28.74 29.32	12.21 12.21	0.362 0.386	F F-
		20	1 2	350 340	10.04 10.42	32.47 31.13	12.21 12.21	0.515 0.467	F F-
		30	1 2	400 370	13.97 14.56	35.43 33.90	12.22 12.22	0.635 0.573	F+ F
	80% 19.93 mm	10	1 2	500 530	5.81 5.66	30.99 32	12.24 12.24	0.452 0.493	NF F-
		20	1 2	500 510	10.40 10.30	35.45 35.74	12.25 12.25	0.633 0.645	F F
		30	1 2	500 530	14.60 14.25	38.24 39.32	12.27 12.27	0.746 0.790	F- F-
	90% 19.96 mm	10	1 2	600 680	5.90 5.57	34.53 37.07	12.26 12.26	0.594 0.698	F- F
		20	1 2	600 700	10.43 10.29	39.71 40.06	12.27 12.27	0.805 0.819	NF NF
		30	1 2	600 550	15.57 15.64	40.02 40.01	12.28 12.28	0.817 0.846	NF NF

TABLE 4.5

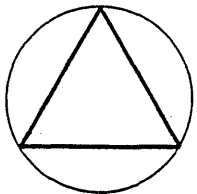
TESTPIECE		EQUATION CONSTANTS		
Tooth Width	Initial Relative Density	Multiplier	Index	Coeff of Determ
8 mm	70%	1.535	0.311	1.000
	80%	1.409	0.207	0.996
	90%	0.310	0.850	0.992
10 mm	70%	0.352	0.733	0.998
	80%	0.296	0.632	0.998
	90%	0.282	0.935	0.998
12 mm	70%	0.322	0.775	0.993
	80%	0.281	0.657	0.997
	90%	0.268	0.862	0.994



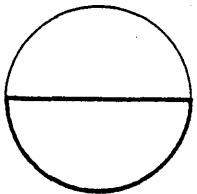
SQUARE



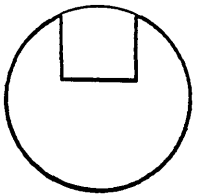
RECTANGLE



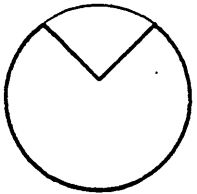
TRIANGLE



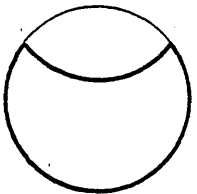
SEMI-CIRCLE



CIRCLE WITH SQUARE CUT



CIRCLE WITH VEE CUT

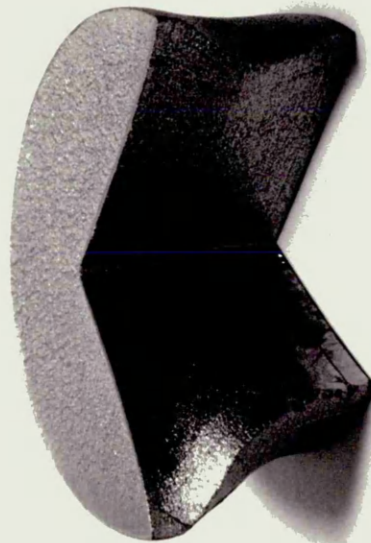


CIRCLE WITH CONCAVE CUT

Fig (4.1) Blocks of various cross sections (top view).
They were machined from sintered billets of 25 mm in
diameter and 25.2 mm in height to a finished height
of 25 mm (Scale 1:1)



Square cut



V cut



Concave cut

Fig (4.2) Fractured and buckled specimens of various cross-sections
upset with PTFE sheets as lubricant

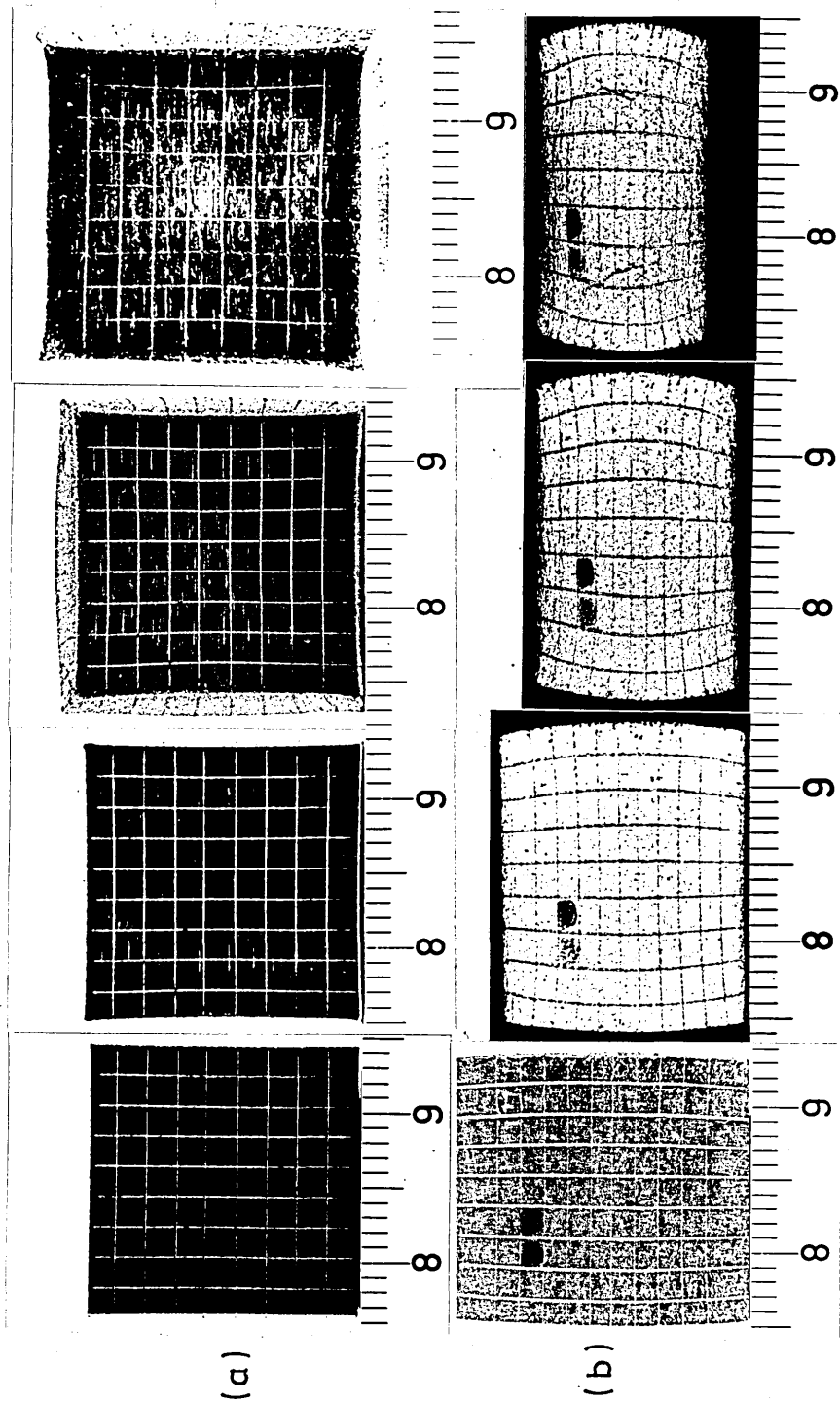


Fig (4.3a) Profile in progress for (a) top view and (b) side view of a specimen of square cross section upset without using a lubricant (scale in cm)

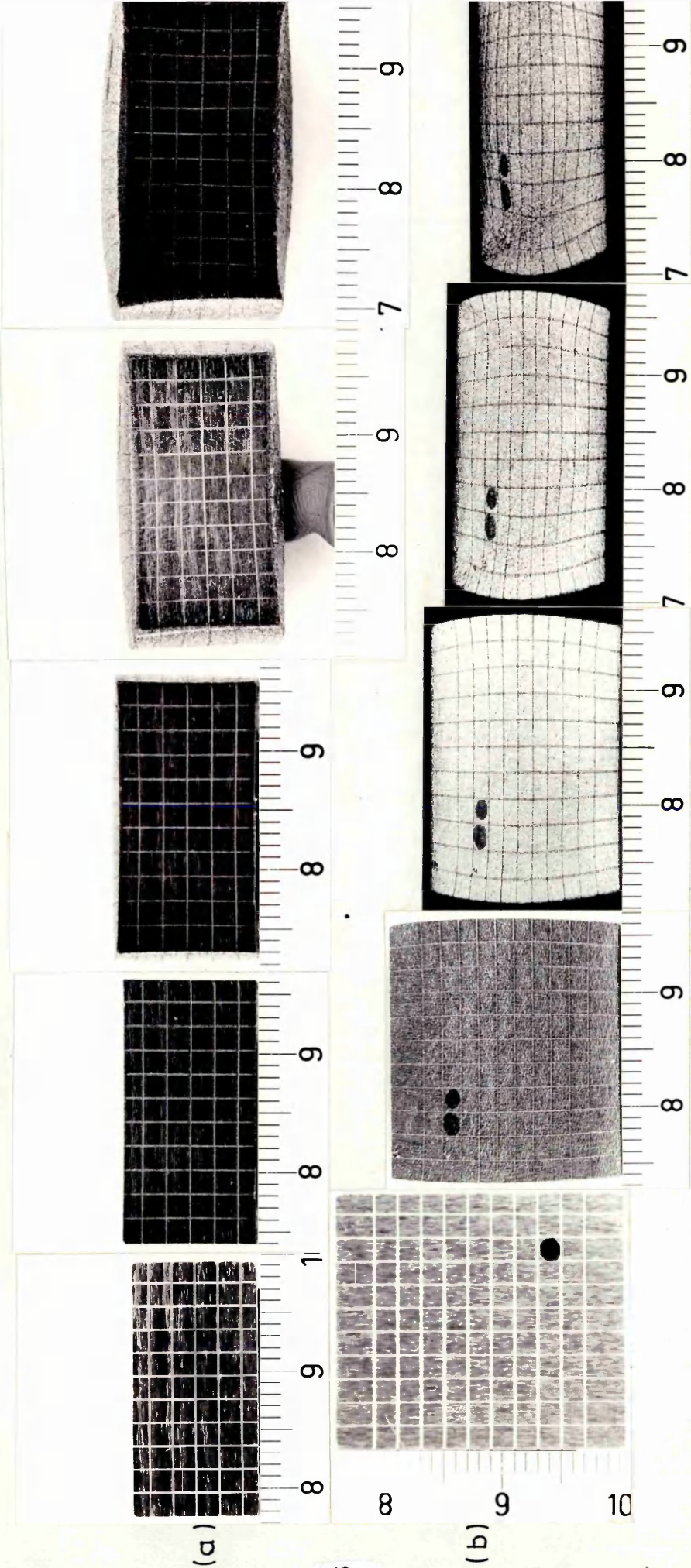


Fig (4.3b) Profile in progress for (a) top view and (b) side view of a specimen of a rectangular cross section upset without using a lubricant (scale in cm)

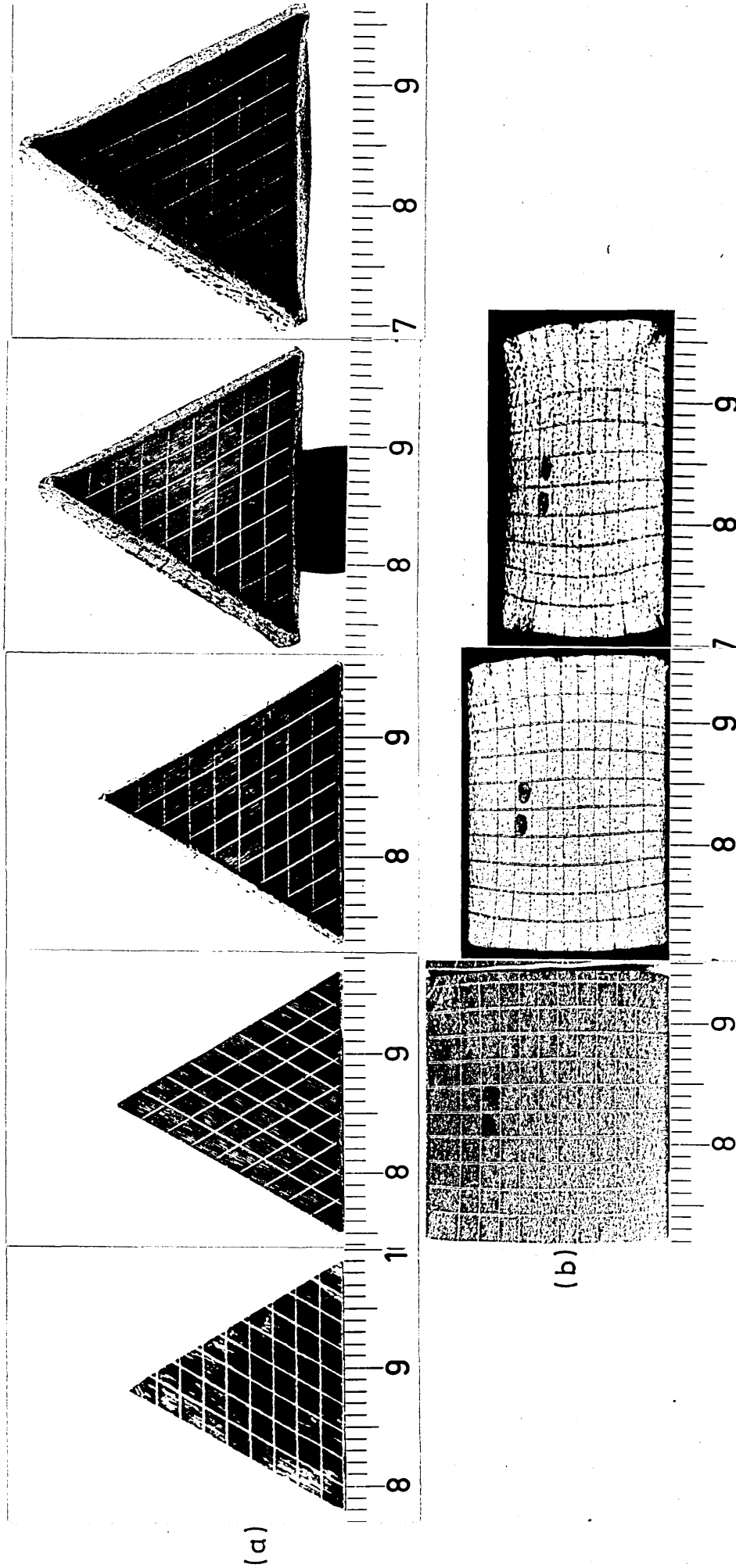


Fig (4.3c) Profile in progress for (a) top view and (b) side view of a specimen of triangular cross section, upset without using a lubricant

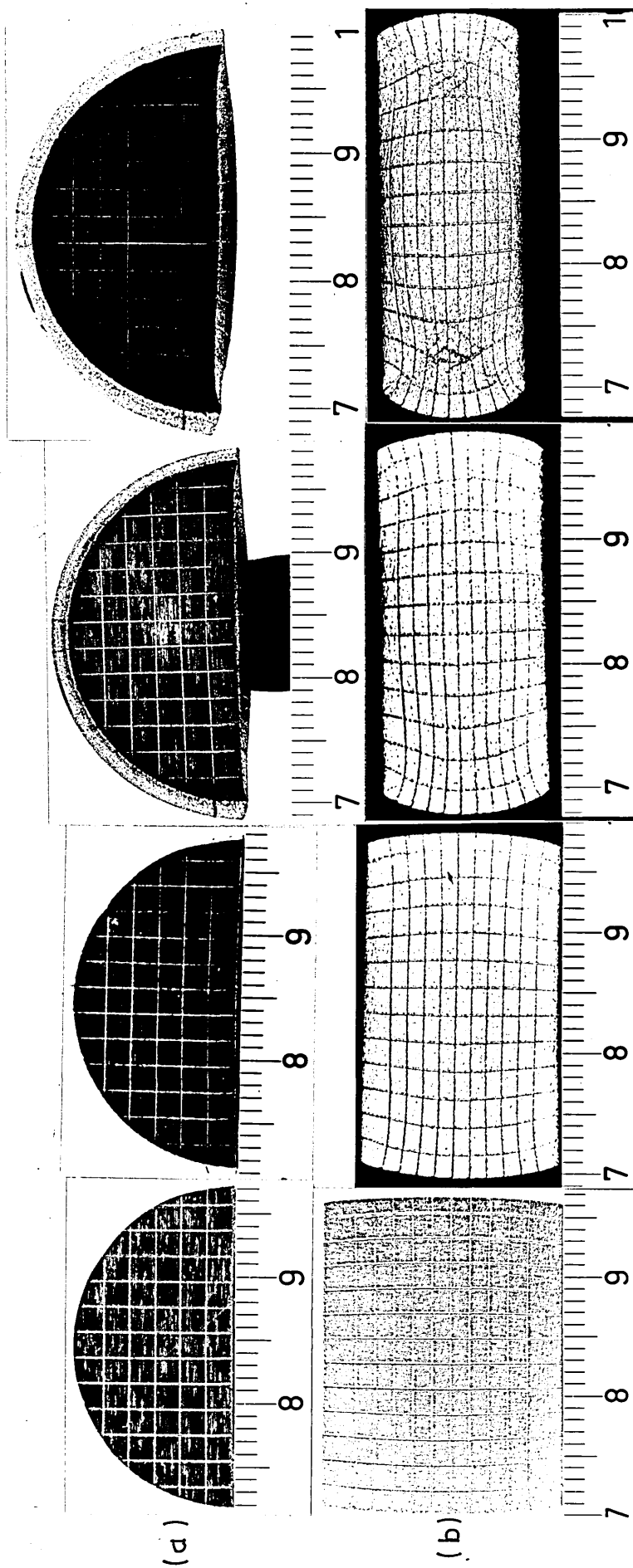


Fig (4.3d) Profile in progress for (a) top view and (b) side view of a specimen of a semi-circular cross section, upset without using a lubricant

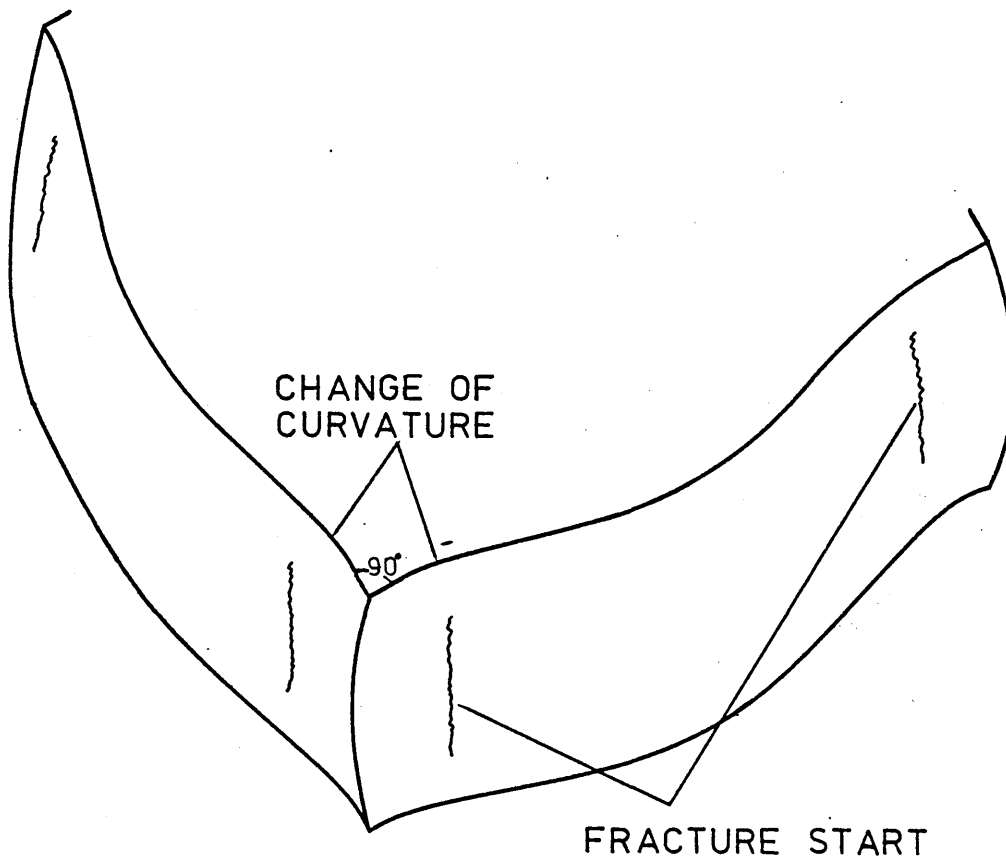


Fig (4.4) A sketch diagram of a specimen of square cross-section after being upset without using a lubricant

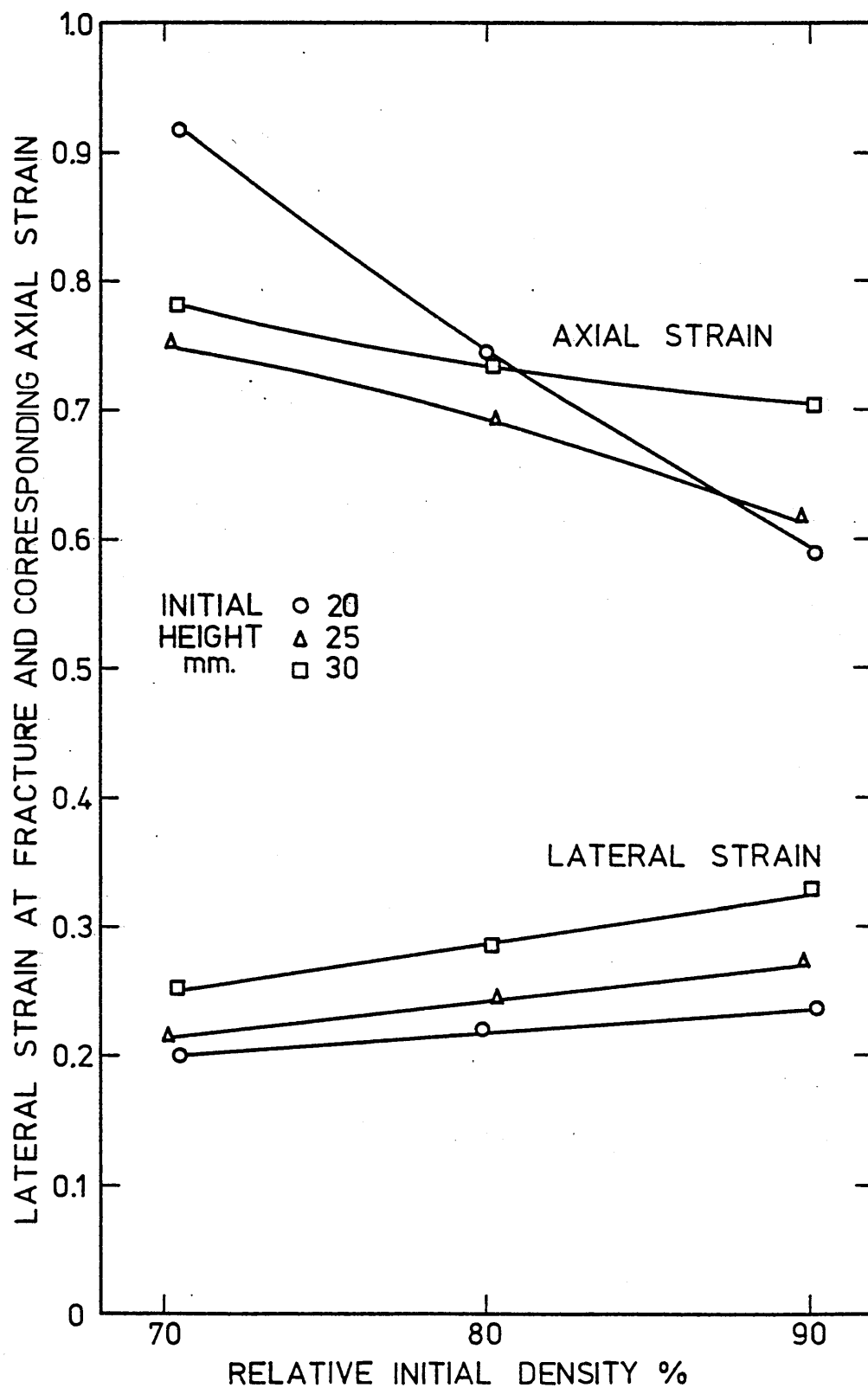


Fig (4.5) The effect of initial density and height on the degree of straining before fracture during upsetting of cylindrical billets

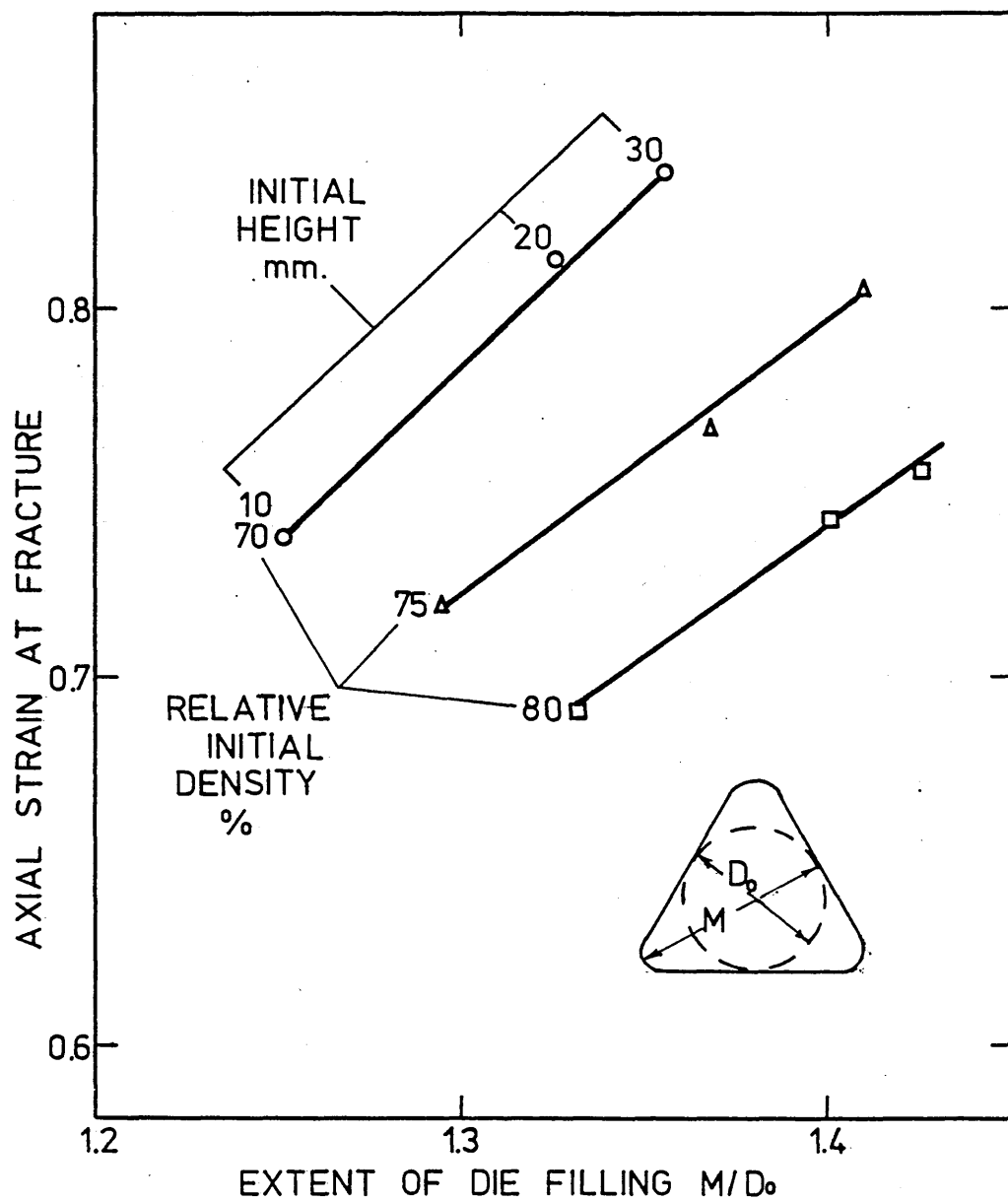


Fig (4.6) The variation of axial strain with the extent of die filling for specimens of three initial densities and heights, forged in a triangular die cavity till fracture

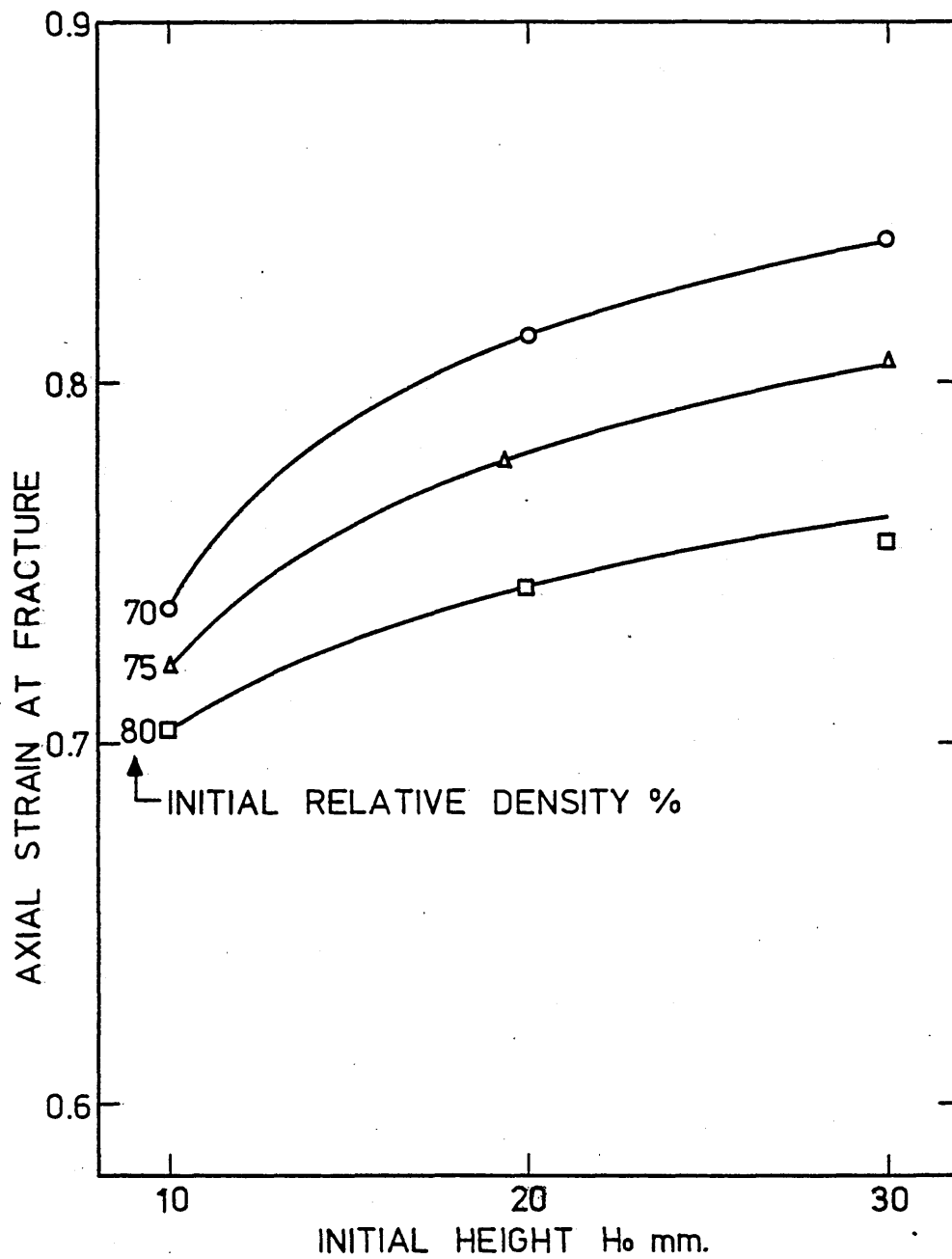


Fig (4.7) The variation of axial strain with the initial height of specimens of three initial densities, when forged in a triangular die cavity till fracture

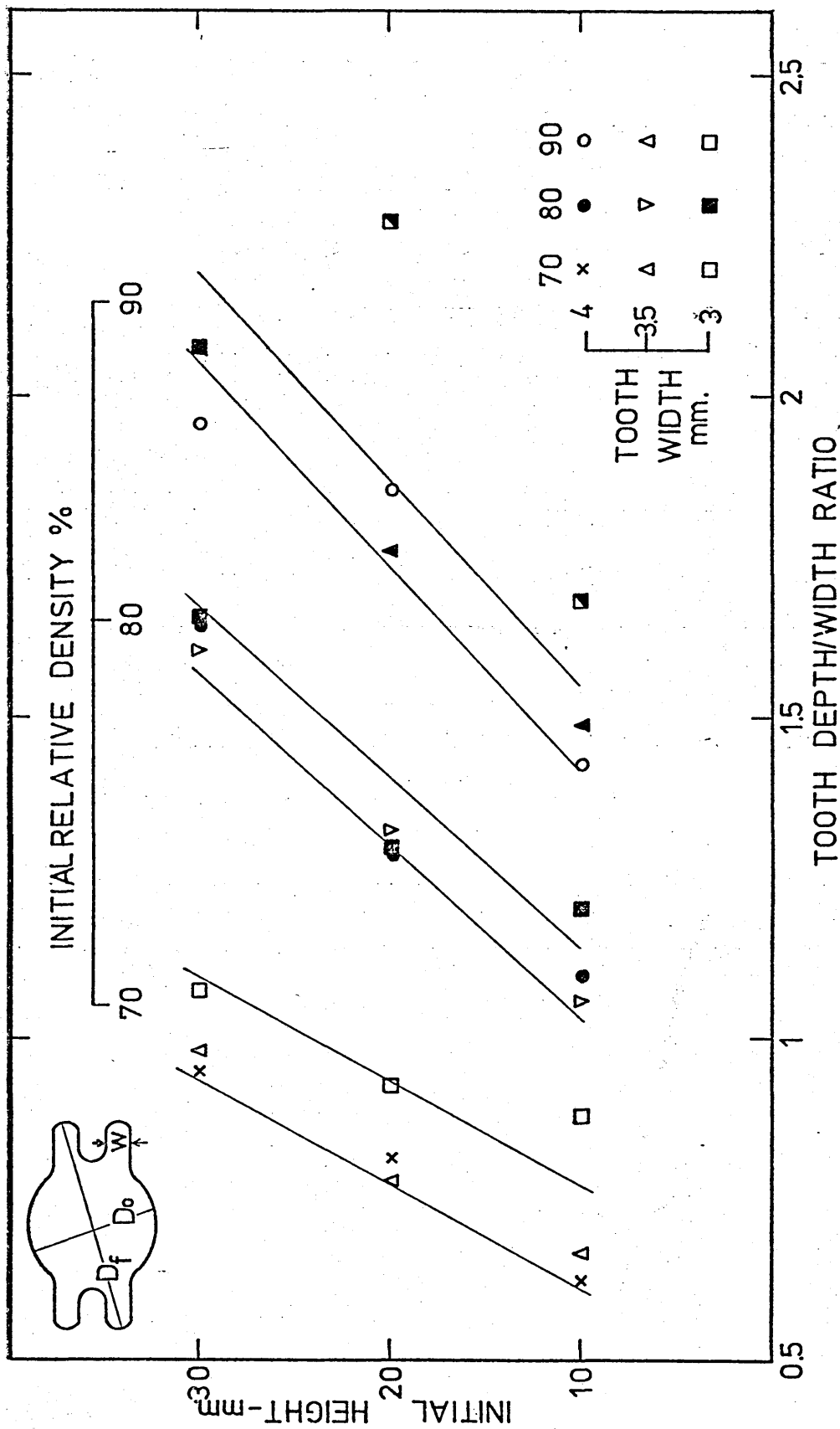


Fig (4.8a) The effect of height on cavity filling for specimens of three initial densities, when forged into cavities of three widths

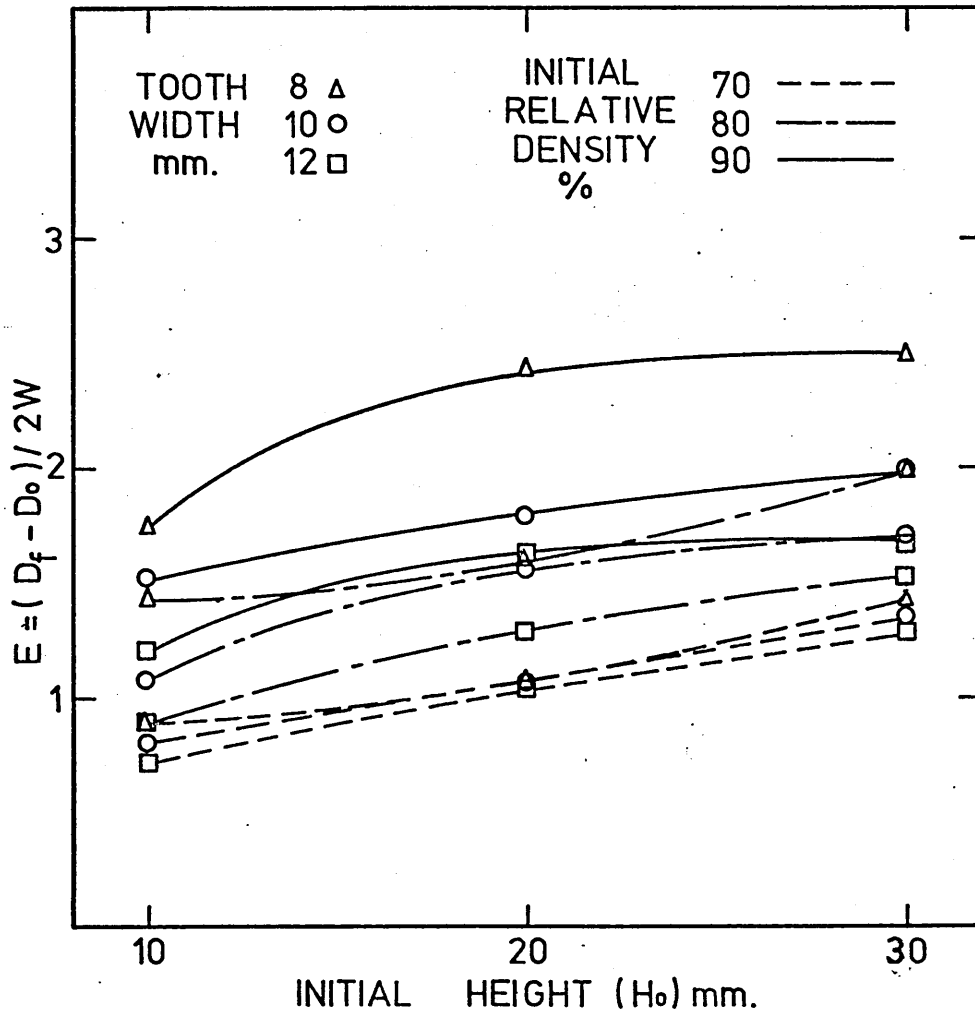
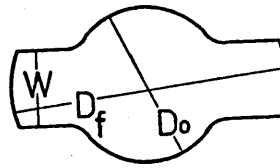


Fig (4.8b) Extent of cavity filling v initial height
for specimens of three initial densities, when
forged into cavities of three widths

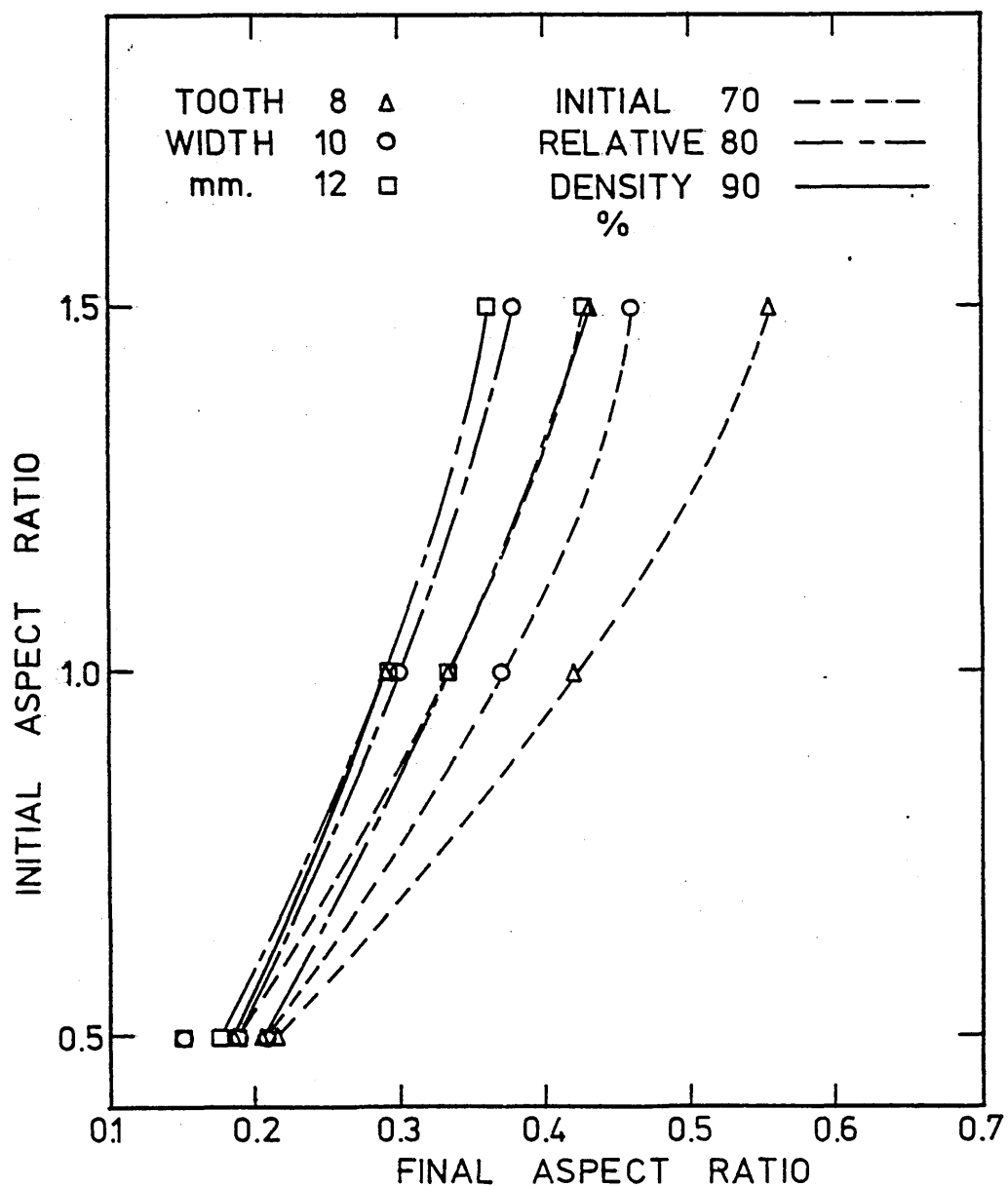


Fig (4.9) The variation of initial aspect ratio with final aspect ratio of specimens of three initial densities when forged into cavities of three widths

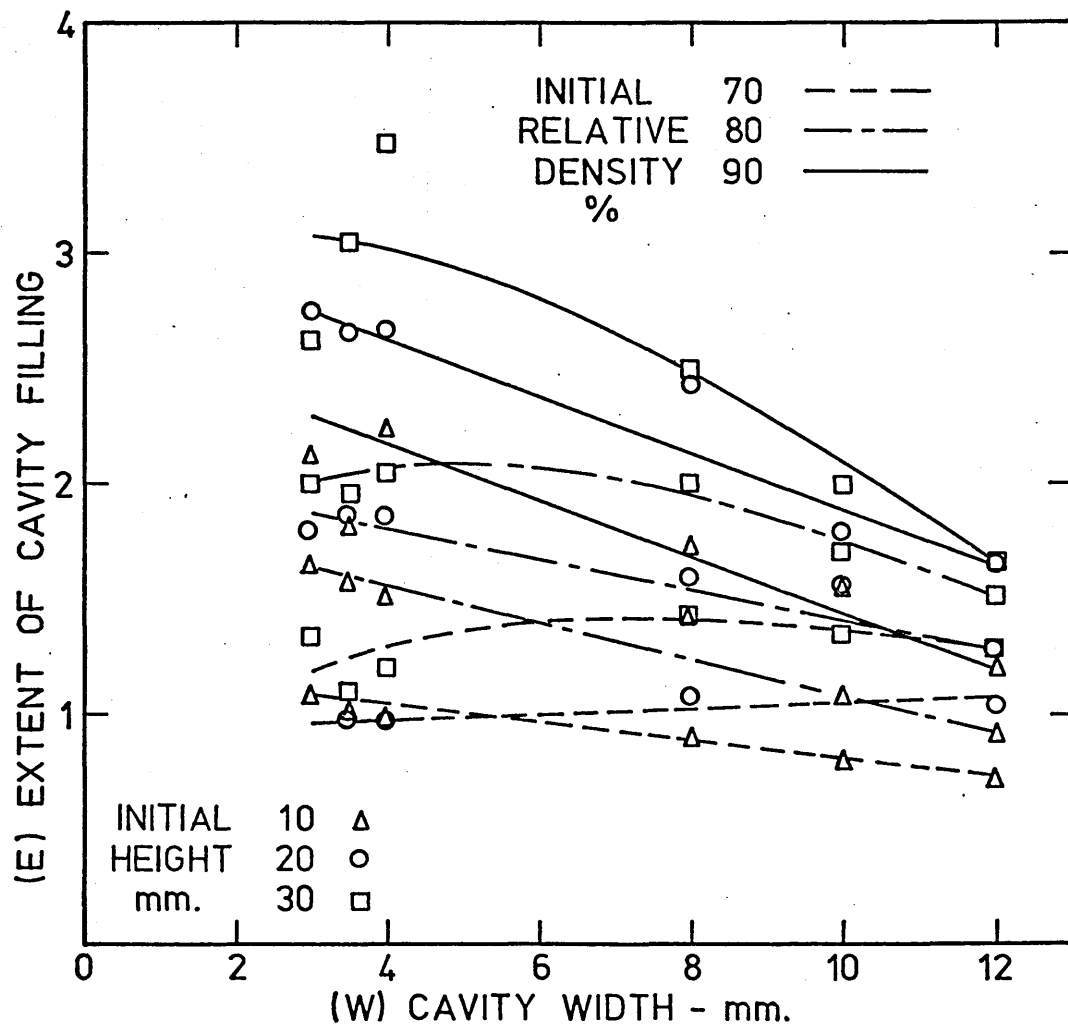
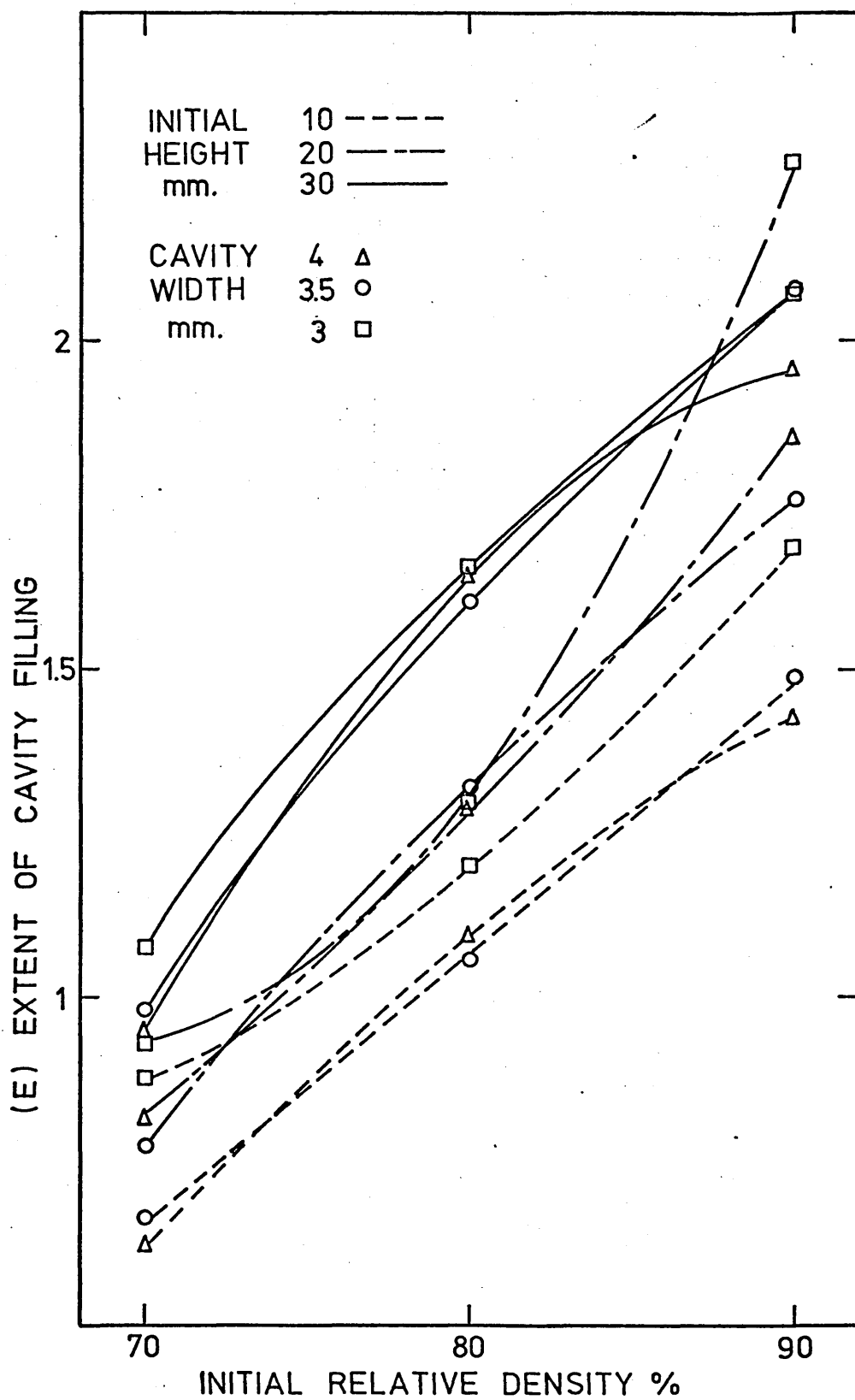


Fig (4.10) The extent of cavity filling v cavity width
for specimens of three initial densities and heights
forged till fracture



Fig(4.11a) The effect of initial density on the extent of cavity filling ($E = ((D_f - D_o)/W)$) of specimens of three initial heights, forged into cavities of three widths

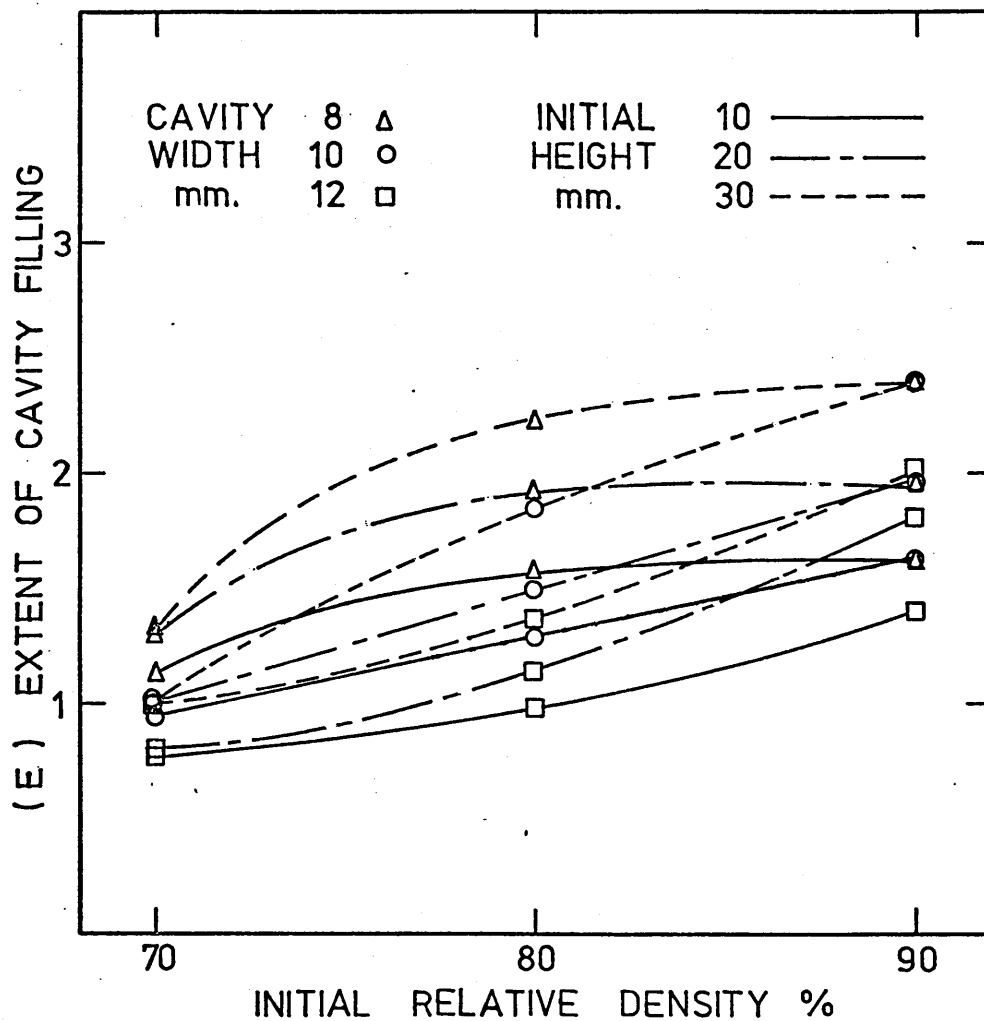
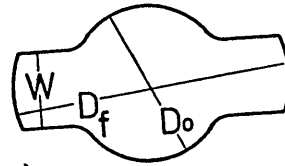


Fig (4.11b) The effect of initial density on the extent of of cavity filling for specimens of three initial heights forged into cavities of three widths

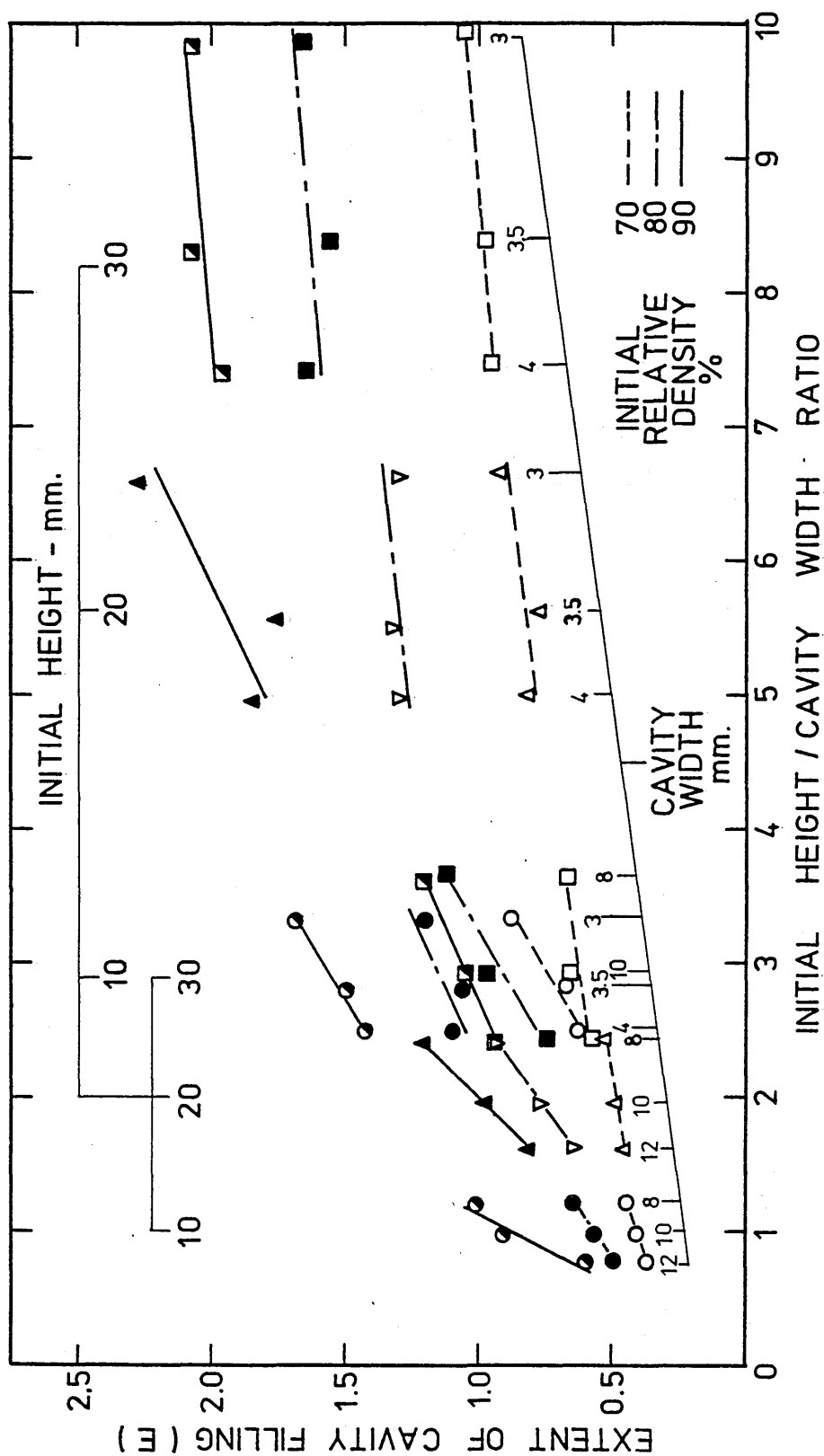


Fig (4.12) The extent of cavity filling versus the ratio of initial height/cavity width for specimens of three initial densities and heights, forged into cavities of six widths

PLASTIC FLOW CHARACTERISTICS OF POROUS MATERIAL

5.1 Plasticity Theory for Sintered Materials

For the development of a theoretical solution to the plastic deformation of any material, a yield criterion must be established first, and followed by a flow rule giving the relationships between stress and strain. For fully dense materials, the Von-Mises yield criterion and Levy Mises flow rules are applicable. This criterion is based on the constant volume assumption and yielding is a function of the second invariant of the stress deviator J'_2 , hence the yield surface is given by

$$\begin{aligned} P^2 &= (3 J'_2) \\ &= ((\sigma_1 - \sigma_2)^2 + (\sigma_2 - \sigma_3)^2 + (\sigma_3 - \sigma_1)^2)/2 \dots (5.1) \end{aligned}$$

where P denotes the flow stress and σ_1 , σ_2 and σ_3 are principal stresses. From the normality flow rule, the stress-strain relationships are obtained (59), assuming that the plastic strain increment is normal to the yield surface, hence

$$d\epsilon_i = d\lambda \quad \partial P / \partial \sigma_i \quad \dots (5.2)$$

where $d\epsilon_i$ denotes plastic strain increment in direction i

σ_i denotes principal stress

$d\lambda$ denotes positive proportionality constant

By differentiating Equation 5.2, a complete set of equations of stress-strain increments are provided:

$$\begin{aligned} d\epsilon_1 &= d\lambda \left[\sigma_1 - (\sigma_2 + \sigma_3)/2 \right] \\ d\epsilon_2 &= d\lambda \left[\sigma_2 - (\sigma_1 + \sigma_3)/2 \right] \\ d\epsilon_3 &= d\lambda \left[\sigma_3 - (\sigma_1 + \sigma_2)/2 \right] \end{aligned} \quad \dots\dots\dots (5.3)$$

For porous materials, however, densification and hence change in volume, takes place during the deformation process and therefore the approach for fully dense materials ceases to apply. Also the hydrostatic stress component becomes effective on yielding, hence the yield surface is given by:

$$P_s^2 = F (J'_2, J'_1) = \alpha J'_2 + \beta J_1 \quad \dots\dots\dots (5.4)$$

where P_s is the flow stress of the sintered material, J_1 denotes the first invariant of stress, which is equivalent to the hydrostatic stress $(\sigma_1 + \sigma_2 + \sigma_3)/3$, and is given by $(\sigma_1 + \sigma_2 + \sigma_3)$, α and β are functions of the relative density.

Many attempts (47 - 52) have been made to modify the approaches based on Von-Mises yield criterion by introducing density as a function of the hydrostatic stress component (Equation 5.4), so that when full density is reached, the dependance of yielding on the hydrostatic stress component vanishes. Based on this, Kuhn and Downey (47) proposed a yield criterion in the form

$$P = [3J'_2 - (1 - 2\nu) J_2]^{\frac{1}{2}} \quad \text{..... (5.5)}$$

where ν is the plastic Poisson's ratio and is equal to 0.5 at full density. From a basic experimental programme ν was found to be equal to $0.5 \rho^{1.92}$, where ρ is the relative density of the material. In this case ν is a function of the relative density only and it is represented by the solid line in Figure 5.1, while the curved lines represent the actual experimental results obtained by Alkatib (33). Similar results were also obtained by Hagerty (34). This means that the Kuhn and Downey relation is valid only at large strains and that a more general relationship is required which should consider the effect of initial density.

Oyane, Shima, Tabata and Masaki (References 49 - 51) have proposed another parameter for the hydrostatic stress component in their analytical solution which is given by

the relation

$$f = \frac{2}{3} \left(\frac{d\varepsilon_1 - d\varepsilon_2}{d\varepsilon_v} \right)^{\frac{1}{2}} \quad \dots (5.6)$$

where $d\varepsilon_v$ is the volumetric strain increment and $d\varepsilon_1$ and $d\varepsilon_2$ are the principal strain increments. In an attempt to relate 'f' to the relative density graphically, an empirical relationship in the form

$$\frac{1}{f} = a (1 - \rho)^n \quad \dots (5.7)$$

was obtained by curve fitting where a and n are constantly equal to 2.5 and 0.5 respectively.

Furthermore, they obtained the stress-strain curves for pore-free material by utilising the basic equations of the proposed yield criterion, thus

$$\bar{\sigma}_{eq} = \frac{1}{f} \left[\frac{((\sigma_1 - \sigma_2)^2 + (\sigma_2 - \sigma_3)^2 + (\sigma_3 - \sigma_1)^2)}{2} + \left(\frac{\sigma_m}{f} \right)^2 \right]^{\frac{1}{2}} \quad \dots (5.8)$$

and

$$d\bar{\varepsilon}_{eq} = \frac{\bar{f}}{\rho} \left[\frac{2}{9} ((d\varepsilon_1 - d\varepsilon_2)^2 + (d\varepsilon_2 - d\varepsilon_3)^2 + (d\varepsilon_3 - d\varepsilon_1)^2) + (f d\varepsilon_v)^2 \right]^{\frac{1}{2}} \quad \dots (5.9)$$

where \bar{f} represents the ratio of the apparent stress applied to the porous body and the effective stress ($\bar{\sigma}_{eq}$) applied to the matrix material. The parameter

\bar{f} was considered as a function of the relative density and was determined from the yield stress-relative density curves in simple compression and tension tests and given by

$$\bar{f} = \rho^n \quad \text{..... (5.10)}$$

where $n = 2.5$

Both parameters f and \bar{f} , are independent of the initial density and consequently can only give average values with a large scatter when applied to higher strain values of practical importance.

Honess (60) carried out a comparative study between results from his experimental programme on sintered iron under various stress conditions and those given by yield criteria already proposed by others. He concluded that the Kuhn and Oyane yield criteria are best suited to describe the plastic behaviour of sintered iron.

Another comparative study was carried out by Corapcioglu and Uz (52) with an additional yield criterion proposed by Corapcioglu and Angan (61) which is again very similar to the ones already proposed by Kuhn, Green and Oyane (47 - 49) but with a different value for the hydrostatic stress dependent factor. Also they (52) presented a limiting

condition for yielding based on the assumption that plastic deformation may not be caused by yielding at high porosity levels but by shear, bending and collapse of pores.

The aim of the present work is to establish the effect of initial density on yielding and subsequently to establish a yield criterion which considers both the initial and final densities. The results will be compared with criteria postulated by previous workers.

5.1.1 Verification of Oyan's Criterion

The criterion proposed by Oyane et al (49) is chosen for verification and for possible modifications based on the results of the present experimental programme for sintered iron compacts. Special attention will be given to the effect of initial density on the solution.

5.1.1.1 Basic Equations

Equation (5.4) may be written as

$$P_s = \left[\{(\sigma_1 - \sigma_2)^2 + (\sigma_2 - \sigma_3)^2 + (\sigma_3 - \sigma_1)^2\} / 2 + \left(\frac{\sigma_m}{f} \right)^2 \right]^{\frac{1}{2}} \quad \dots (5.11)$$

where P_s is the yield surface of sintered material

σ_1, σ_2 and σ_3 are principal stresses

σ_m is the hydrostatic stress component =

$(\sigma_1 + \sigma_2 + \sigma_3) / 3$ and the parameter

f denotes the effect of $\dot{\sigma}_m$ on yielding which, in the present work, is considered to be a function of both the initial and final density.

In order to relate the flow stress of the porous material, P_s , to the equivalent flow stress of the solid matrix, $\bar{\sigma}_{eq}$, equation (5.11) may be re-written as

$$P_s = \bar{f} \bar{\sigma}_{eq} = \left[\{(\sigma_1 - \sigma_2)^2 + (\sigma_2 - \sigma_3)^2 + (\sigma_3 - \sigma_1)^2\} / 2 + \left(\frac{\sigma_m}{f} \right)^2 \right]^{\frac{1}{2}} \dots (5.12)$$

where \bar{f} represents the ratio of the flow stress of the porous material to the flow stress of the solid matrix.

The parameters f and \bar{f} may be determined experimentally and since experimentation values which are going to be used to incorporate the influence of the strain hardening of the matrix material, then equation (5.12) may be applicable to porous materials with strain hardening matrices.

The principal strain increments can be derived by partially differentiating the plastic potential g with respect to σ_1 , σ_2 and σ_3 which is given by

$$g = \frac{1}{\bar{f}} \left[\{(\sigma_1 - \sigma_2)^2 + (\sigma_2 - \sigma_3)^2 + (\sigma_3 - \sigma_1)^2\} / 2 + \left(\frac{\sigma_m}{f} \right)^2 \right]^{\frac{1}{2}} = \bar{\sigma}_0 \dots (5.13)$$

where $\bar{\sigma}_0$ is the yield stress of the material

Thus

$$d\epsilon_1 = d\lambda' \frac{\partial g}{\partial \sigma_1} = d\lambda \left\{ \sigma_1 - \left(1 - \frac{2}{9f^2}\right) \sigma_m \right\}$$

$$d\epsilon_2 = d\lambda' \frac{\partial g}{\partial \sigma_2} = d\lambda \left\{ \sigma_2 - \left(1 - \frac{2}{9f^2}\right) \sigma_m \right\}$$

$$d\epsilon_3 = d\lambda' \frac{\partial g}{\partial \sigma_3} = d\lambda \left\{ \sigma_3 - \left(1 - \frac{2}{9f^2}\right) \sigma_m \right\} \dots (5.14)$$

and the volumetric strain increment

$$d\epsilon_v = d\epsilon_1 + d\epsilon_2 + d\epsilon_3 = \frac{d\rho}{\rho} = d\lambda \frac{2}{3f^2} \sigma_m \dots (5.15)$$

Now if an equivalent strain increment referred to the relative matrix is denoted by $d\bar{\epsilon}_{eq}$, then the plastic work done per unit volume of the porous body, dW , is given by

$$dW = \sigma_1 d\epsilon_1 + \sigma_2 d\epsilon_2 + \sigma_3 d\epsilon_3 = \rho \bar{\sigma}_{eq} d\bar{\epsilon}_{eq} \dots (5.16)$$

Note, that since a unit volume of a porous body with a relative density ρ consists of the matrix material of volume ρ , then dW is not equal to $\bar{\sigma}_{eq} d\bar{\epsilon}_{eq}$.

Substituting Eq (5.14) in to Eq (5.16) and rearranging we find

$$d\lambda = \frac{3\rho}{2\bar{f}^2} \frac{d\bar{\epsilon}_{eq}}{\bar{\sigma}_{eq}} \dots (5.17)$$

following Oyan's (49) mathematical manipulation we have

$$d\bar{\sigma}_{eq} = \frac{\bar{f}}{\rho} \left[\frac{2}{9} \{ (d\epsilon_1 - d\epsilon_2)^2 + (d\epsilon_2 - d\epsilon_3)^2 + (d\epsilon_3 - d\epsilon_1)^2 \} + (f d\epsilon_v)^2 \right]^{\frac{1}{2}} \dots (5.18)$$

5.1.1.2 Determination of f and \bar{f}

By substituting into equations (5.14) and (5.15) the conditions of uniaxial compression, $\sigma_2 = \sigma_3 = 0$ and $\sigma_m = \sigma_1/3$ we get:

$$(d\epsilon_1 - d\epsilon_2)/d\epsilon_v = 9f^2/2 \quad \dots\dots\dots (5.19)$$

from equation (5.12)

$$\bar{\sigma}_{eq} = (\sigma_1/\bar{f}) (1 + 1/9f^2)^{\frac{1}{2}}$$

$$\text{or } \sigma_1 = \bar{f}\bar{\sigma}_{eq} (1 + 1/9f^2)^{\frac{1}{2}} \quad \dots\dots\dots (5.20)$$

In order to determine f and \bar{f} , the following experimental procedure was carried out:

1. Cylindrical compacts (20 mm dia x 25 mm height) were prepared from Hoganas atomised iron powder (AHC 100.29) mixed with 0.25% graphite using floating die compaction tools and zinc stearate suspended in Benzene as a die wall lubricant. Six density levels were prepared by varying the compaction load.

2. The compacts were sintered for 1 hour at 1120°C in a tube furnace with a controlled atmosphere of 10% Hydrogen, 90% Argon.
3. The sintered specimens were machined to equal heights and finish and the sintered density was measured.
4. The specimens were upset incrementally between polished flat dies at equal reductions of height of 2 mm each with PTFE sheets (0.125 mm thick) as lubricant. After each increment the load and the specimen height and diameter were noted and the PTFE sheets were renewed.
5. From these measurements the upsetting stress, σ_1 , the current density, ρ , the axial strain, ϵ_1 , the lateral strain, $\epsilon_2 = \epsilon_3$, and the volumetric strain, ϵ_v , were calculated and plotted in Figures 5.2, 5.3 and 5.4.

The values of the function f were then calculated using equation (5.19) and are plotted in Figure (5.5) against current porosity ratio $(1 - \rho)$. If we assume that f is a function of initial and final densities in the form

$$1/f = \rho_o^a (1 - \rho)^b \quad \dots\dots\dots (5.21)$$

where a and b are constants, then determination of a and b by computational regression analysis gives

$$1/f = 1.15 (1 - \rho)^{0.2533} / \rho_o^{1.066} \quad \dots\dots (5.22)$$

Also if the value of $1/f$ is calculated as a function of final density only, as in Oyane's solution, in the form of equation (5.21) the resultant expression is

$$1/f = 1.87 (1 - \rho)^{0.3554} \quad \dots\dots (5.23)$$

Both values of $1/f$ as given by equations (5.22) and (5.23) are shown in Figure (5.5). From this figure, it can be clearly seen that $1/f$ cannot be taken as a function of current density alone and furthermore, even when the initial density is considered as in equation (5.22), the deviation from experimental values is still high enough to render the equations in these forms not to be an accurate representation of observed results.

The method suggested by Oyane et al for the calculation of \bar{f} was also inaccurate. As shown in Figure (5.6) (reference 33), the stress-density relationship cannot be represented by one straight line and consequently the value of \bar{f} could not be calculated.

Therefore, one should conclude that Oyane's approach is not as appropriate to sintered iron material as originally suggested.

5.2 Stress-Strain-Density Diagram

In order to illustrate the behaviour of sintered iron under uniaxial frictionless compression conditions the space diagram shown in Figure (5.7) was constructed by utilising the experimental results already obtained (Reference 33). It is clearly shown how densification and strain hardening is affected by the initial density of the preform. On the right side of the diagram, ie at full density, stress-strain results obtained by testing annealed mild steel billets under the same conditions (Figure 5. 8) are included for comparison. For instance, the worked sintered iron could achieve a higher yield strength than annealed mild steel, despite a high porosity content.

Possibly at higher reductions the curves shown in the diagram (5.7) might merge with the mild steel curve but not necessarily at the same point. In fact, it has already been proven that higher stresses are required to fully densify specimens of lower initial density (reference 3).

It is believed that such a diagram is very informative and a useful aid to the designer of sintered components.

5.3 Yield Stress Space Diagram

To further the knowledge and understanding of the behaviour of sintered material under various stress conditions, one should establish a stress space diagram for the material under consideration as shown in Figure (5.9).

For the fully solid material, this diagram is represented by only one ellipse with its origin at the centre, ie the solid material yields at the same stress level in tension and in compression and its maximum shear stress is exactly one half its yield stress according to Tresca's yield criterion or equal to 0.57 its yield stress according to Von Mises yield criterion.

While for porous material, the behaviour is completely different as shown in Figure (5.9). Here, at every porosity level, we have a different yielding stress. Furthermore, the presence of pores and the process by which the powder was compacted and sintered may affect differently the behaviour of the material under various stress conditions.

The results presented in Figure (5.9) were obtained by three sets of tests. The results from frictionless upsetting tests are shown in Figure (5.16), the results from tensile tests of flat test pieces are shown in Table 5.1 and in Figure (5.10) and the results from torsion tests are shown in Figure (5.11).

As far as yielding is concerned as it is the subject of this diagram (5.9), the results obtained by the upsetting test are more accurate because the yield point can be easily identified by the temporary decrease of the applied pressure which is followed by a sharp increase in the deflection of the dial gauge. Such a demarkation point has not been observed during the tensile and torsion tests, hence, for these tests, the proof stress was obtained from the stress-strain diagram of each test. For the tensile tests, the stress-displacement plots obtained by the Instron testing machine were utilised and the proof stress was calculated at a 0.1% elongation. While for torsion tests, the torque at a 0.5° twisting angle was considered.

After examining Figure (5.9) it is obviously clear that the material does not yield similarly to wrought materials, since it yields under much lower stress levels in tension and torsion conditions than in compression except at the higher porosity level (30%), such results are somewhat

contrary to expectations.

5.4 Analysis of Simple Upsetting of Cylindrical Billets of Porous Material Using a Finite Difference Numerical Technique

In this study a finite-difference numerical technique was used to analyse theoretically the deformation behaviour of sintered iron compacts during upsetting operations. This numerical technique had previously been developed and reported in references (73, 74) in connection with analysing simple upsetting of cylindrical billets of elastic strain hardening and strain rate sensitive material. The stress-strain property of sintered iron compacts is of course, dependent on the relative density, a parameter which changes during the deformation process. This necessitates a variable relative density dependent material property to be incorporated in any analytical method for predicting deformation characteristics of such materials. To this end the above mentioned numerical technique was modified and used to study the simple upsetting of the sintered iron compacts. The basic principles and assumptions involved in the technique are:

1. The billet could be idealised to be made up of a number of concentrated masses connected to each other by massless links of circular cross-section which possess the same strength properties as the material of the billet.
2. The plane sections remain plane throughout the deformation process.
3. Uniform axial straining occurs within each individual link.
4. The frictional stress at the billet-tup interface is proportional to the normal stress on the face of the billet (Coulomb friction).
5. The radial expansion of each connecting link is governed by the condition of mass constancy.
6. There is no resistance to radial expansion of any link from the neighbouring link except for the links in contact with the top and bottom platens, in which case, interface friction forces resist radial expansion.

The technique essentially uses a lumped mass model for the actual billet and the procedure amounts to expressing the dynamic force equilibrium equations for each lumped mass in finite-difference form and relating the displacement of each lumped mass to the strain in the corresponding link. After each time interval the stress in each link and hence the axial force is determined from the material stress-strain characteristics.

5.4.1 Analysis

The general equation of motion for an element of the billet soon after deformation commences can be derived by considering the internal and inertia forces acting on the element, as shown in Figure(5.12 (a)), and is given by,

$$\frac{\partial N}{\partial s} = m \frac{\partial^2 u}{\partial t^2} \quad \dots\dots\dots (5.24)$$

Figure(5.12 (b)) shows the lumped parameter model for a number of elemental lengths of the billet illustrated in Figure(5.12 (a)). For convenience each elemental length Δs will be considered to consist of one concentrated mass and a massless link, and initially all elemental lengths are equal. This model replaces the actual billet by a mass-link system. Under the action of the internal and inertia forces, the position of each concentrated mass in the model

identifies the position of a corresponding elemental length of the actual billet. The finite-difference equation for the elemental length at the i 'th location of the model in Figure(5.12 (b)) is given by,

$$N_{i+1, j} - N_{i, j} - \Delta s_o^m \cdot \ddot{u}_{i, j} = 0 \quad \dots (5.25)$$

Equation(5.25) applies to all the elemental lengths along the billet and gives the instantaneous values of $u_{i, j+1}$ for any instant in time t_{j+1} when coupled with the following relationship between the acceleration and displacement in finite-difference notation.

$$u_{i, j+1} = \ddot{u}_{i, j} (\delta t)^2 + 2u_{i, j} - u_{i, j-1} \quad \dots (5.26)$$

The time increment δt is defined by

$$\delta t = t_{j+1} - t_j \quad \dots (5.27)$$

The change in length $\delta (\Delta s)_{i, t_{j+1}}$ of the link occurring during the time interval δt is

$$\delta (\Delta s)_{i, j+1} = \Delta s_{i, j+1} - \Delta s_{i, j} \quad \dots (5.28)$$

The strain increment occurring in the link during the time interval is,

$$\delta \epsilon_{i, j+1} = \frac{\delta (\Delta s)_{i, j+1}}{\Delta s_{i, 0}} \quad \dots (5.29)$$

The total strain in the link can now be determined thus,

$$\epsilon_{i, j+1} = \epsilon_{i, j} + \delta \epsilon_{i, j+1} \quad \dots (5.30)$$

since the time interval and, hence, the strain increment are both small.

In order to facilitate the calculation of stress which may vary across the end faces of the billet, when friction is present, it is necessary to idealise the actual cross-section to an equivalent section model which consists of a number of layers across each of which the stress is assumed to be uniform. The circular cross-section of the billet is assumed to consist of n discrete, evenly spaced layers of material of tubular cross-sectional area which can carry normal stresses. These layers are considered to be separated by a material which cannot carry any normal stress but has infinite shear rigidity.

With this simplified model the stress in the billet can be defined by the individual normal stresses at the n separate layers.

In order to determine the axial force acting in each link after the time interval δt the stresses in each layer of that link are calculated from the strain increment given by equation (5.20) and a known constitutive equation for the billet material given by

$$\sigma_{il} = F(\rho_o, \rho_c, \epsilon) \quad \dots (5.31)$$

where ρ_o and ρ_c are the original and current relative densities and ϵ is the current axial strain. ρ_c may be expressed as

$$\rho_c = F_1(\rho_o, \epsilon) \quad \dots (5.32)$$

so that equation (5.31) may be expressed in terms of ρ_o and ϵ only giving

$$\sigma_{il} = F_2(\rho_o, \epsilon) \quad \dots (5.33)$$

In order to incorporate the effect of friction at the tup-billet and billet-anvil interfaces, the magnitudes of the layer stresses for the links in immediate contact with the tup and the anvil are then modified by means of

the equation,

$$\sigma_{i\ell} = \sigma_{i1} \left[1 + 2\mu (R_i - R_{i\ell})/H \right] \dots\dots (5.34)$$

where μ is the frictional coefficient, H is the current billet height, R_i is the outer radius of the link and $R_{i\ell}$ is the mean radius of the layer. The effect of tup-billet and billet-anvil interface friction on the links other than in immediate contact is determined by use of a friction-cone analogy substantiated by experimental evidence. This analogy assumes two friction cones within the billet one at each end having a base coinciding with the interface area and a height depending on the coefficient of friction. The height of the cone is equal to the radius of the interface area when $\mu = 0.5$ and decreases proportionately to zero for $\mu = 0$. The stress in any layer of a link falling within the friction cone is also modified by equation (5.34).

The axial force N_i in the i 'th link is then obtained from the equation

$$N_i = \sum_{\ell=1}^n \sigma_{i\ell} \cdot A_{\ell} \dots\dots (5.35)$$

where A_l is the cross-sectional area of the layer calculated from the link area A_i . The link area A_i in turn is determined using the concept of the conservation of mass after each time interval δt , thus

$$A_{i,j+1} = \rho_{i,j} \cdot A_{i,j} \cdot \Delta s_{i,j} / (\rho_{i,j+1} \cdot \Delta s_{i,j+1}) \quad \dots (5.36)$$

where $\Delta s_{i,j+1} = \Delta s_{i,j} + \delta (\Delta s)_{i+j+1}$

At the end of each time interval δt the diameter of each link is calculated from the known cross-sectional area $A_{i,j+1}$ and the instantaneous profile of the billet is obtained by joining the mid-diametral points of all links. The cycle of computation described, is repeated until plastic deformation ceases.

5.4.2 Experimental Work

For the purpose of comparing experimental results with those predicted theoretically using the above described numerical techniques, data already obtained at other stages of this project were used. The corresponding theoretical results were obtained by feeding in appropriate data into the computer programme developed for this purpose.

5.4.3 Discussions

In order to demonstrate the ability to incorporate a density dependant material property, computer simulations of a simple upsetting process based on the lumped mass model were undertaken. Friction conditions varying from $\mu = 0$ to 0.5 were considered. The configuration of the billet and its finite-difference equivalent model used in the simulation studies are shown in Figure 5.13. The finite difference model consisted of 12 lumped masses. The experimentally derived quasi-static stress-strain characteristics given by,

$$\sigma = 641 \rho_o^{1.124} \epsilon (0.305 \rho_o)^{-2.3} \dots (5.37)$$

was incorporated into the simulation technique. It was estimated that strain rates of the order of 10^2 s^{-1} would be involved during the initial deformation period. However, in the absence of any accurate data regarding strain rate behaviour of the material under consideration, this effect was ignored in the analysis.

Instantaneous profiles were predicted for a number of billets upset under various frictional conditions. Figure (5.14) shows a series of profiles of a billet of 80 per cent initial density deformed under frictional condition given by $\mu = 0.25$. Figure (5.15) compares profiles at 50% reduction of height for various interface friction conditions at the top end of a 92% initial relative density specimen. While Figure (5.16) compares the top and bottom radii of the specimens in Figure (5.15) but for a wider range of initial densities. The variation in the radius with interface friction is shown in Figure (5.17). Billets of the same initial dimensions but different initial densities were analysed and the reduction in height is plotted against current radius as shown in Figure (5.18). The corresponding experimental results are also shown in this figure for comparison. Very good correlation is evident between the experimental and theoretical results.

The variation in the current density with reduction in height for a number of initial densities is shown in Figure (5.19). Experimental results are also shown for comparison and show very good agreement. Compression was carried out using PTFE as lubricant. Figure (5.20) shows

the relation between initial energy used with percentage reduction in height for various initial densities predicted theoretically when upsetting was carried out under lubricated end conditions.

When upsetting was carried out under frictional end conditions a variation in density was evident from hardness testing along the height of the billet. Theoretically predicted variations of density along the height of three billets of initial densities 70, 80 and 92 per cent are shown in Figure(5.21) for $\mu = 0.5$. It is evident that the density is higher at the mid-section of the billet and the variation is the maximum for 70 percent initial density. The effect of friction on the variation of mid-section radius of billets of 80 per cent initial density was predicted as shown in Figure(5.22). The experimental points correspond to upsetting tests with PTFE as lubricant. A similar effect is demonstrated in Figure (5.23) which shows plots of reduction of height against the extent of barrelling predicted theoretically for billets of 80 per cent initial density.

The quasi-statically determined density dependent stress-strain properties are shown in Figure(5.2) for initial densities ranging from 70 to 92 per cent. The empirical relationship given by equation (5.37) was derived from regression analysis of the experimental curves shown in this figure.

The variation in tup load with deformation is shown in Figure(5.24) for billets of initial densities of 70, 80 and 92 per cent and upset under lubrication conditions. Finally, the deformation against time under the same lubrication conditions is shown in Figure(5.25) for billets of initial densities of 70, 80 and 92 per cent. As expected the low density billet deforms at a higher rate than high density billets.

TABLE 5.1

Initial density %	Yielding load N*	Fracture load N	Total elongation mm/mm	Proof stress N/mm ²	Fracture stress N/mm ²
72.14	-	1700	0.015	-	94
72.14	121	1546	0.013	67.2	86
72.08	129	1540	0.019	71.7	86
76.4	140	2050	0.028	77.8	114
76.4	-	1970	0.019	-	109
76.18	138	1973	0.025	76.7	110
80.73	159	2540	0.040	88.3	141
80.90	154	2550	0.039	85.6	142
80.95	167	2585	0.047	92.8	144
85.50	186	3190	0.056	103.3	177
85.33	179	3335	0.075	99.4	185
85.39	181	3440	0.082	100.6	191
89.82	192	4290	0.100	106.7	238
89.88	177	4310	0.123	98.3	239
90.10	193	4380	0.133	107.2	243

* Yielding load was calculated at 0.1% elongation.

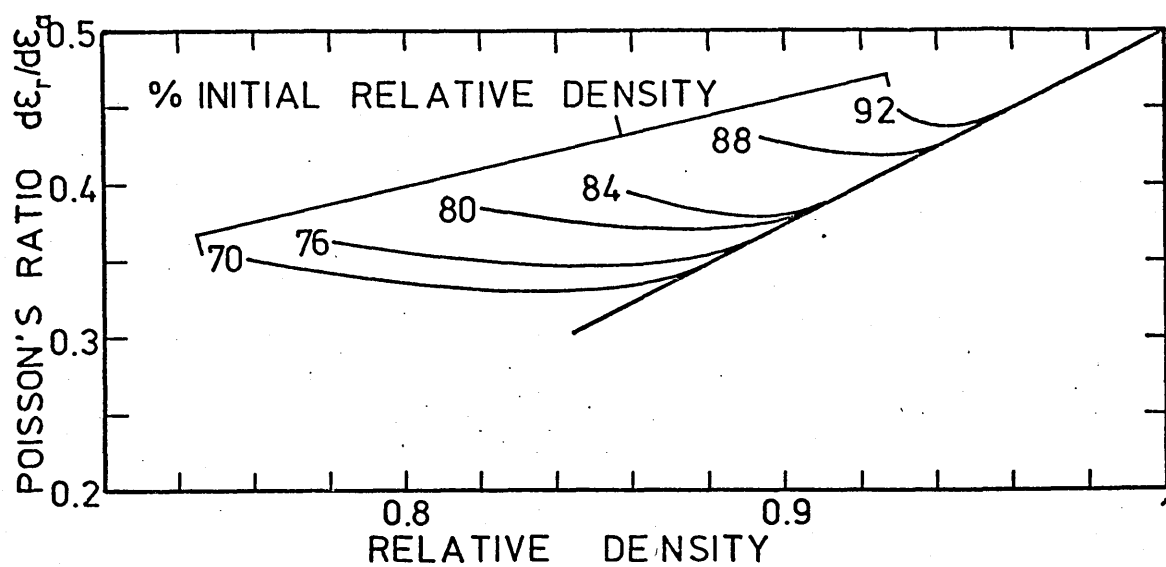


Fig (5.1) The variation of Poisson's ratio with the relative density of specimens of six initial densities during upsetting process (ref. 33)

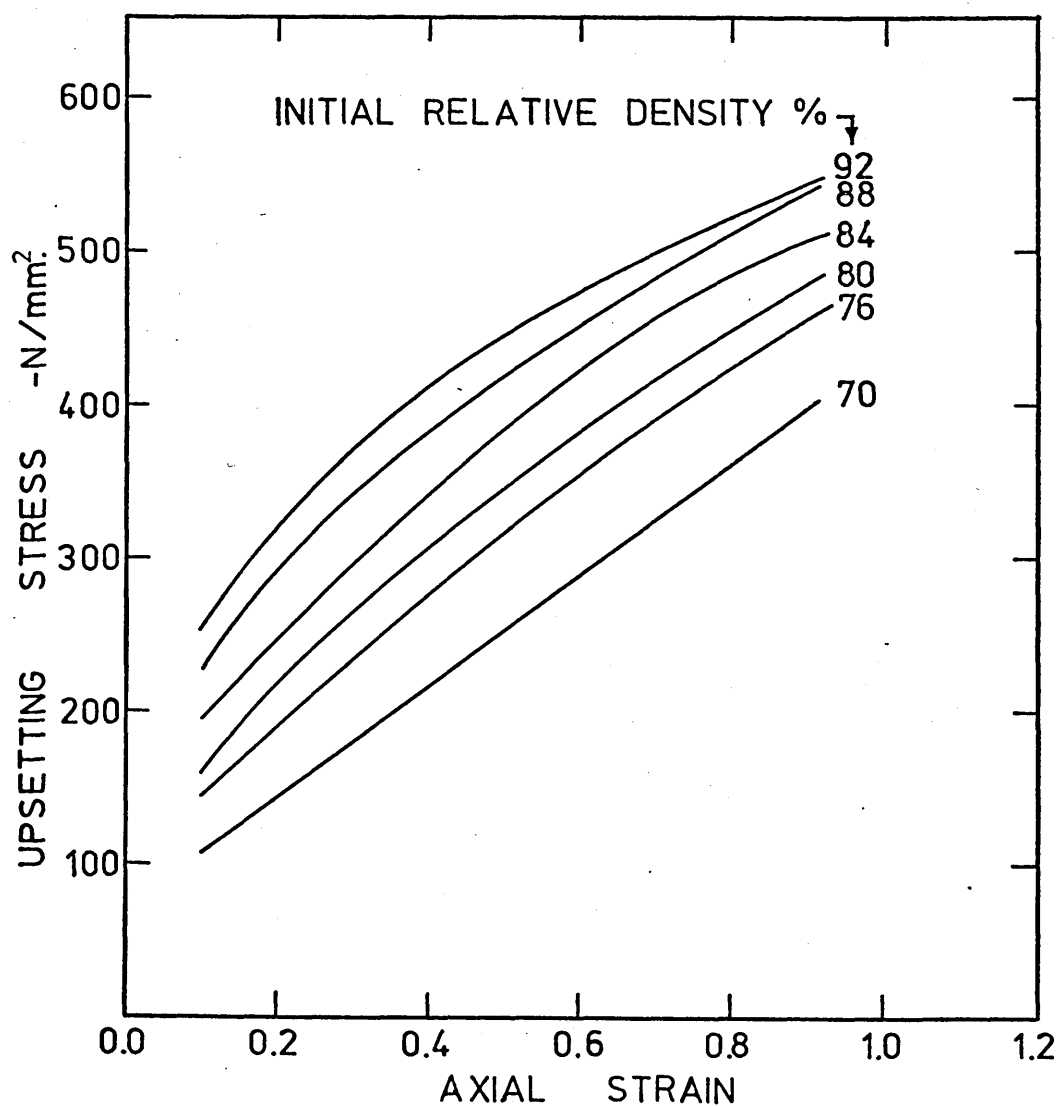


Fig (5.2) The stress-strain relationship of sintered iron material during frictionless upsetting process (ref. 33)

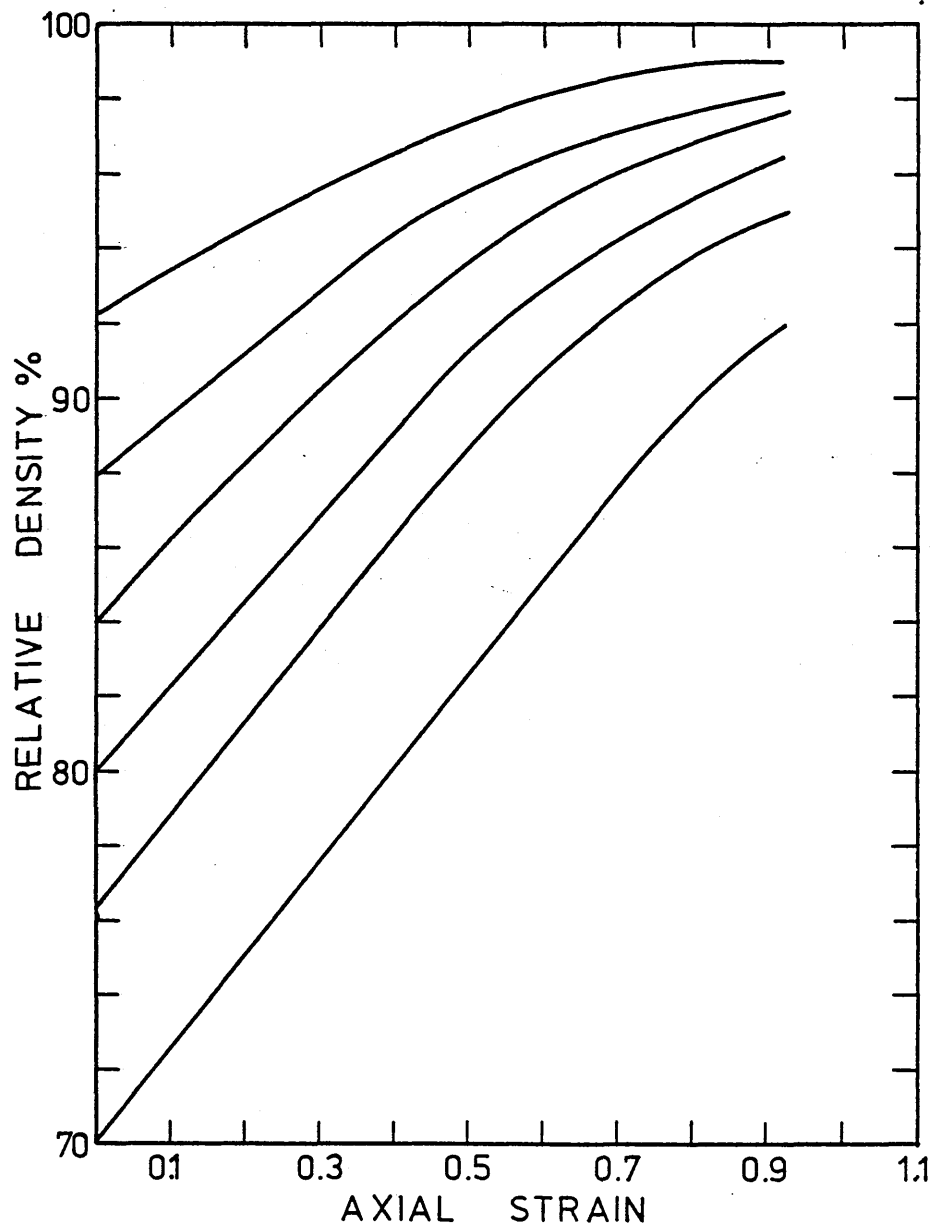


Fig (5.3) The variation of axial strain with the density of sintered iron specimens during frictionless upsetting process (ref 33)

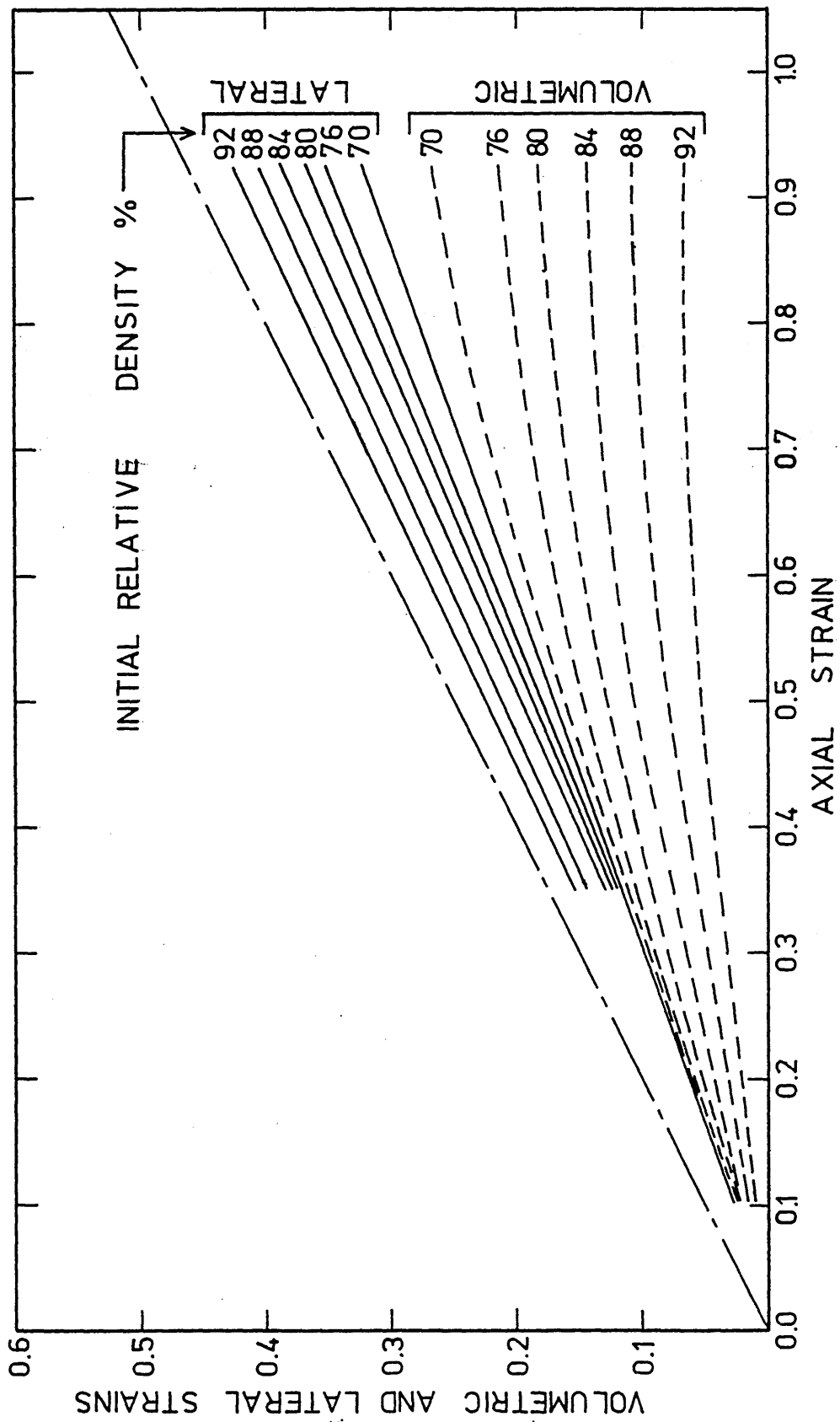


Fig (5.4) The variation of the volumetric and lateral strains with the axial strain of sintered iron specimens of six initial densities during frictionless upsetting process

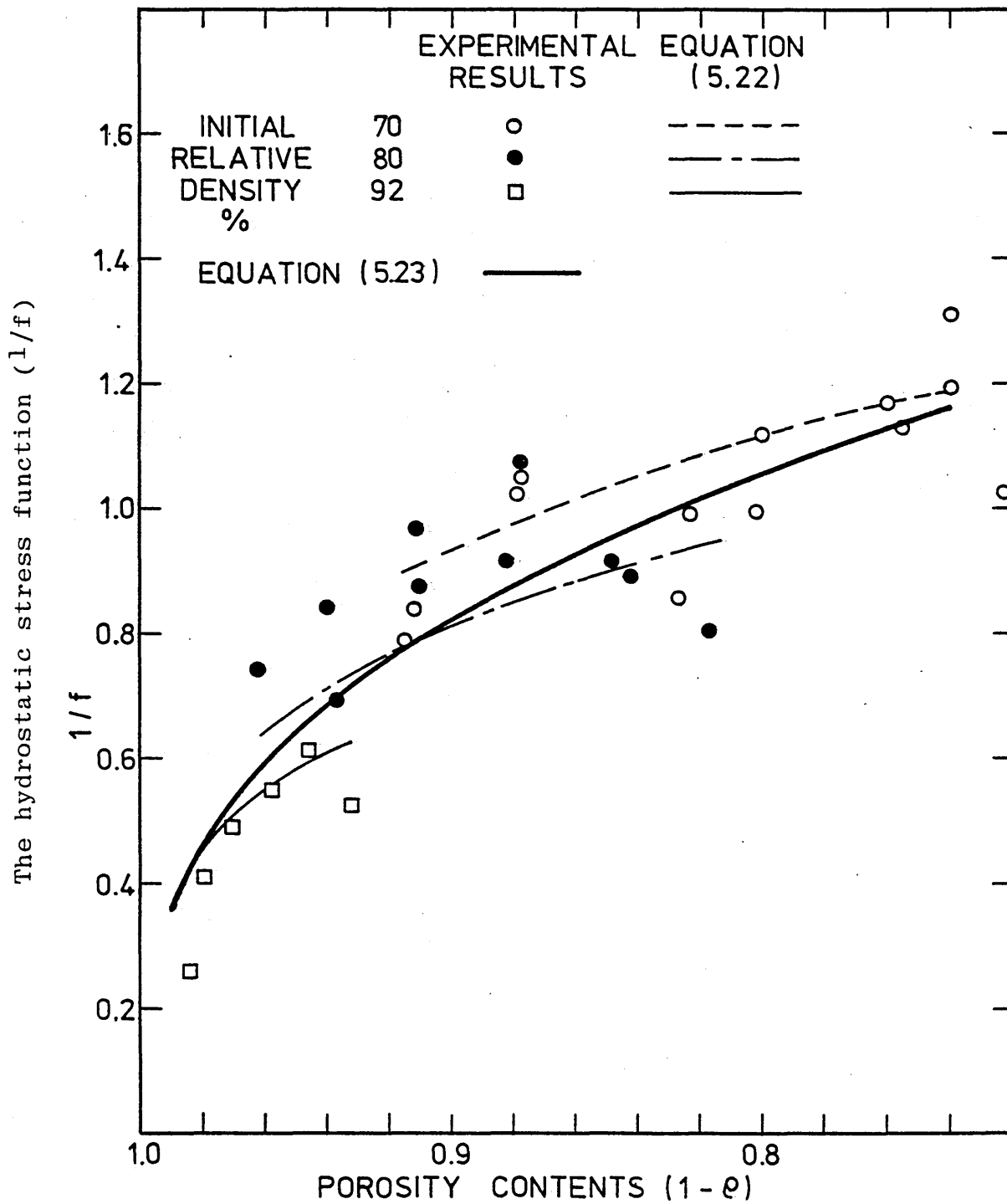


Fig (5.5) The variation of the hydrostatic stress function ($1/f$) with porosity for specimens of three initial densities during frictionless upsetting

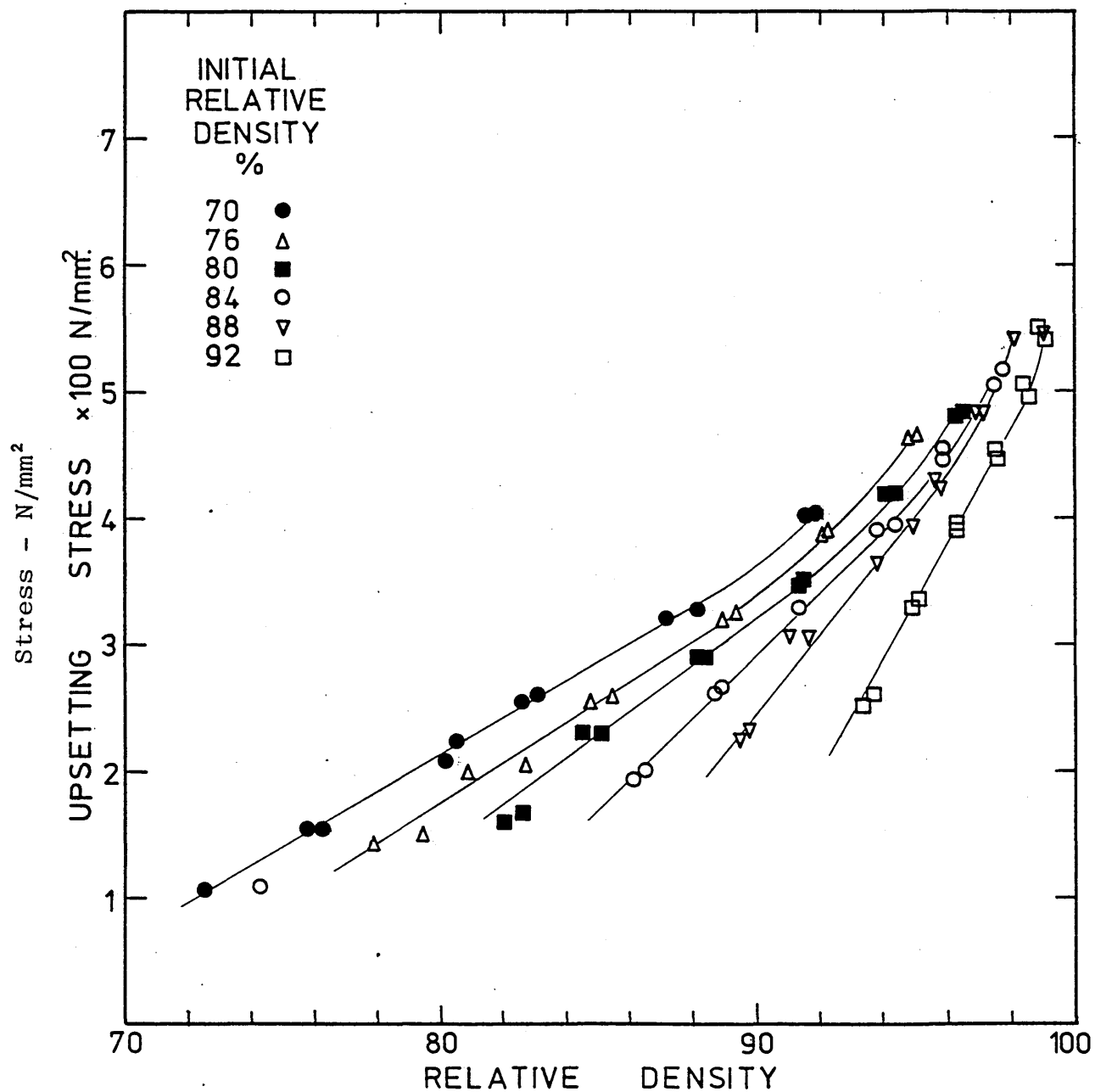


Fig (5.6) The effect of initial density on the stress-density relationship during upsetting (ref 33)

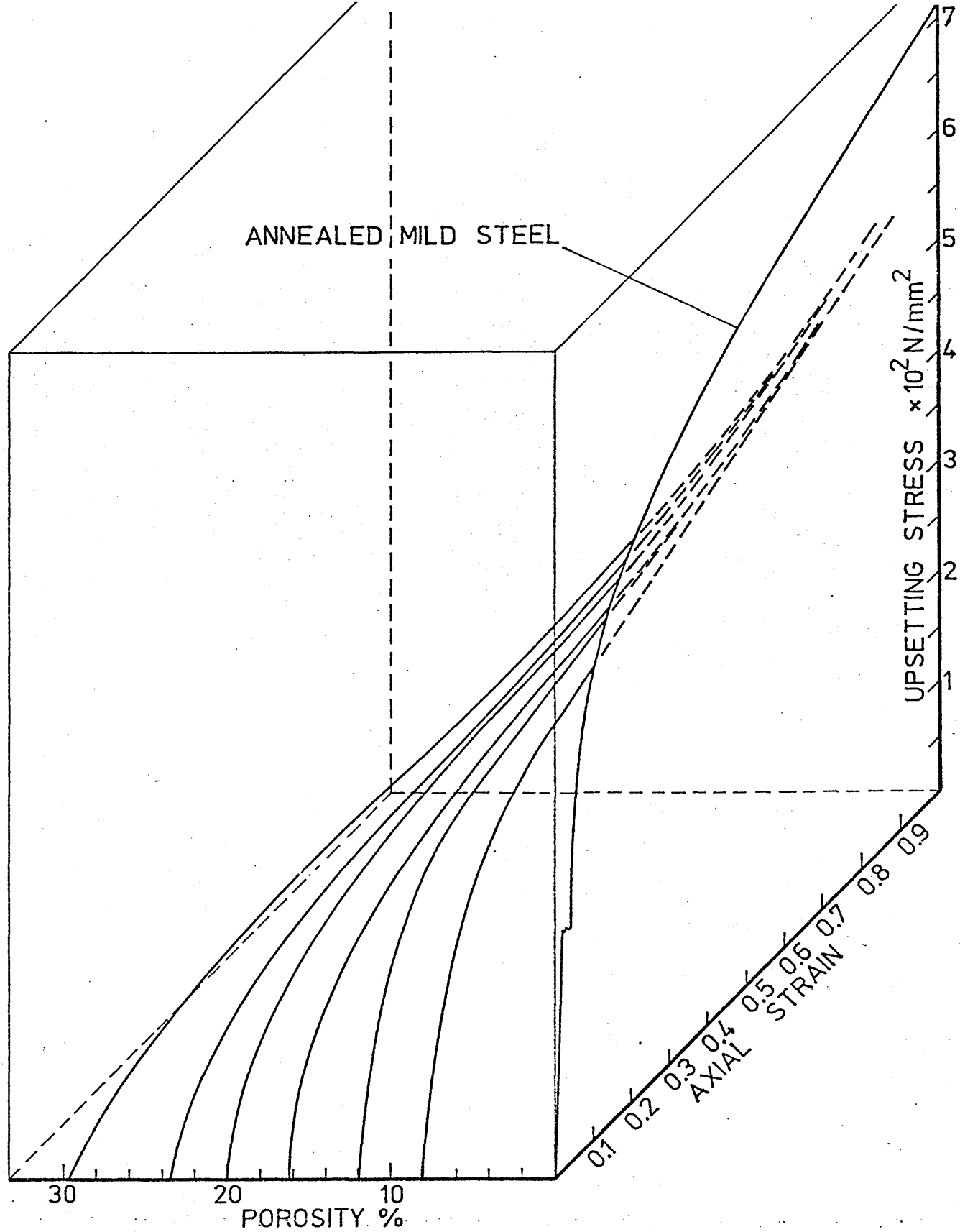


Figure (5.7) Stress-strain-density space diagram for sintered iron, uniaxially upset with PTFE sheets as lubricant.

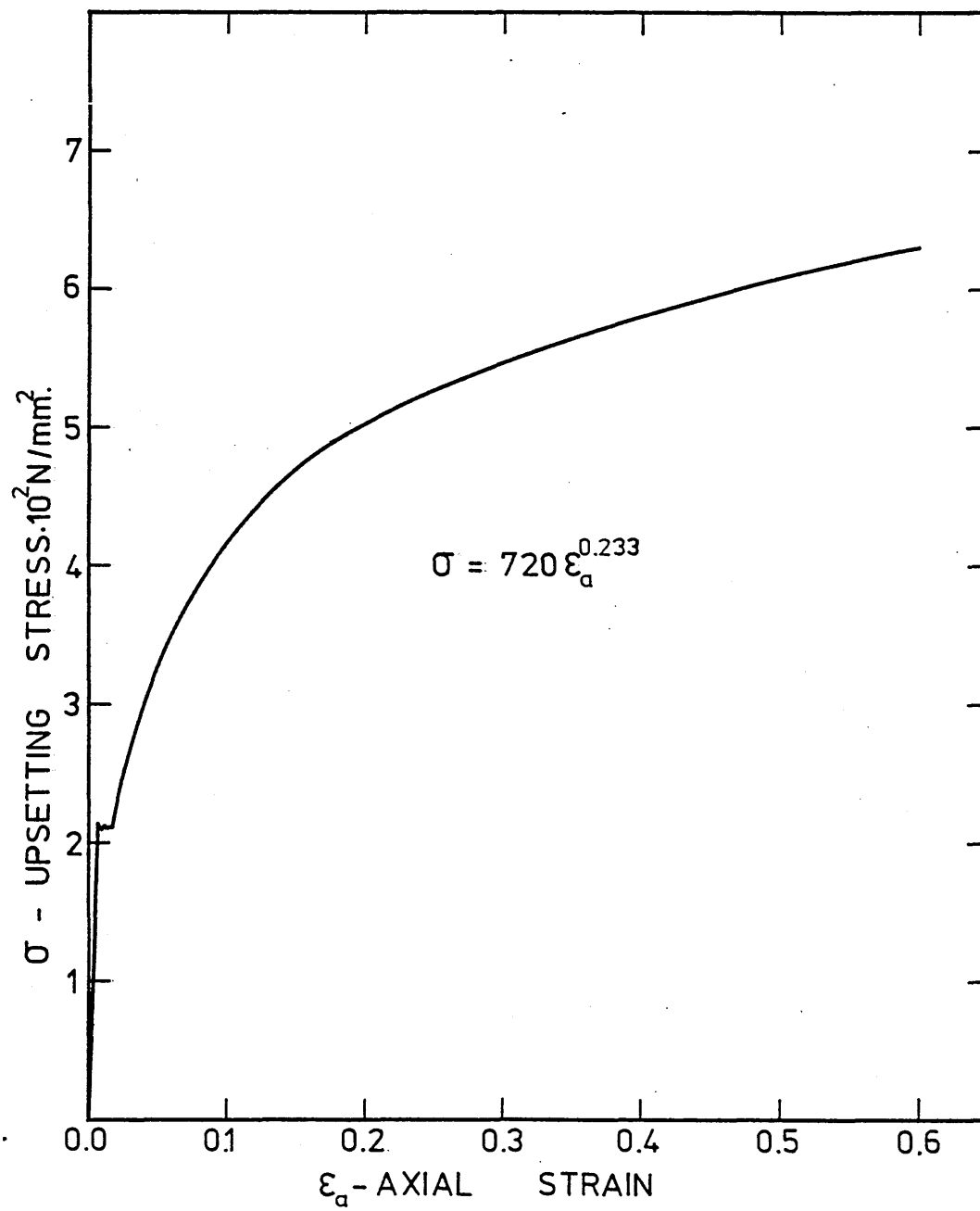


Fig (5.8) The stress-strain relationship of mild steel when upset with PTFE sheets as lubricant

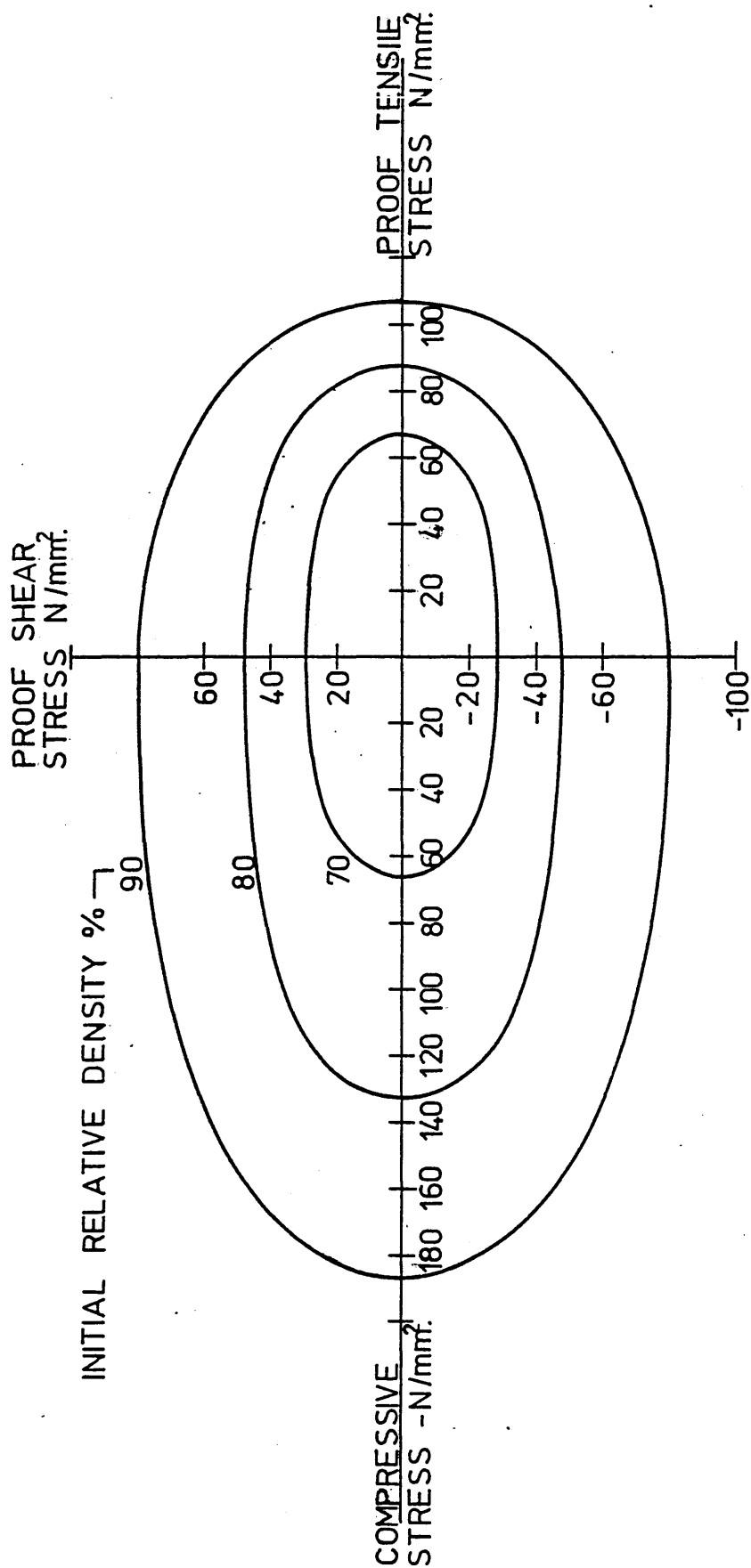


Fig (5.9) The stress space diagram of sintered iron at room temperature

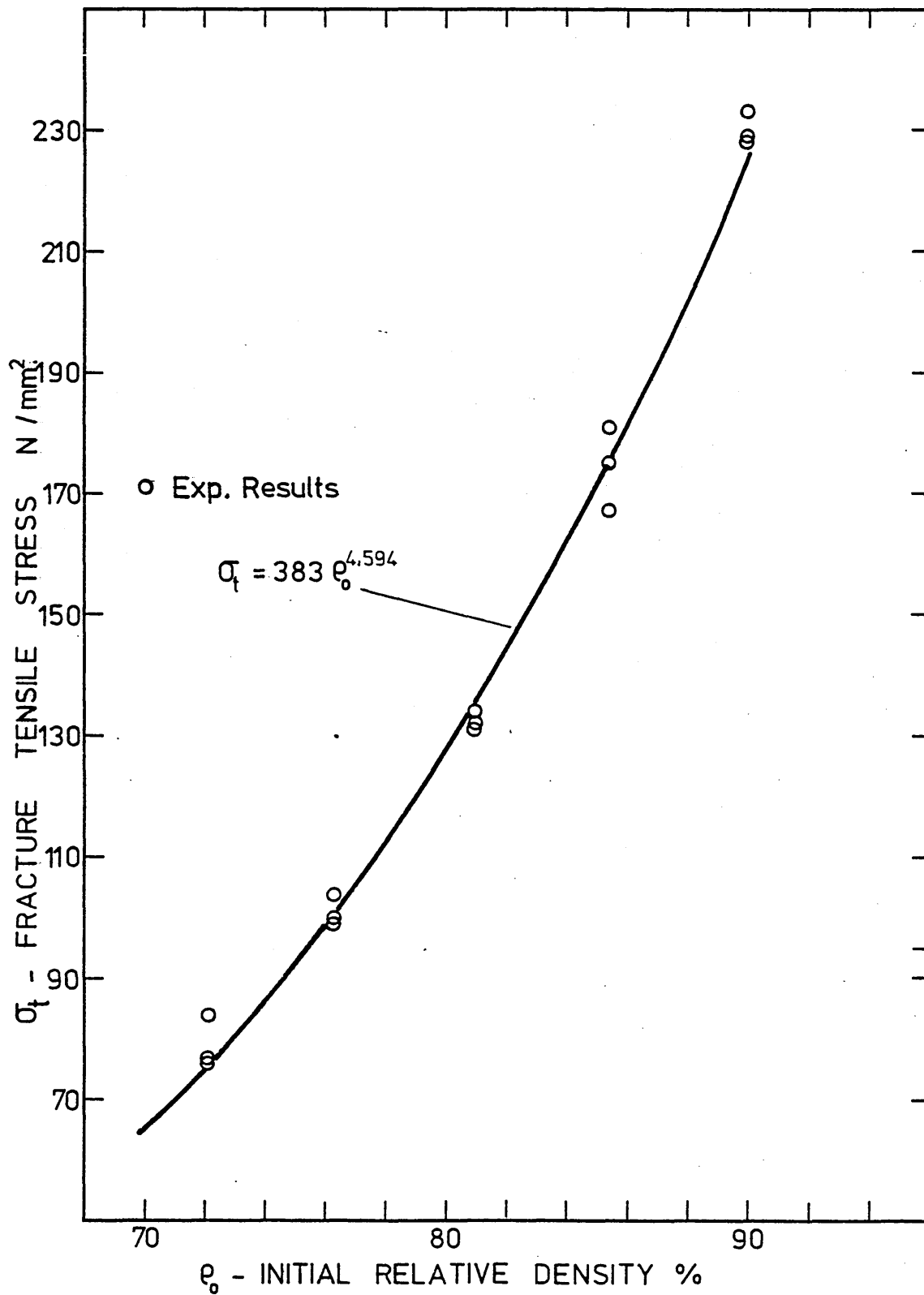


Fig (5.10) The variation of fracture tensile stress with the initial density of flat tensile testpieces of sintered iron

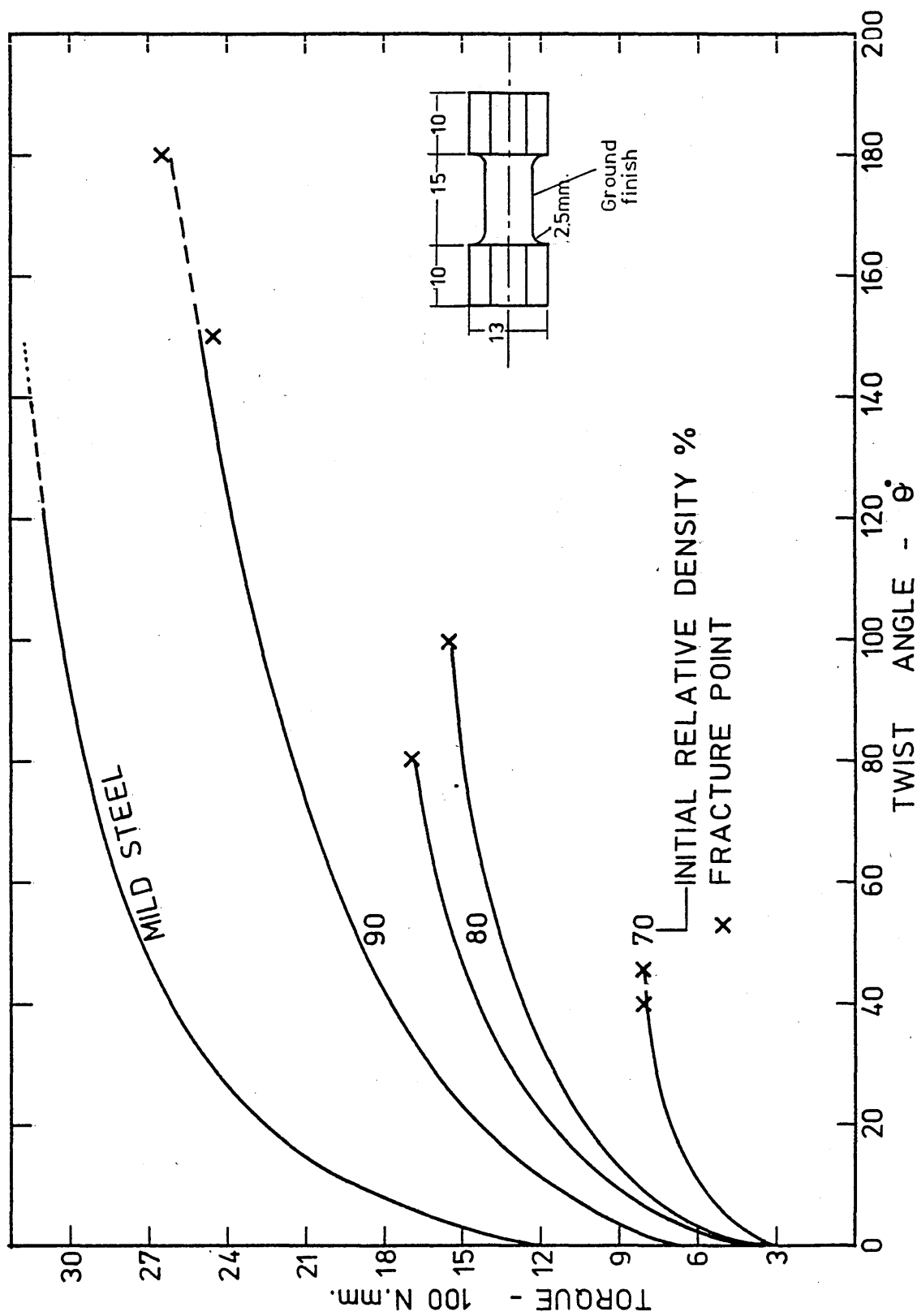
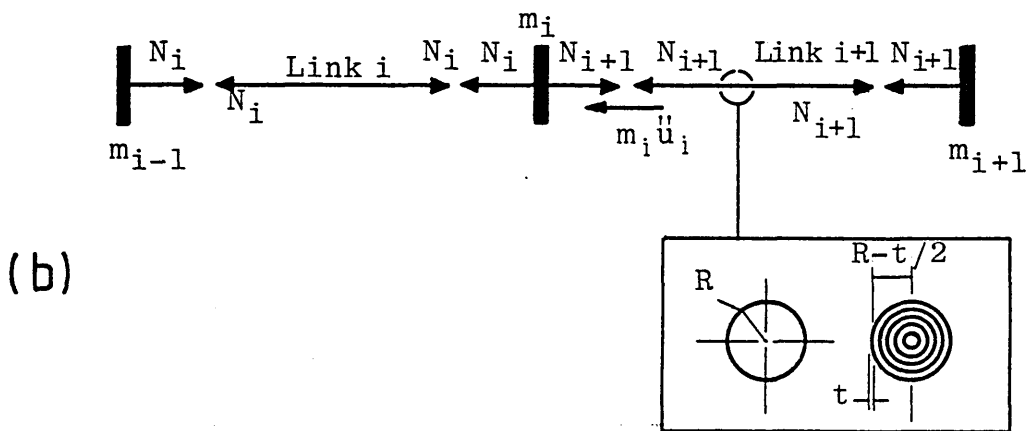
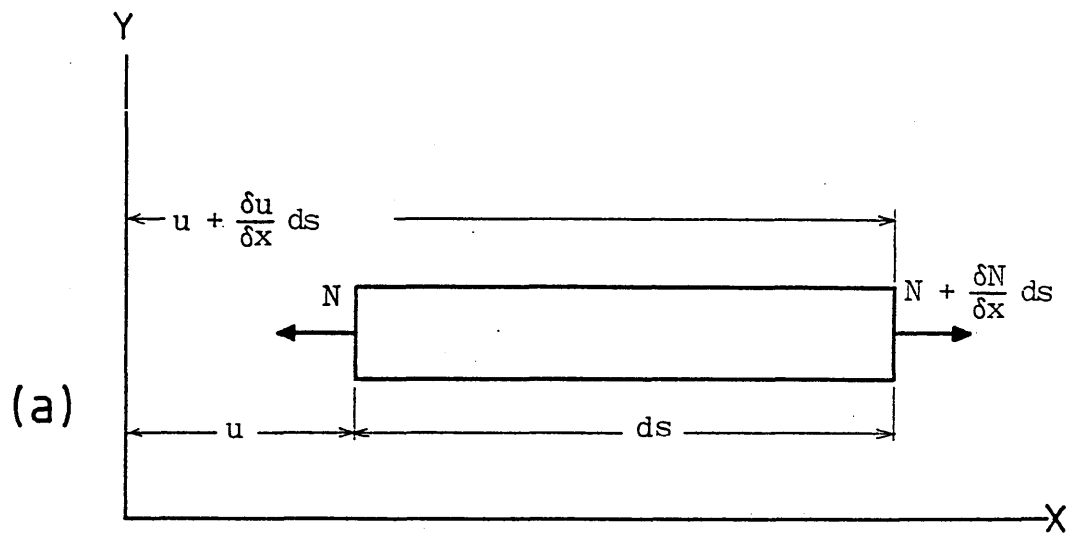


Fig (5.11) The torsional characteristics of sintered iron in comparison with that of mild steel



(Fig 5.12) (a) An element of the billet and forces acting on it

(b) Numerical model of the element in (a)

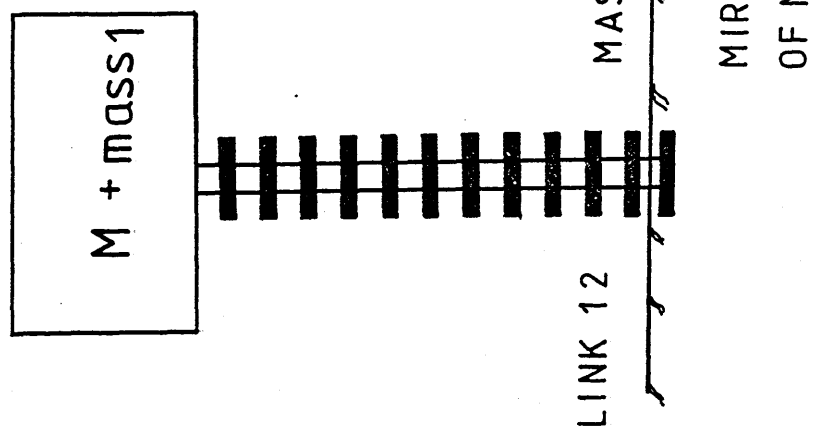
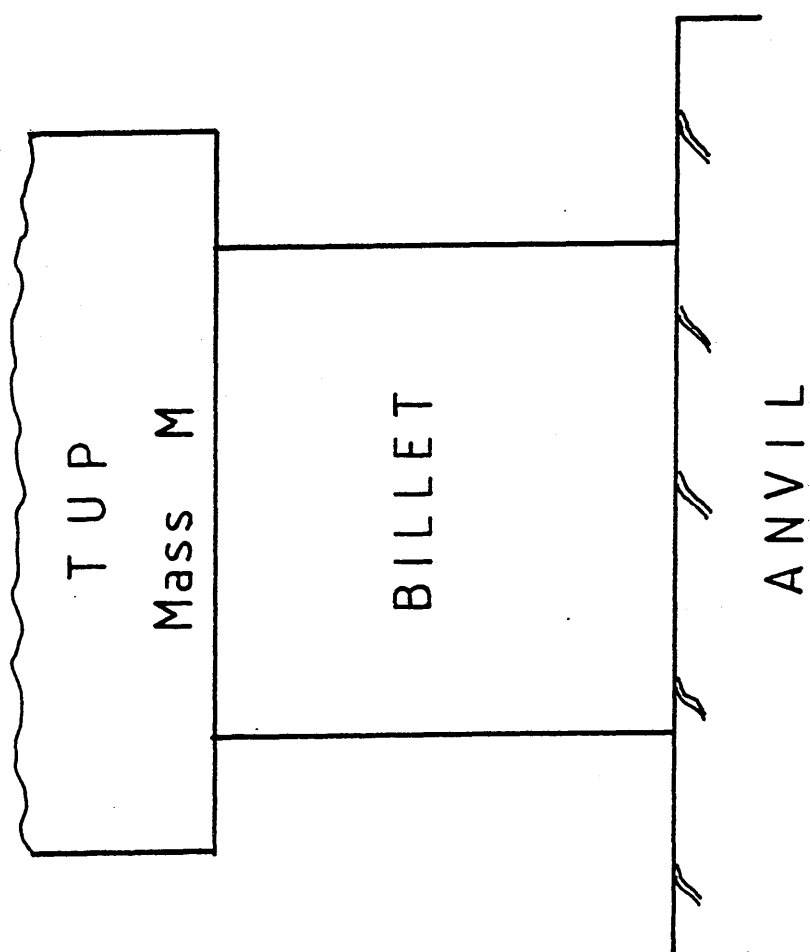


Fig (5.13) Actual loading configuration of the billet and its equivalent numerical model

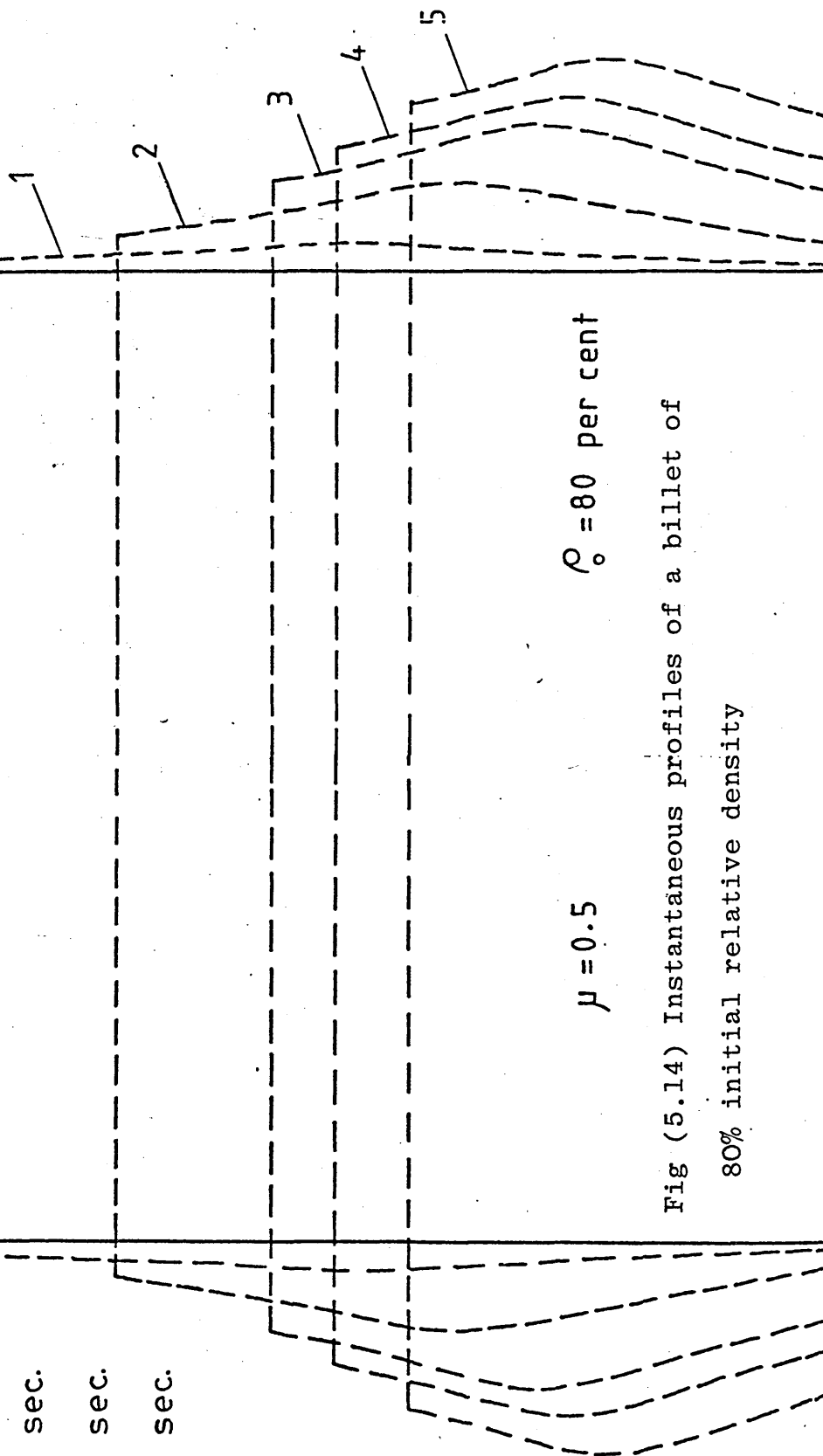
T U P

Undeformed Billet

$t_1 = 0.2$ m sec.
 $t_2 = 0.6$ m sec.
 $t_3 = 1.0$ m sec.
 $t_4 = 1.2$ m sec.
 $t_5 = 1.6$ m sec.

$\mu = 0.5$
 $\rho_0 = 80$ per cent

Fig (5.14) Instantaneous profiles of a billet of 80% initial relative density



A N V I L

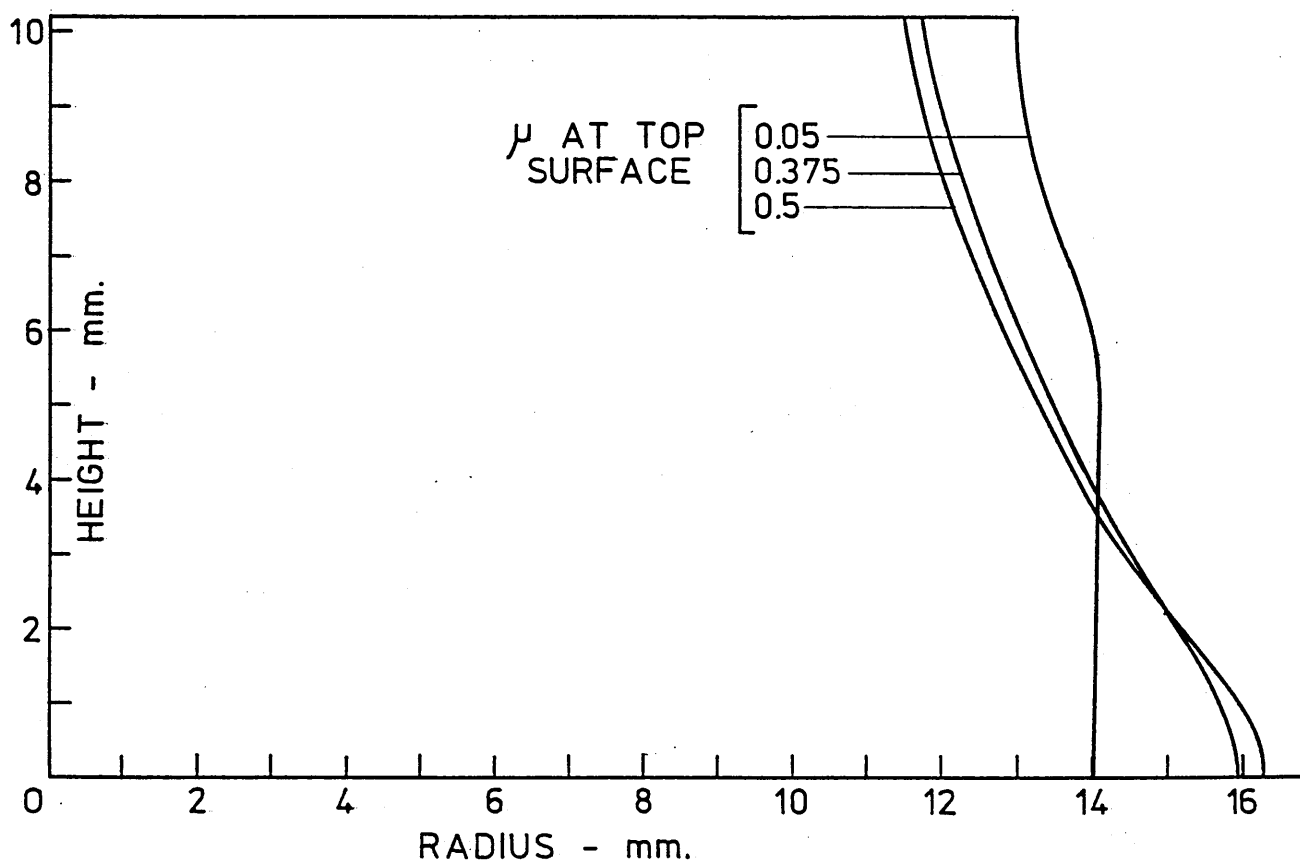


Fig (5.15) Comparison of profiles at 50% reduction of height for various interface friction conditions at the top end of a 92% initial relative density specimen

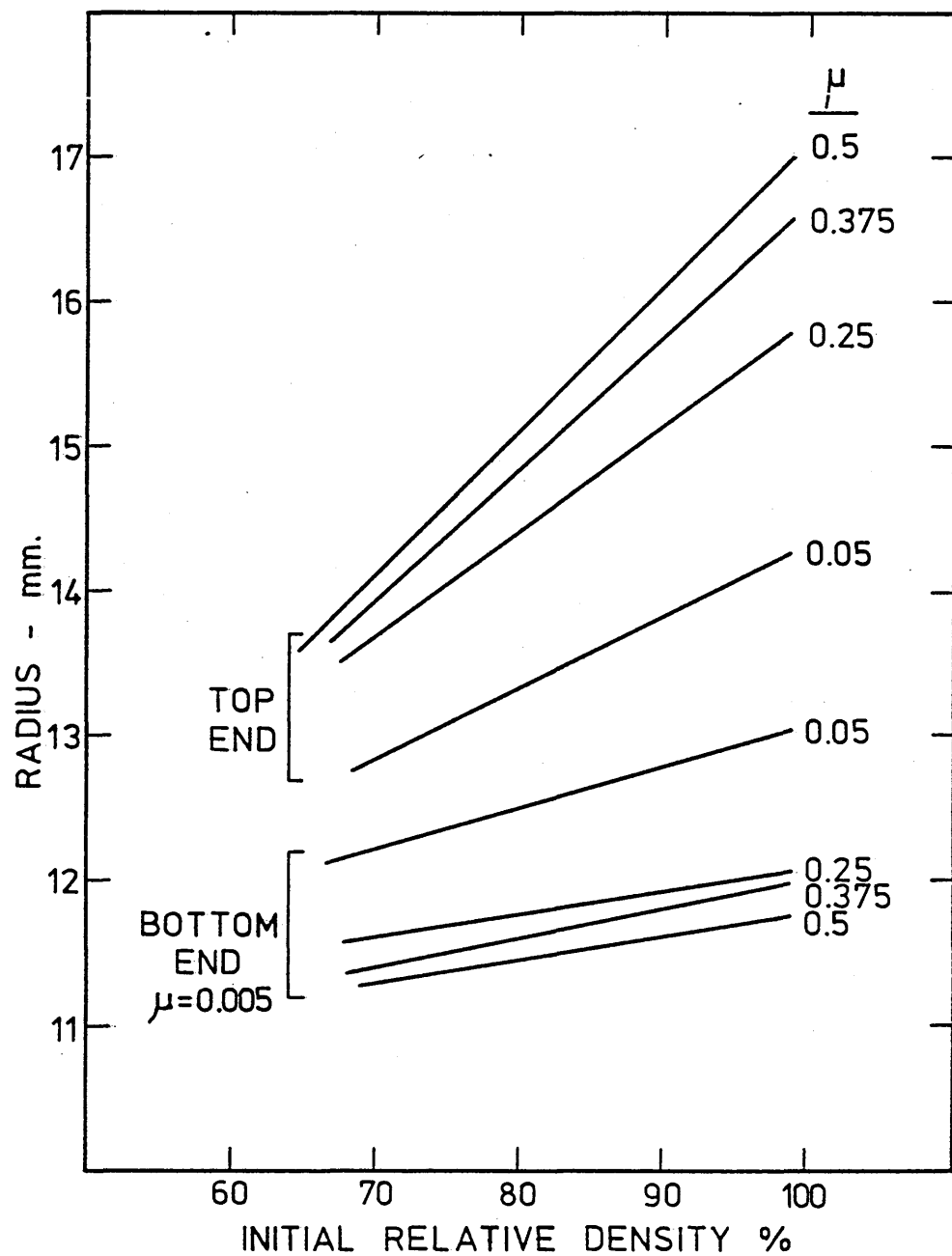


Fig (5.16) Comparison of radii at 50% reduction of height for various interface friction at top end with semi-frictionless at bottom end of specimens of various initial densities

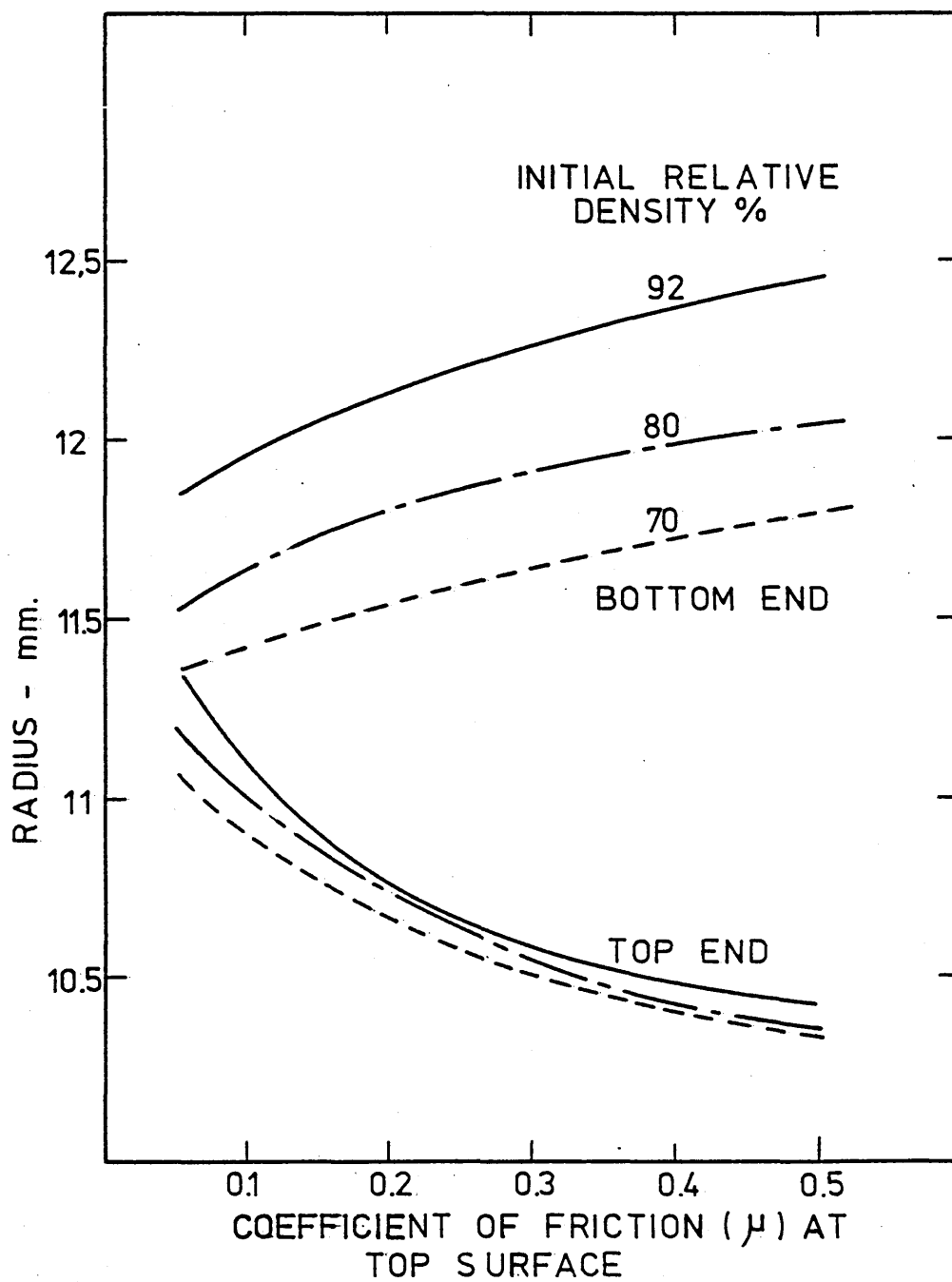


Fig (5.17) The variation in radius with interface friction for specimens of various initial densities upset with semi-frictionless condition at the bottom end interface

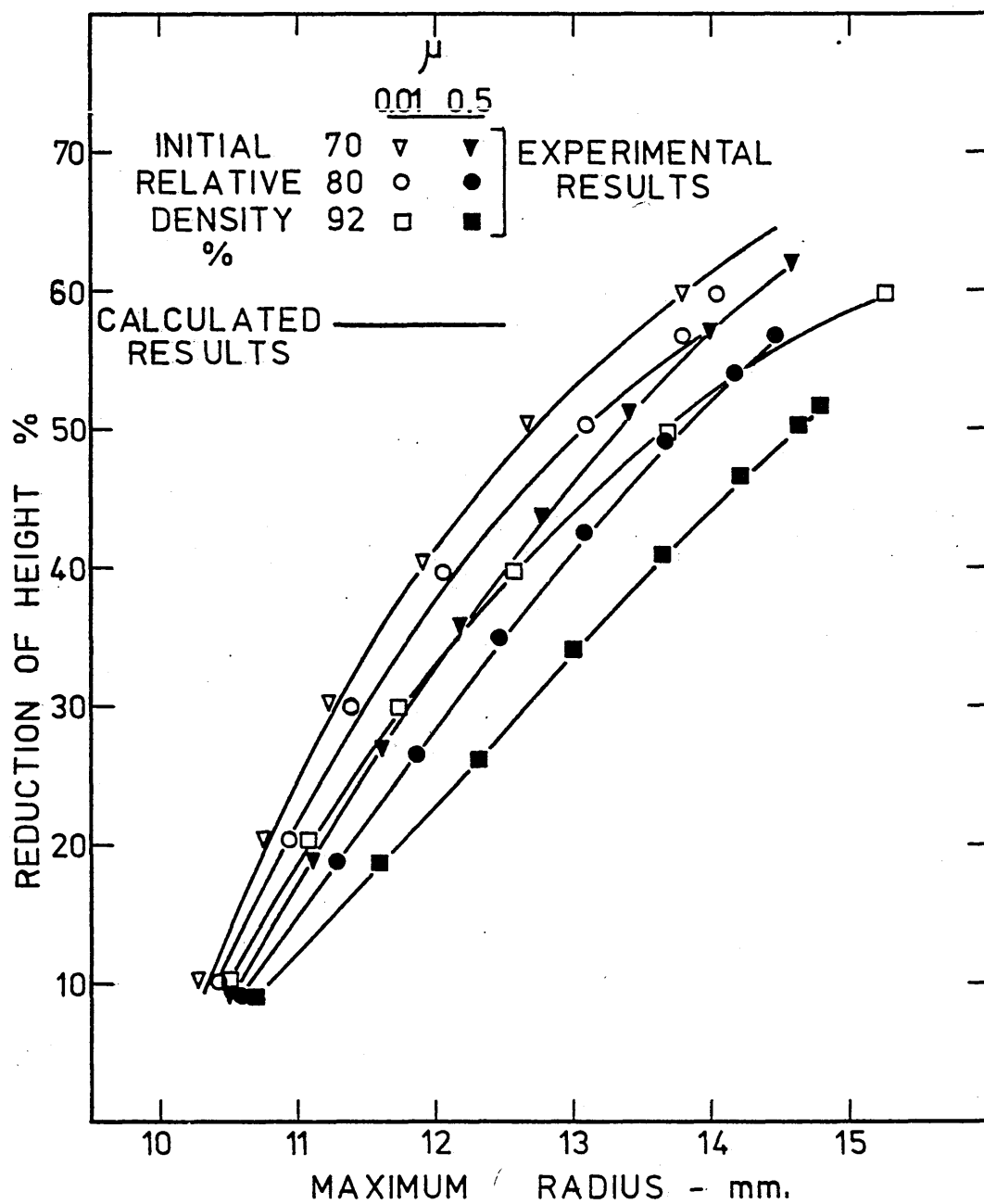


Fig (5.18) The effect of interface friction and initial density on the variation of maximum radius of cylindrical specimens with the reduction of height during upsetting

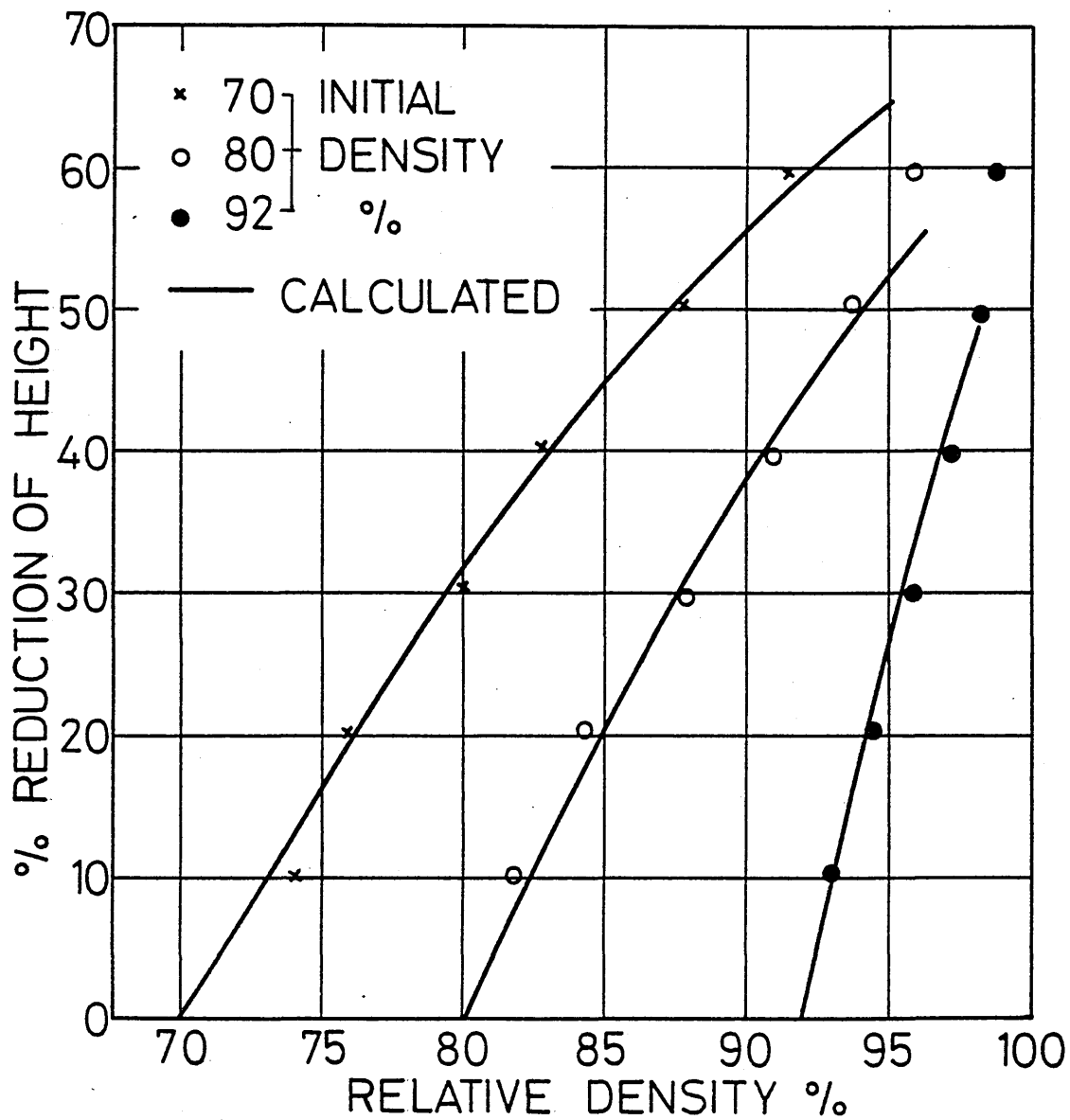


Fig (5.19) The variation of density with the reduction of height of specimens of various initial densities upset with PTFE as lubricant

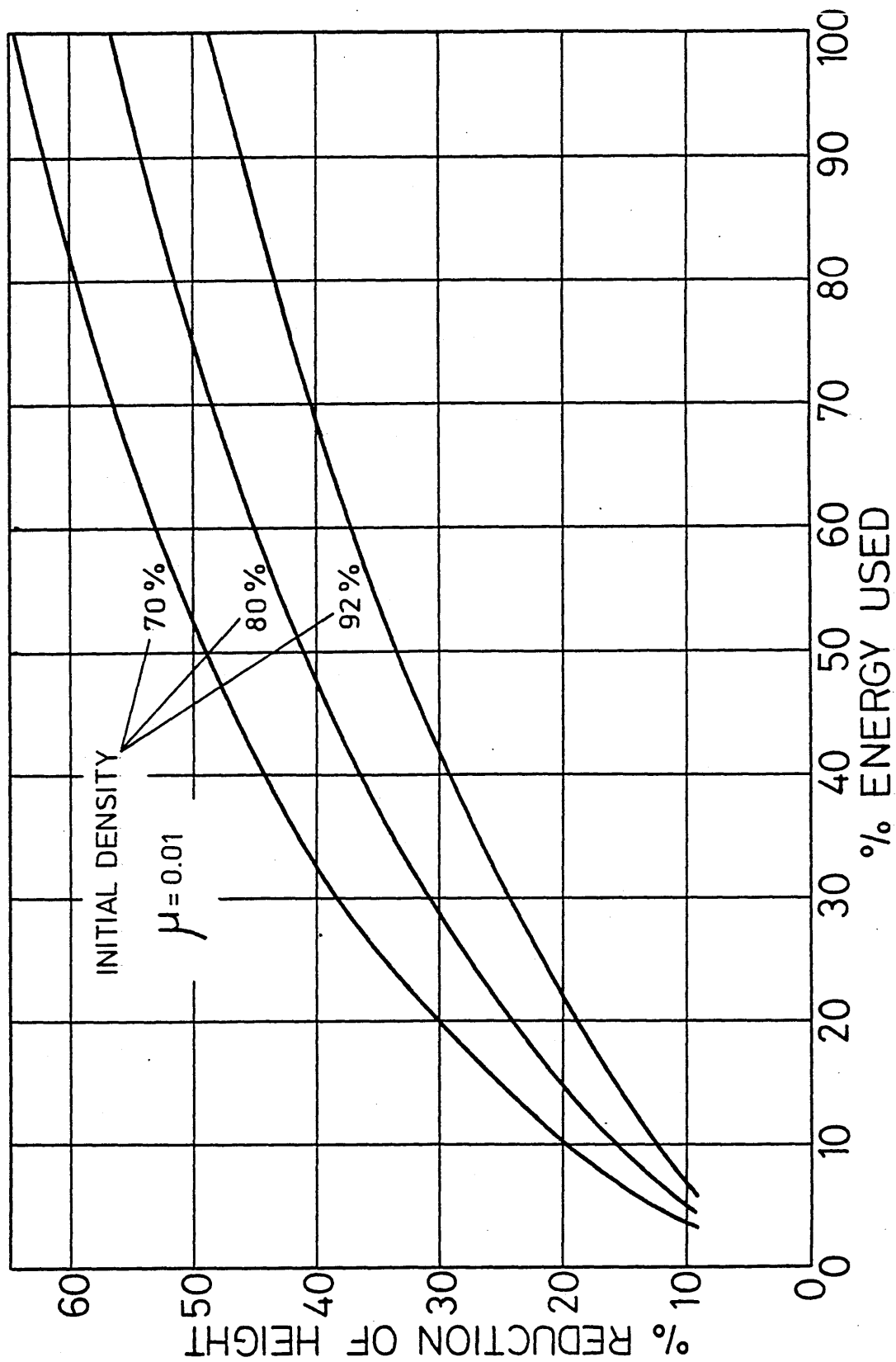
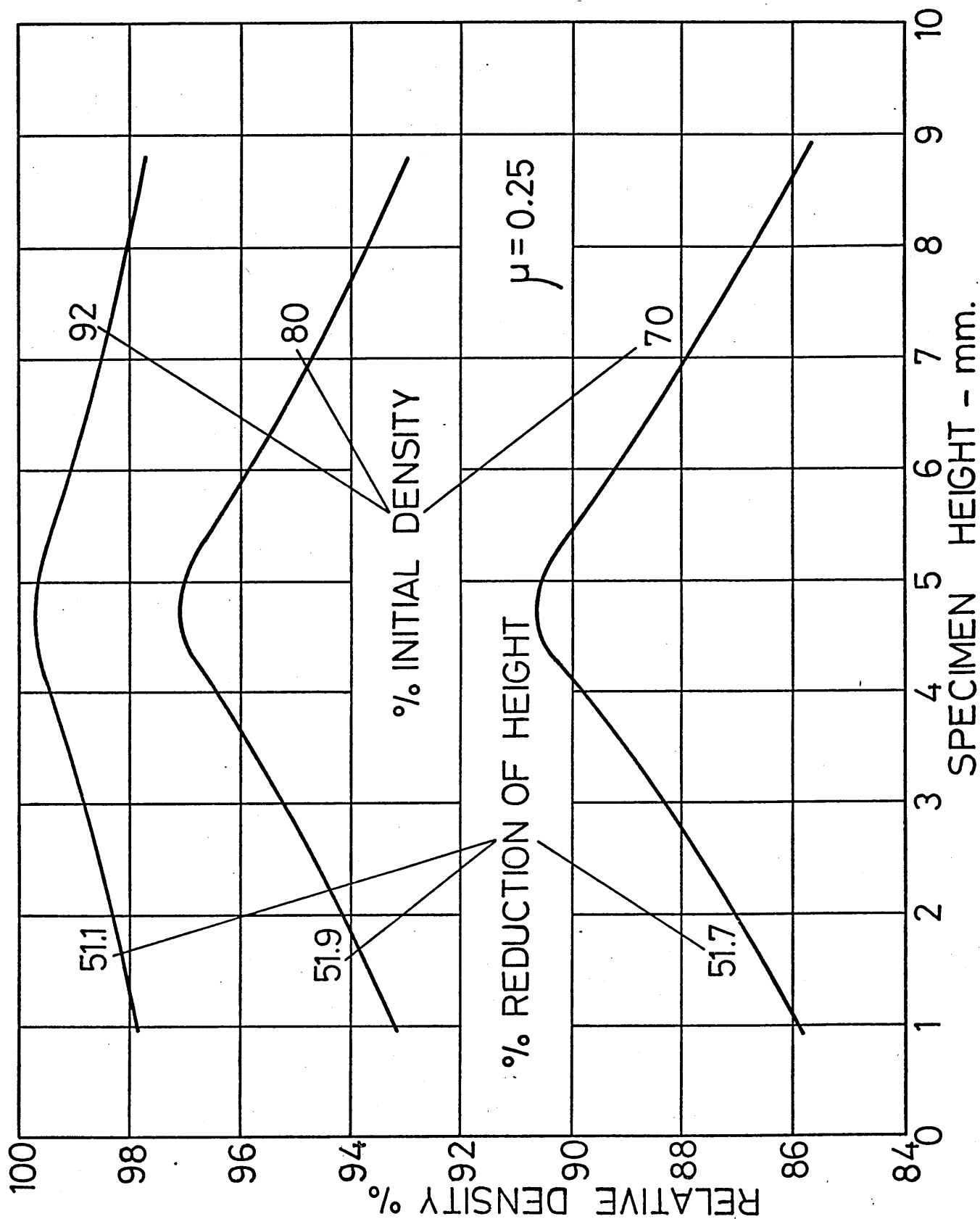


Fig (5.20) The variation of initial energy used with percentage reduction of height for specimens of various initial densities as predicted theoretically

Fig (5.21) The theoretically predicted distribution of density along the height of specimens of three initial densities, upset to identical reductions of height



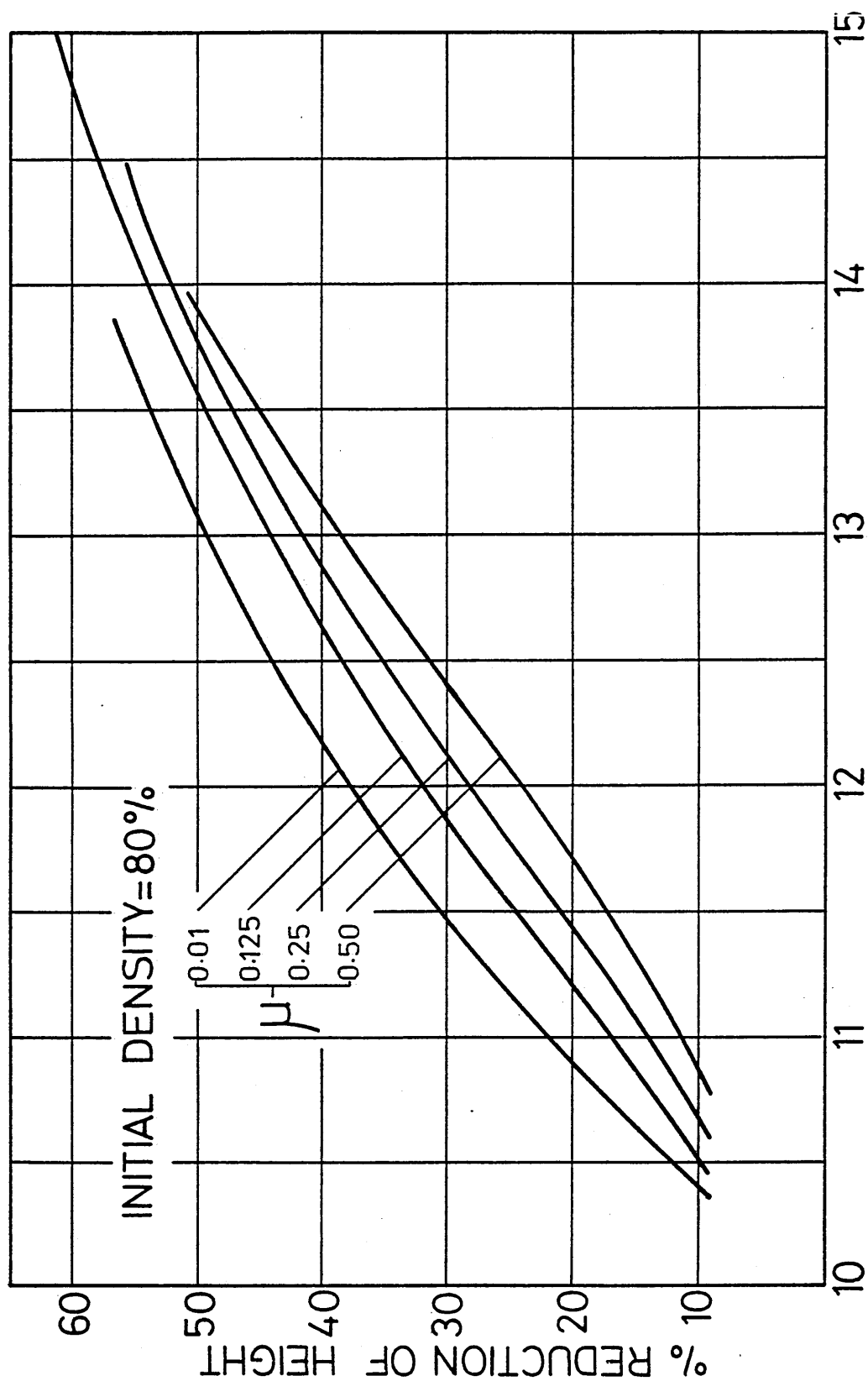


Fig (5.22) The effect of interface friction on the variation of the specimen mid-section radius (maximum) with reduction of height

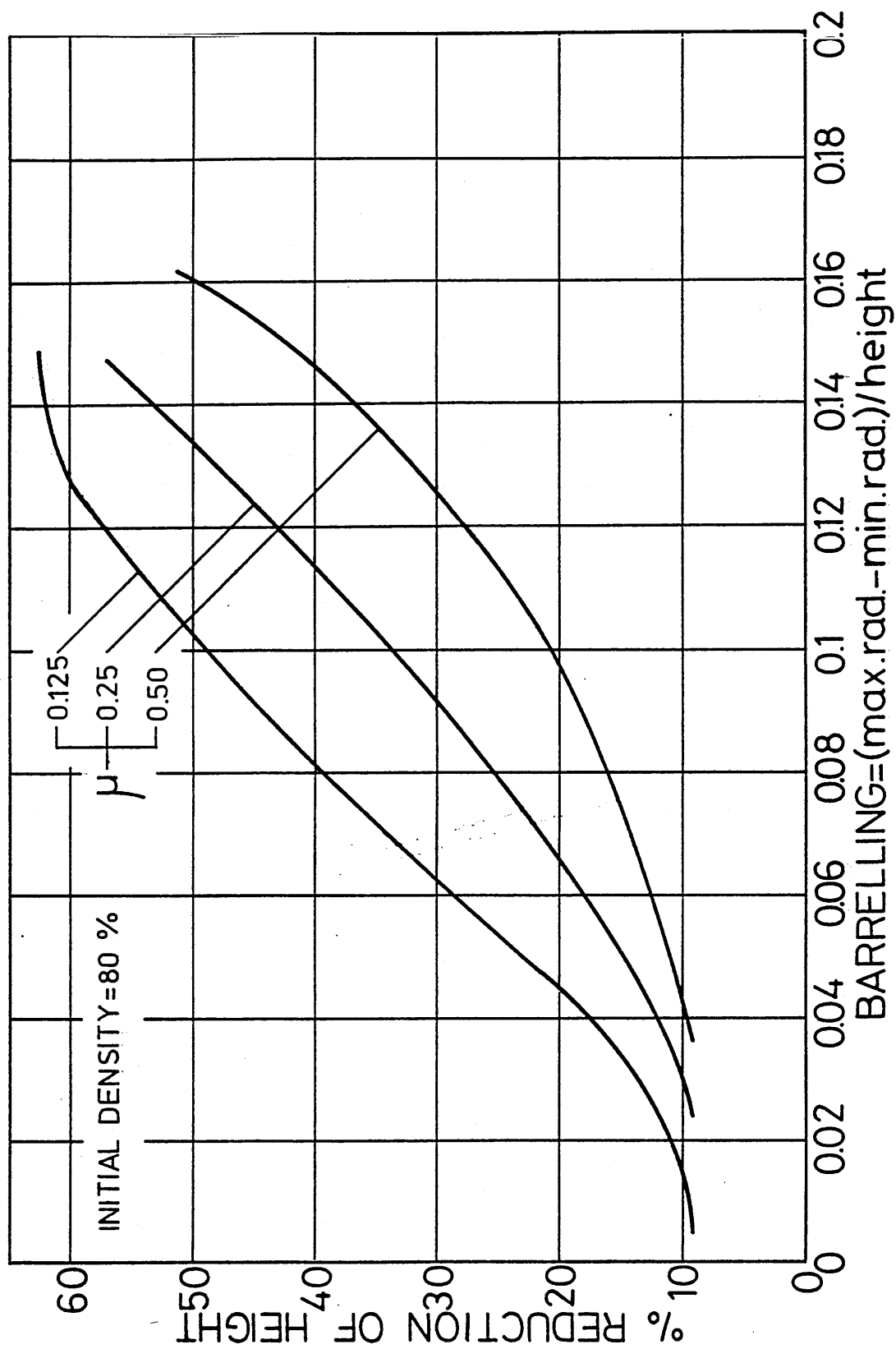


Fig (5.23) A theoretically predicted barrelling at various reductions of height of specimens upset with various interface frictions

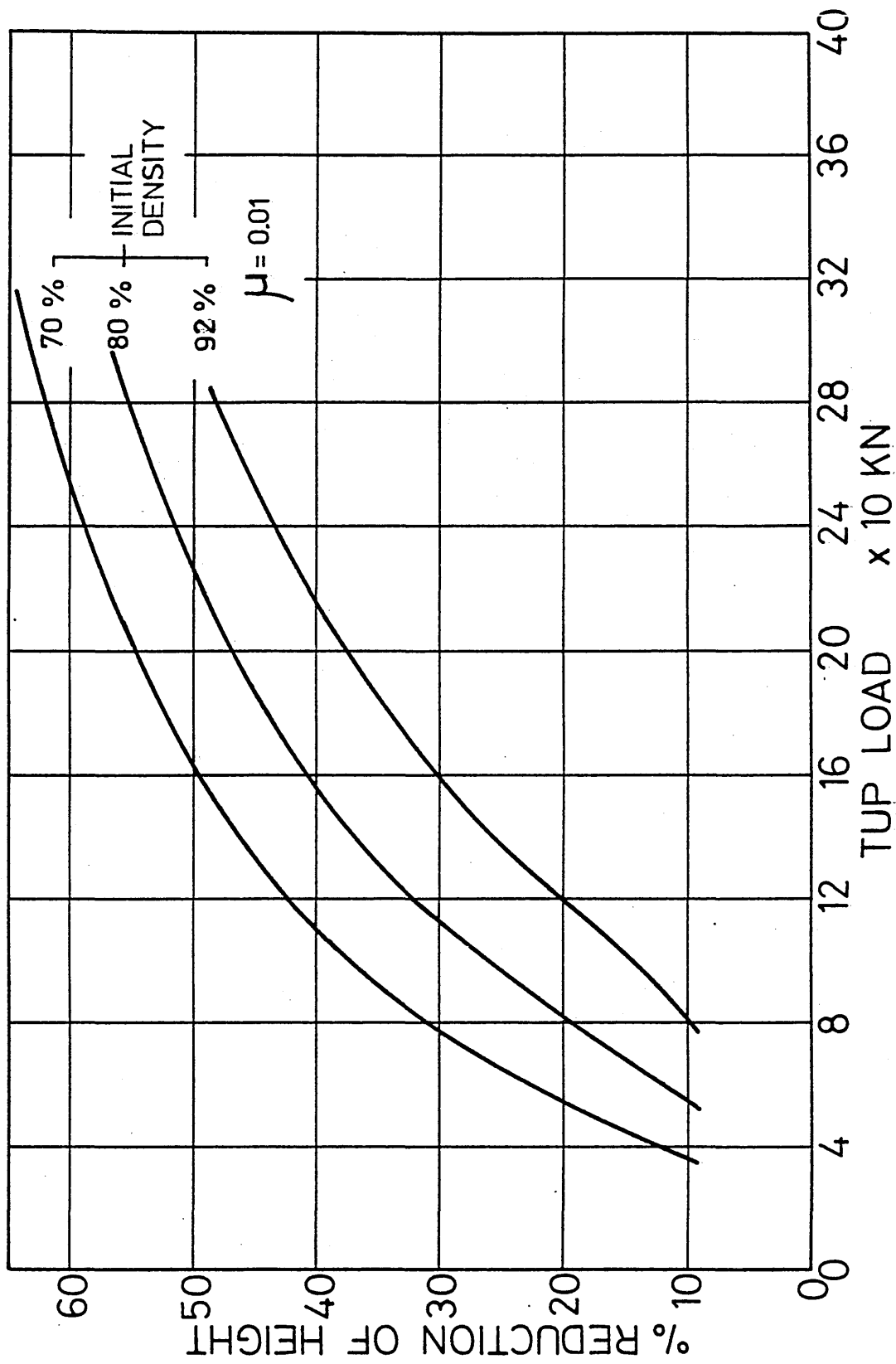


Fig (5.24) The variation of tup load with reduction of height for specimens of three initial densities, upset under lubrication condition

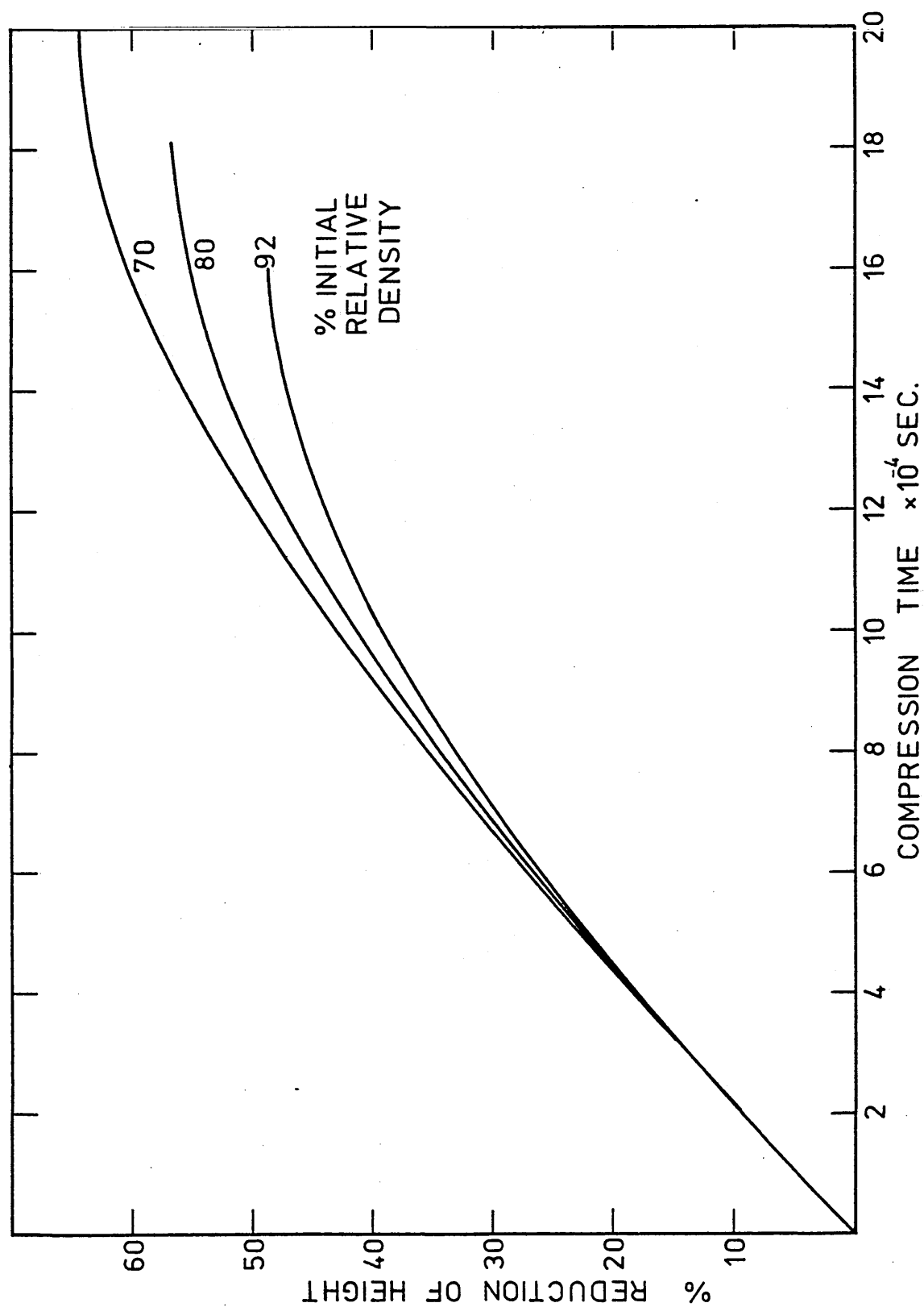


Fig (5.25) The variation of compression time with reduction of height for specimens of three initial densities upset under lubrication condition ($\mu = 0.01$)

CONCLUSIONS AND RECOMMENDATIONS

6.1 Conclusions

The following may be concluded from the present investigations:

1. This work has shown the importance of sintering time and temperature on the sintered and upset properties and on the deformation characteristics of the sintered material. In general the increase of sintering time and temperature improved the properties and promoted better deformation characteristics. However, the effect of sintering time was found to be comparatively small.

Upsetting stresses increased with sintering temperatures of up to 1100°C while the density and reduction of height at fracture were found to be maximum at 1200°C .

For the material investigated the temperature of 1100°C may be considered to give optimum properties for the range 900 to 1200°C

2. Aspect ratio has very significant effect on sintered materials and their deformation characteristics. Densification, lateral flow, and reduction of height at fracture were increased with the increase of aspect ratio, whilst the upsetting stresses to a fixed height were decreased.

Empirical equations describing the relationship between axial strain and aspect ratio, upsetting stress and

initial and final density, and initial aspect ratio and final aspect ratio were developed for upsetting cylindrical specimens without using a lubricant.

3. Deformation of porous prismatic blocks is generally identical to wrought materials. Sharp edges tend to cause buckling and the premature fracture of the specimen.

4. Porous materials cannot be extruded as easily as the formation of hubs unless a large draft angle is provided.

5. Restraining the two ends of the specimen during upsetting promotes deformation of highly porous preforms by reducing the extent of bulging and increases the densification rate.

6. A triangular-cavity die may be used as a measure of forgeability of sintered iron preforms of initial relative densities of up to 80%. An empirical equation fitting these results has been formulated.

7. Gear teeth can successfully be formed by forging sintered iron blanks. Decreasing the tooth width delays fracture and consequently promotes greater cavity filling. Furthermore, specimens of higher initial aspect ratio and density exhibits better cavity filling.

The extent of cavity filling at fracture can be calculated by applying an empirical equation obtained from the present work.

8. The role of initial density on plastic flow has been demonstrated and accordingly, any yield criterion for sintered iron which does not include initial density may not be sufficiently accurate. A space diagram for the stress-strain-density relationship of sintered iron during a semi-frictionless quasistatic compression test was constructed. This diagram shows the basic flow characteristics of sintered iron and compares them with those of mild steel. Hence it is very informative to the designer of sintered components providing a good illustration chart for the subject of porous materials.

Another diagram of similar importance showing the behaviour of sintered iron under various stress conditions was also constructed. Sintered iron yields under identical stress ratios at a high porosity level to those of solid metal, but these ratios deviate with the decrease in porosity although the resistance to yielding increases.

9. Simple upsetting of sintered iron compacts has been studied theoretically using a numerical technique which incorporates variable density dependent stress-strain properties of the compacts. Deformation characteristics were observed under a number of friction conditions. Theoretically predicted results when compared with those obtained by experiments showed a very good correlation.

6.2 Recommendations

Sintered material has a great potential for development because of the numerous production advantages they offer over their counterparts of wrought materials. Hence more thorough investigations are required in order to optimise their performance and to discover new areas of potential use.

Since the need for an accurate yield criterion is still outstanding, therefore, it is recommended that a research programme should be undertaken to examine the behaviour of sintered iron, copper and aluminium under uniaxial, plane and re-pressing stress conditions with and without using a lubricant at both room and at warm temperatures. Also measurements of the properties such as tensile, torsion, fatigue, hardness, impact and bending should be carried out at the sintered state and at the deformed states. It is hoped that with such kind of information, a yield criterion, empirically based could be developed.

Investigators exploring the mechanics of deformation of porous materials should look into the cause of fracture at the outside surface and inside the deformed specimen and relate this cause to the variation of porosity and various interface friction. The magnitude of the coefficient of interface friction needs to be determined for porous materials. The test-ring technique

may be recommended.

The variation of porosity within a single compact due to the compaction technique employed and subsequent deformation is worth looking into by other than hardness mapping technique.

When attempts are carried out to provide the designer of sintered components with useful data and practical charts and nomograms etc, these should be preceded by industrial visits and a survey of market needs. From time to time, a study of the economics of sintered components in comparison with other rival materials should be carried out.

It is recommended that any kind of machining in the preparation of any testpiece should have a ground finish. Also the scope for repeating the investigation carried in this work on different porous materials, such as mild steel, copper and aluminium is wide open.

REFERENCES

1. R B Bargainnier and J S Hirshhorn, "Forging Studies of a Ni-Mo P/M Steel". Fall PM Conf Proc Cleveland, Ohio, 1970.
2. W J Hyppmann, "The Effect of Powder Characteristics on the Sinter-Forging Process", Powder Metallurgy, Number 1, 1977.
3. H W Antes, "Cold Forging of Iron and Steel Powder Preforms", Modern Developments in Powder Metallurgy, Volume 4 (Processes), plenum press 1971.
4. H W Antes and P L Stock, "The Effect of Deformation on Tensile and Impact Properties of Hot PM-Formed Nickel-Molybdenum Steels". Powder and Metallurgy, Volume 17, Number 33, 1974.
5. G Zapf, "The Mechanical Properties of Hot Recompactd Iron-Nickel Sintered Alloys". Powder Metallurgy, Volume 13, Number 26, 1970.
6. R T Cundill, E Marsh and K A Ridal, "Mechanical Properties of Sintered/Forged Low-Alloy Steels". Powder Metallurgy, Volume 13, Number 26, 1970.

7. K Obara, Y Nishino and Y Saito, "The Cold Forging of Ferrous P/M Preforms", Modern Developments in Powder Metallurgy, Volume 7, 1973.
8. Y Araki, S Shima and M Oyane, "Friction at the Tool-Workpiece Interfaces in the Forming of Sintered Metals", Kyoto report on plasticity and metal forming, volume 2, 1977.
9. R A Huseby and M A Scheil, "Forging from P/M Preforms", American Society for Metals (ASM), Powder Metallurgy, Conf, Ohio 1970.
10. J B Marx, R Davies and T L Guest, "Some Considerations of the Hot Forging of Powder Preforms", 11th Int MTDR Conf, University of Manchester, 1970.
11. K Suzuki and K Shimamura, "Mechanical Properties of P/M Hot Forged Iron Preforms via HERF Process", Metals and Ceramics Materials Laboratory, Toshiba Electric Co Ltd, Japan, 1974.
12. S O Shalia and P Ramakrishnan, "Powder Preform Forging of a Low-Alloy Steel".

13. W J Hyppmann, "Forces During Forging of Iron Powder Preforms", The Int J Powder Metallurgy and Powder Technology, Vol 12, No 4, Oct 1976.
14. M S Maclean, W E Campbell and R J Dower, "An Insight into the Mechanical Properties of Powder Metal Forgings as a Function of Processing Route". Powder Metallurgy Int, Vol 7, No 3, 1975.
15. R J Dower, "Forging P/M Preforms at NEL", East Kilbride, Scotland.
16. G Bockstiegel and U Bjork, "The Influence of Preform Shape on Material Flow". Powder Metallurgy, Vol 17, No 33, 1974.
17. C L Downey and H A Kuhn, "Powder Preform Forging" (Technical Report). Drexel University, Department of Metallurgical Engineering, 1972.
18. B Aren, "Material Flow in the Powder Forging of a Gear-Profile as a Function of Preform Shape", Linkoping University, Department of Mech Eng, Sweden, 1975.
19. J C Billington, D E Fallas and A Torabi, "Deformation During Hot Rolling of Iron Powder Compacts". Powder Metallurgy, Vol 18, No 36, 1975.

20. I Amato, G Bollani and E Sgambetterra, "On the Tensile, Impact and Fatigue Properties of Sinter-forged Materials". Fiat, Central Laboratories, Orbassano, (Turin), Italy.
21. F Hanejko, "AISI 4000 Transverse and Longitudinal Impact Properties as a Function of Sintering Temperature and Deformation", Hoeganas Corporation, 1973.
22. P Ramakrishnan, "Mechanical Behaviour of Sinter-forged Materials, Proc 2nd Int Conf on Mechanical Behaviour of Materials, 1976, pp 1310-15.
23. K H Moyer, The Effect of Preform Density on the Impact Properties of Atomised Iron P/M Forgings. 1971 Fall Powder Metallurgy Conf Proc, 1972, pp 53-63.
24. K H Moyer, "The Effect of Flow on Impact Properties of Hot Formed Atomised Iron Preforms", Progress in Powder Metallurgy, vol 28, 1972, pp 303-312.
25. G Bockstiegel, "A Study of the Work Compaction in Powder Pressing", Powder Metallurgy, Int, Vol 3, 1971, p 17.

26. H W Ants, Processing and Properties of Powder Forgings,
Sagamore Army Materials Research Conf Proc, 18th, Raquette
Lake, NY, 1971, pp 171-210.
27. H F Fischmeister, Modern Techniques for Powder Metal
Fabrication of Low Alloy and Tool Steels, Ann Rev Mat
Sci, Vol 5, 1977
28. Eloff, PC and Guichelaar, PJ, Hot Formed Powder Preforms:
The relationship among deformation, Induction Sintering
and Mechanical Properties, Material Engineering Congress
Proc, October 1971, Cleveland, Ohio.
29. B Avitzur and P Blum, Forging and Extrusion of P/M
Preforms. Modern Developments in Powder Metallurgy,
vol 7, 1973, pp 73-90.
30. L F Hammond, E G Schwartz, Int J Powder Metallurgy, 1970,
6 (1), p 25.
31. M Koerner, Powder Metallurgy Int, 1971, 3, p 186.
32. G Bockstiegel and U B Jork, The Influence of Preform
Shape on Material Flow, Residual Porosity and Occurrence
of flows in Hot Forged Powder Compacts, Powder Metallurgy,
1974, 17 (33), p 126.

33. H Alkatib, Investigations into Mechanics of Deformation of Sintered Billets. MPhil Thesis, CNAA, 1975.
34. M M Hagerty, An Experimental and Theoretical Model of the deformation and densification of sintered powder metallurgy compacts. PhD Thesis, Drexel University, November 1972.
35. H A Kuhn, Flow and Fracture Criteria for Powder Forging. Fall Powder Metallurgy Conf Proc, October 1971, 0 299, Detroit, Mich.
36. H A Kuhn, Fundamental Principles of Powder Preform Forging. Sagamore Army Material Research Conf Proc, 18th, Raquette Lake, NY, 1971, pp 153-169.
37. M Storozhevskii, Some Problems of Modelling a Porous Body, Poroshkovaya Metallur, 1968, 5, 65, pp 409-413.
38. B Ya Pines and N I Sukhinin, Zh Tekh Fiz, 26, 2076 (1956).
39. W Kreher and H G Schopf, Effective Elastic-Plastic Compressibility of Porous Bodies, Int J Solids and Structures, 1973, Vol 9, pp 1331-1348.
40. T Y Chu and Z Hashin, Plastic behaviour of composites and porous media under isotropic stresses. Int J Eng, Sci 9 971 (1971).

41. Yu G Dorofeev, Theory and Technology of the Component Formation Process (Distribution of Density in Powder Blanks During Free Upsetting). Soviet Powder Metallurgy Mat, Seram, Vol 14, Part 5, pp 351-355, 1975.
42. V V Skorokhod and I F Martynova, Irreversible Deformation of a sintered porous body of work-hardening plastic metal. Sov Powder Metall Met Ceram, 1977, 16 (4), pp 295-8.
43. K Mori, S Shima and K Osakada, Analysis of Forming of Porous Materials Using the Rigid Plastic Finite Element Method. Kyoto Report on Plasticity and Metal Forming, Vol 2, 1977, pp 46-50.
44. R Haynes, A Theoretical Evaluation of the Strengths of Sintered Plain Carbon and Low-Alloy Steels. Powder Metallurgy, 1971, vol 14, No 27, pp 71-77.
45. R J Kahlow and B Avitzur, Void Behaviour as Influenced by Pressure and Plastic Deformation. Tran ASME J Eng Industry, August 1974, pp 901-911.
46. S Shima, T Tabata, M Oyane and T Kawakami, Upper Bound Theory for Deformation of Porous Materials, Memoirs, Faculty of Engineering, Kyoto University, 1976, vol 38, pp 117-137.

47. K A Kuhn and C L Downey, Deformation Characteristics and Plasticity Theory of Sintered Powder Materials, J Powder Metallurgy, vol 7, no 1, 1971.
48. R J Green, A Plasticity Theory for Porous Solids, Int J Mech Sci, Vol 14, 1972, pp 215-224.
49. M Oyane, S Shima and Y Kono, Theory of Plasticity for Porous Metals, Bulletin of JSME, 16, 1973, pp 1254-62.
50. S Shima and M Oyane, Plasticity Theory for Porous Metals, Int J Mech Sci, vol 18, 1976, pp 285-291.
51. T Tabata and S Masaki, A yield criterion for porous metals and analysis of axial compression of porous disks. Kyoto Report on Plasticity and Metal Forming, vol 2, 1977, pp 51-58.
52. Y Corapcioglu and T Uz, Constitutive Equations for Plastic Deformation of Porous Materials, Powder Technology, 21, 1978, pp 269-274.
53. F J Esper, H E Exner and H Metzler, The Correlation Between Raw Materials, Preparation Conditions and Properties of Sintered Iron, Powder Metallurgy, vol 18, No 35, 1975, pp 107-123.

54. M J Koczak and H Chung, The Effects of Elemental Alloying and Sintering Temperature on the Cold Forming of Powder Metallurgy Nickel Steels, ASM Conf on Powder Metallurgy, Int, Vol 7, No 2, 1975, pp 71-74.
55. Pease III and F Leander, The Effect of Processing on the Structure and Properties of Powder Metallurgy Materials, ASM Conf on Powder Metallurgy, 1970, 24 pages.
56. R Davies and M Negm, The Effects of Some Process Variables on the as-Forged Ni-Mo Alloy Steel. Powder Metallurgy, No 1, 1977, pp 39-47.
57. S J Hirschhorn, Introduction to Powder Metallurgy. APMI, NY, 1969.
58. H A Kuhn and C L Downey, Flow and Fracture Affect Design of Preforms for Powder Forging, Int J Powder Metallurgy and Powder Technology, vol 10, No 1, 1974, pp 59-66.
59. R Hill, The Mathematical Theory of Plasticity, Oxford University Press, London, 1967.

60. H Honess, Investigation of Plastic Deformation Characteristics of Sintered Iron at Room Temperature. Powder Metallurgy International, Vol 4, No 4, 1977, pp 170 - 173.
61. Y Corapcioglu and Z Angew, Math Mech to be published.
62. T Nakgawa, T Amaner, K Obara, Y Nishino and Y Maeda, On the Cold Forging of Sintered Iron Powder Preforms. Proc 13th Int MTDR Conf, Birmingham, September 1972, pp 455-461.
63. G Sjoberg, V Mironov and H Fischmeister, Die Filling and Densification in Hot Extrusion Forging of Porous Preforms. Powder Metallurgy Int, Vol 9, No 4, 1977, pp 160-163.
64. C L Downey and H A Kuhn, Designing P/M Preforms for Forging Axisymmetric Parts. The Int J Powder Metallurgy and Powder Technology, Vol 11, No 4, October 1975, pp 255-261.
65. H A Kuhn, P W Lee and T Erturk, A Fracture Criterion for Cold Forming. TRANS ASME J Eng Materials and Tech, Vol 95H, 1973, pp 213-218.

66. C L Downey and K A Kuhn, Application of a Forming Limit Concept to the Design of Powder Preforms for Forging. TRANS ASME, J Eng Materials and Tech, Vol 97H, 1974, pp 121-125.
67. S Y A Aku, R A C Slater and W Johnson, The Use of Placticine to Simulate the Dynamic Compression of Prismatic Blocks of Hot Metal, Int J Mech Sci, Vol 9, 1967, pp 495-525.
68. H Riedel, Doctoral Dissertation, Aachen 1913.
69. M Kurrein, Plasticity of Metals, Chapt 3, Griffin, London 1964.
70. W Johnson, R A C Slater and A S Yu, Int J Mech Sci, 6, 409, 1964.
71. H A Kuhn, Designing Powder Preforms. Technical Paper, Society of Manufacturing Engineers, MF76-395, Michigan, 1976.
72. H A Kuhn, S K Suh and M L Robinson, Metal Flow Studies for Powder Preform Forging.
73. M S J Hashmi and F B Klemz, The Effect of Friction in Simple Upsetting of Cylindrical Billets of Elastic-Plastic and Elastic-Strain Hardening Material: A Numerical Technique. Proc 17th Int MTDR Conf 1976, p 597.

74. M S J Hashmi, A Numerical Technique for Analysing Simple Upsetting of Cylindrical Billets of Strain Rate Sensitive Material, Proc 18th Int MTDR Conf 1977, p 27.